Statistics of non-affine displacements: Defect precursors and stability of lattices

Thesis

by Pankaj Popli

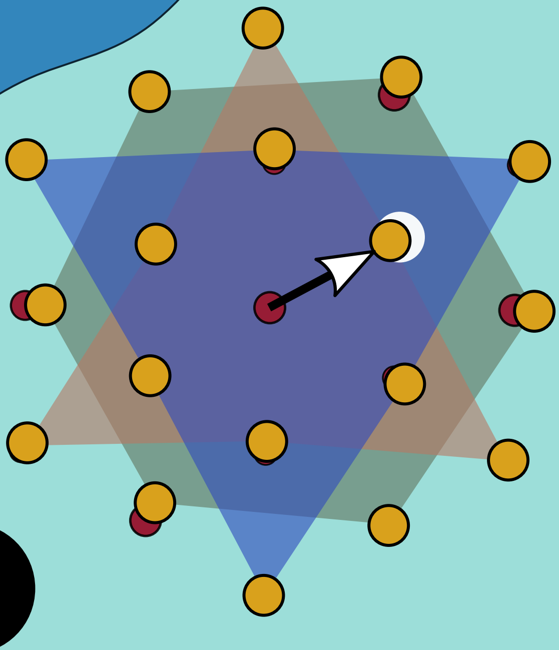

A route to robotic swarms...

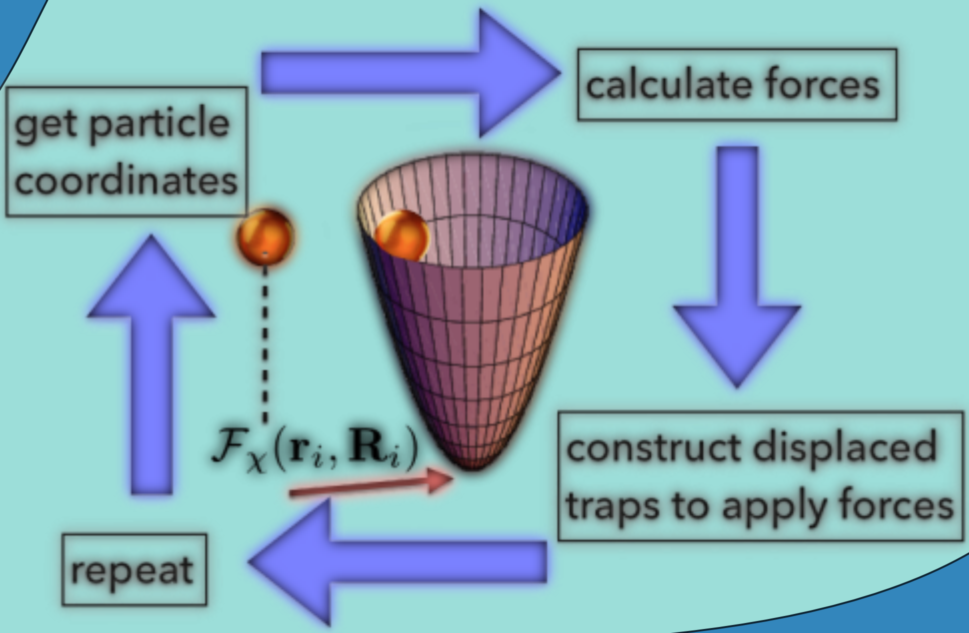
calculate forces
get particle coordinates
$\mathcal{F}_\chi(\mathbf{r}_i, \mathbf{R}_i)$
construct displaced traps to apply forces
repeat

Statistics of non-affine displacements : Defect precursors and stability of lattices

A Thesis

Submitted to the
Tata Institute of Fundamental Research, Mumbai
for the degree of Doctor of Philosophy
in Physics

by

Pankaj Popli

TATA INSTITUTE OF FUNDAMENTAL RESEARCH
TIFR CENTER FOR INTERDISCIPLINARY SCIENCES
Hyderabad, India

December, 2020

Dedicated to Mom & Dad

Abstract

Fluctuations in atomic positions are classified as being either (i) “smooth”, consisting of long wavelength phonons, or (ii) “singular”, arising from topological defects [1]. This classification has led to a deeper understanding of many properties of crystalline solids such as melting [1, 2], and mechanical failure of solids under external loads [3, 4]. However, it is not optimal to obtain a linear combination of phonons equivalent to the prevailing local lattice defects (describing local lattice defects in terms of phonons is clearly not optimal). Further, in amorphous solids, the lack of long-range structural order makes it hard to distinguish between smooth and singular displacements. In a recently introduced, alternative, way of classifying fluctuations [5], any set of displacement of particles away from some specified reference configuration is projected onto two mutually orthogonal spaces viz. *affine* and *non-affine*. The affine modes involves *continuously* varying, elastic displacements, and can be written as a linear transformation of this reference configuration. Whereas the non-affine modes, consists of displacements which are not linear transformations and are related to defects in certain two dimensional crystalline (mono-atomic) lattices [6]. In addition, the likelihood of a particular defect can also be estimated from the excitation spectra of non-affine modes [6, 7]. Earlier work in this direction was restricted to two dimensions and simple monatomic lattices. Physical systems in nature, however, is three-dimensional and has multi-atom basis. Therefore, non-affine modes for these systems need to be determined and studied.

In this thesis, we generalise this projection formalism to the lattices with multi-atom basis in d-dimension. The statistics of non-affine displacements due to thermal fluctuation is then analyzed in a variety of two-dimensional lattices such as square, honeycomb, and kagome. Where in three-dimensions, we limit our analysis to the crystals from cubic family. In each case, we demonstrate that the non-affine modes are indeed the precursors to the commonly observed lattice defects. Additionally, deformations such as slips or stacking faults can also be understood using these modes. We further test the robustness of our results to the extent of different parameters and inter-particle interactions. Our study reveals that the prevalent non-affine modes lead to particle rearrangement and may not maintain the topology of the local neighbourhood of a particle; a finding that has significant implications for the stability of lattices.

Equipped with this knowledge, we devise an experimental protocol to stabilise (i) lattice of colloidal particles, and (ii) patterns of active robotic swarm. This is accomplished in an energy efficient way by imposing feedback controlled “non-affine forces”. These restoring forces alter the particle’s arrangement in order to minimise non-affine fluctuations while allowing only affine transformations. Moreover, our stabilisation procedure/algorithm needs no awareness of inter-particle interactions or the particulars of underlying noise but the details of instantaneous and reference configuration. *In colloids*, the resulting colloidal lattice is translationally invariant and retains all the low-energy phonon modes. We further note that the non-affine forces depends upon the reference structure, therefore, the symmetry of the lattice can be changed at will. *In robotic swarms*, the pattern obtained is stable and as a whole can be translated without interfering with the stabilisation algorithm. The agents are not forced to sense, difficult to measure, environmental parameters such as local velocity of air or water in order to stabilise the swarm. A novel outcome of this study is that by maintaining the structure of robotic swarm, the statistics of underlying flow field can be determined solely from non-affine forces. As non-affine forces are a-priori known, no extra measurement on the turbulent field is required to obtain the statistics. Therefore, such techniques will be useful in studying the turbulent flow where the direct measurement of flow velocities is difficult.

We conclude the thesis with a list of possible future applications of the principles presented in this thesis.

Contents

1 Introduction **1**
- 1.1 Order and fluctuations in systems of particles 1
- 1.2 A crystal in a box: statistics of atomic fluctuations 3
  - 1.2.1 Computer simulations 3
  - 1.2.2 Experiments with colloidal solids 4
- 1.3 Elastic constants from atomic fluctuations 5
  - 1.3.1 The defect free case 5
  - 1.3.2 The crystal with defects 6
- 1.4 Non-affine displacements: a summary of the thesis 7

2 The projection formalism for non-affine displacements **9**
- 2.1 The Falk-Langer least square fit formalism 9
- 2.2 The projection method for lattices with mono-atomic basis 11
  - 2.2.1 Spatial direct- and cross- correlations 17
- 2.3 Generalisation to lattices with multi-atom basis 18
  - 2.3.1 Spatial direct- and cross- correlations 23
- 2.4 Summary and conclusion 26

3 Non-affine displacements in $2d$ and $3d$ crystals **27**
- 3.1 Model Hamiltonian 27
  - 3.1.1 The triangular lattice in $2d$ 30
  - 3.1.2 The square lattice in $2d$ 32
  - 3.1.3 The planar honeycomb lattice in $2d$ 33
  - 3.1.4 The Kagome lattice in $2d$ 35
  - 3.1.5 The simple cubic lattice in $3d$ 36
  - 3.1.6 The body-centered cubic lattice in $3d$ 38
  - 3.1.7 The face centered cubic lattice in $3d$ 39
- 3.2 Coupling between affine and non-affine displacements 40
- 3.3 Spatial correlations for $2d$, $3d$ mono-atomic lattices 41
- 3.4 Summary and conclusion 44

4 Non-affine displacements and deformation modes **45**

4.1 Deformation of solids: a brief background 45
4.2 Deformation of the triangular solid 45
4.3 Deformation of the square solid 47
4.4 Deformation of the FCC solid 48
4.5 Summary and conclusion 49

5 Stabilising colloidal crystals **51**
5.1 The feedback loop 52
5.2 Application to colloidal crystals 54
    5.2.1 Simple square lattice with harmonic interactions 54
    5.2.2 Simple square lattice with Gaussian interactions 55
    5.2.3 Complex open lattices 58
    5.2.4 Stabilisation mechanism 59
    5.2.5 Experimental realisation of the stabilisation procedure 62
5.3 Summary and conclusion 63

6 Stabilizing order in robotic swarms **65**
6.1 Introduction 65
6.2 A robotic swarm in a turbulent flow 67
    6.2.1 Modelling the flow field 68
    6.2.2 Modelling active forces 70
6.3 Results 74
    6.3.1 Model A: Floppy swarm 75
    6.3.2 Model B: Rigid swarm 76
6.4 Summary and conclusion 78

7 Thesis conclusion and future direction **87**

A Appendix A **91**
A.1 Dynamical matrix for harmonic interactions 91
    A.1.1 Square 91
    A.1.2 Triangular 91
    A.1.3 Triangular with bond bending: 92
    A.1.4 Planar honeycomb 92
    A.1.5 Honeycomb with bond bending 93
    A.1.6 Kagome 94
    A.1.7 SC 96
    A.1.8 BCC 97
    A.1.9 FCC 97
A.2 Strain correlation iso-surfaces for 3d lattices 98

A.2.1 SC 98
A.2.2 BCC 99
A.2.3 FCC 100

B Appendix B **103**

Bibliography **111**

List of Figures

2.1 Schematic showing coarse-graining volume Ω around set of particles arranged in triangular lattice. Dotted circle represents zero temperature reference position and colored circles are the instantaneous positions. 11

2.2 From [5]. **(a)** to **(h)**, eigenvectors correspond to non zero eigenvalues of PCP for the case of triangular lattice. The $N_\Omega = 6$ resulting 12 eigenvalues in two dimensions. Four eigenvalues out of twelve are zero and correspond to affine modes and are shown in Fig 2.3. 15

2.3 From [5]. **(a)** to **(d)**, eigenvectors correspond to non zero eigenvalues of $(\mathsf{I}-\mathsf{P})\mathsf{C}(\mathsf{I}-\mathsf{P})$. The eigenvectors correspond to four non zero eigenvalues represents the affine transformation of the reference lattice, volume change, uni-axial strain, shear, and rotation. 15

2.4 Schematic showing the two coarse-graining volume for cross correlations. 17

2.5 Schematic showing coarse-graining volume Ω for lattice with basis. Different color represents two different basis atoms and dotted circles are zero temperature position of the particles. Each cell (dotted ellipse) denotes the lattice sites, here arranged in a triangular lattice. The particular schematic here has two basis atom, however, more basis atoms can be added. 18

2.6 Schematic showing two coarse-graining volume for cross correlations. Two distant neighborhoods Ω and $\bar{\Omega}$ are situated around lattice sites i and k respectively. 24

3.1 Schematic diagram showing the triangular **a.**, square **b.**, planar honeycomb **c.**, kagome **d.**, simple cubic **e.**, body centered cubic **f.** and face centered cubic **g.** lattices. The nearest neighbor bonds are shown in bold while the next nearest neighbor bonds, whenever present, are drawn using dashed lines. The parameter a is the lattice constant, chosen to be unity. The equilibrium bond angle θ_0 has also been marked for the triangular and honeycomb lattices. In the 3d cases shaded color regions have been added to make the cubic geometry clearer. 28

3.2 Scaled distribution $P(\chi^{\star})$ for all 2d lattices where $\chi^{\star} = \chi/\langle\chi\rangle$. The solid colored lines are from our analytic calculations and the points are simulation results (using $N = 1024$ except for Honeycomb, where $N = 512$ and Kagome, where $N = 300$). Triangular: light pink with $k_b = 0$; Square: sky blue, $k_2 = 0.5$; Honeycomb: brown, $k_2 = 0.5$ and Kagome: purple, $k_2 = 0.5$. The distribution for square and triangle plotted here is for the smallest coarse-graining volume used in Sections 3.1.1 and 3.1.2. Whereas, for other lattices coarse-graining volume is same as shown in Fig 3.6 and 3.8. 29

3.3 Scaled distribution $P(\chi^{\star})$ for all 3d lattices, where $\chi^{\star} = \chi/\langle\chi\rangle$. The meaning of the symbols is the same as in Fig. 3.2. The distribution is plotted for SC: sky blue, $k_2 = 0.5$, $N = 1000$. BCC : brown, $k_2 = 0.5$, $N = 2000$. FCC: purple, $k_2 = 0.75$, $N = 4000$. The coarse-graining volume is described in the text. 30

3.4 Non-affine modes for triangular lattice with different sizes of the coarse graining volume Ω at inverse temperature $\beta = 1000$ with no next nearest neighbor bonds. **a.** The spectrum of the eigenvalues of PCP is shown for three different choices of Ω (inset), which consists of all particles within the first (Ω_1 - light blue), second (Ω_2 - magenta) and third (Ω_3 - dark green) nearest neighbor shells. The reference positions of particles are shown by small yellow circles. The horizontal lines show the eigenvalues. Note the large gap between the largest eigenvalue and the rest of the spectrum. **b.** The two degenerate eigenvectors corresponding to the largest eigenvalue of PCP. Note that a nearest neighbor bond is being stretched and a next near neighbor bond nearly perpendicular to it has been shortened. This mode is same as the one discussed in Ref. [6]. This displacement tends to replace the six-fold neighborhoods by two five- and two seven-fold neighbors producing a tightly bound dislocation–antidislocation pair. **c.** and **d.** show that increasing Ω does not affect the nature of this mode. 31

3.5 Non-affine modes for square lattice with different sizes of the coarse graining volume Ω. The parameters are $k_2 = 0.5$, $\beta = 1000$. **a.** The spectrum of the eigenvalues of PCP is shown for three different choices of Ω (inset). The color code is the same as in Fig. 3.4**b** The two degenerate eigenvectors corresponding to the largest eigenvalue of PCP. These modes tend to shift a row of atoms relative to adjacent rows **c.** and **d.** show that, as in the triangular case, increasing Ω does not affect the nature of these modes. . 32

3.6 Non-affine modes and spectra for the planar honeycomb, with $k_2 = 0.5$ and $\beta = 500$. **a.** Schematic of the lattice and the coarse graining volume (pink shaded region) used, with ellipses drawn around each pair of atoms that is in the same basis. **b.** The eigenvalue spectrum. Note that there is no single prominent eigenmode with a large gap as in the triangular and square structures. **c.** Plots of the first three non-degenerate non-affine eigenmodes in the order of prominence (magnitude of eigenvalue). Eigenmode 2 represents an incipient Stone-Wales defect. 33

3.7 Plot of the eigenvalues σ_i of PCP (colored lines, top panel) as a function of the bond angle rigidity parameter k_b, showing the effect of including bending rigidity of bonds in the triangular **a.** and planar honeycomb **b.** structures. While the relative prominence of the modes is unaffected in the triangular lattice except for the breaking of degeneracy of some low probability modes, in the honeycomb lattice the mode corresponding to the SW defect precursor (yellow) is strongly suppressed with increasing k_b (see text). 35

3.8 **a.** Schematic of the Kagome lattice and coarse-graining volume Ω (pink shaded region), **b.** the spectrum of non-affine modes and **c.** 1-3, the three most prominent non-affine modes. Parameters used: $k_2 = 0.5$, $\beta = 100$. . . 36

3.9 **a.** Plot of the eigenvalues of the SC lattice for three different values of k_2: 0.25, 0.5 and 1.0. **b.** The non-affine mode corresponding to the largest eigenvalue for $k_2 = 0.5$ and $\beta = 1000$. Note that this is similar to what is obtained for the square lattice. 37

3.10 **a.** Plot of the non-affine eigenvalues of the BCC lattice for three different values of k_2: 0.5, 0.75 and 1.0 at $\beta = 1000$. **b.** One of the non-affine modes with the largest eigenvalue for $k_2 = 0.75$. 38

3.11 **a.** Plot of eigenvalue spectra of FCC for different choice of $k_2 : 0.25, 0.5$ and 1.0 at $\beta = 1000$. **b.** The eigenmode corresponding to the largest eigenvalue for $k_2 = 0.5$. **c.** Same as **b.** but viewed from the $[111]$ direction. Notice that the central particle has displaced out of plane and sits below a particle from a different stacking layer, resulting in a stacking fault in the FCC system. 39

3.12 Normalized χ correlations, $C_{\chi\chi}(\rho) = (\langle\chi(0)\chi(\rho)\rangle - \langle\chi(0)\rangle^2) / \left(\langle\chi(0)^2\rangle - \langle\chi(0)\rangle^2\right)$, for several different lattices as a function of distance $\rho = \mathbf{R}\cdot\hat{\mathbf{x}}/d_{nn}$ measured in units of the *nearest neighbor distance*, d_{nn} in the reference lattice along one coordinate axis. Brown and blue are for square and triangle lattices ($d_{nn} = a$); orange and red are for FCC ($d_{nn} = a/\sqrt{2}$) and BCC ($d_{nn} = a\sqrt{3}/2$) respectively. 41

3.13 Iso-strain surfaces for the strain-strain correlation functions in Fourier space and in the $\mathbf{q} \to 0$ limit for SC, BCC, FCC lattices. Figures shown for **a.** deviatoric ($e_{xx} - e_{yy} - e_{zz}$), **b.** shear ($e_{xy} + e_{yx}$) and **c.** volume ($e_{xx} + e_{yy} + e_{zz}$) strains. The values of the correlations at the iso-surfaces are different in each case and have been chosen for ease of presentation. They are listed in the Appendix A.2 along with the full algebraic expressions used to plot the iso-surfaces. The other parameters used are $k_2 = 1/6$ and $\beta = 1$ throughout. 42

4.1 **a.** Relative contribution from non-affine modes when a slip is introduced by translating the bottom half of a triangular lattice along a close-packed direction by a lattice spacing. **b.** The corresponding contribution of the four affine modes. Note that the largest contributions come from shear and rotation. The insets show the configuration of atoms in Ω after the slip (**a**-i) and the separate non-affine (**a**-ii) and affine (**b**) contributions. See text for details. 46

4.2 Non-affine contribution in the square lattice when the middle row is displaced by half a lattice spacing. Note that this transformation tends to produce a triangular lattice symmetry starting from the original square lattice. 47

4.3 Contribution from different **a.** non-affine and **b.** affine modes when one introduces a slip in the FCC lattice. The inset shows a schematic diagram of the lattice as seen from the $[111]$ direction. The original position of the close packed lattice plane is shown as a triangle with a blue dotted boundary and the final position as a blue shaded triangle. Contribution from a stacking fault from **c.** non-affine and **d.** affine modes. The inset shows, as before, the original and final positions of a close packed plane of atoms. 48

5.1 Schematic diagram showing the steps involved in generating feed-back controlled optical traps. The particle coordinates are obtained from video microscopy. The neighbourhood of each particle is recorded and the force $\mathcal{F}_\chi(\mathbf{r}_i, \mathbf{R}_i)$ (see text) calculated from the Hamiltonian 5.1. Next, the positions of optical traps needed for applying these forces are calculated and the traps deployed. If this procedure is continuously repeated for all particles at a rate comparable to typical vibrational frequencies of the colloidal particles, a uniform stabilising field is obtained. 53

5.2 **a.** Phonon dispersion curve $\omega(q)$ plotted along high symmetry directions for a square lattice network of vertices connected by springs. Both nearest neighbour and next nearest neighbour springs with spring constants $k_1, k_2 > 0$ are needed for stability. The longitudinal (transverse) modes are shown with solid (dashed) lines. The colours denote $k_2 = 0$ (black), 0.1 (red) and 0.5 (blue). **b.** Phonon dispersion for $k_2 = 0$ but now for various values of $h_X = 0$ (black), 0.003 (red), 0.03 (blue). Insets show the interaction volume Ω in the square lattice with bonds (left) and the high symmetry points of the corresponding Brillouin zone (right) 54

5.3 **a.** Phonon dispersion curve $\omega^2(q)$ plotted along high symmetry directions for a square lattice of particles interacting with the GCM potential at $\rho = 0.5$ and $T = 1 \times 10^{-3}$. The small q region where $\omega^2 < 0$ is shown in the inset. We follow the same convention as in Fig. 5.2. There are two sets of curves for $h_X = 0$ (red curves) and $h_X = -0.5$ (blue curves). **b.** A stability diagram for finite size square lattices constructed from the dispersion curve in **a.** The green shaded region represents $-h_X$ values below which the square lattice becomes unstable ($\omega^2(q) < 0$). We have also marked six points on the graph such that black (white) circles denote stable (unstable) square lattices. 56

5.4 **a.** Configurations obtained from Monte Carlo simulations after 6×10^6 MCS arranged according to the corresponding points marked off in Fig 5.3**b** verifying the stability condition. Colours correspond to the local value of χ. **b.** $P(\chi)$ obtained from the equilibrated configurations where the square lattice is stable (top) and unstable (bottom). The data points are computed from the results of our simulations and the lines are predictions of the harmonic theory [7]. The configurations and the curves are labelled by the corresponding h_X and N values. 56

5.5 Typical particle configuration from the simulation performed to stabilise complex and simple lattices. Particles in the simulation has Gaussian interaction with the parameters defined in the text and $h_X = -2$. In the beginning, non-affine forces are determined from the projection matrix P defined for kagome lattice. At latter time t, the projection matrix was switched from one lattice symmetry to the other. **a.** Typical configurations of stable lattices at different times. **b.** Plot of global non-affinty parameter X as a function of time. Signature of this switching is present in the peak values of X. Our simulations shows that complex lattice can be stabilised and the symmetry of the lattice can be changed at will. Note that at each switching of the projection matrix P, the density of the lattice has been reduced by increasing the size of the simulation box. This is done in order to avoid kinetically arrested states. 58

5.6 Configurations showing the recovery of the square lattice after an initial distortion: **a.** The square lattice of 2500 GCM particles at $\rho = 0.5$ and $T = 1 \times 10^{-3}$ was distorted by displacing alternate rows of particles by half a lattice spacing (see schematic inset) producing a triangular lattice close to the S_E structure (**i**). Under a stabilising field of $h_X = -2.0$ the target lattice quickly recovers as seen in **ii** (4.8×10^4 MCS) and **iii** (24×10^4 MCS). **b.** Here we produce a patch of triangular lattice within a square matrix (**i**) and again let the solid recover the square structure: (**ii** and **iii** as above) under the influence of the same field as in **a**. The particles are coloured according to the value of the local χ values. 60

5.7 The resulting $P(\chi)$ at the end of runs Fig. 5.6**a** (red circles) and Fig. 5.6**b** (blue squares), the solid line is the harmonic theory prediction [7]. 61

6.1 Schematic of a swarm of bots (blue dots) the solid black lines joining the bots are a guide to the eye. 67

6.2 Typical time evolution ($t_1 < t_2 < t_3$) of the ring in the presence of turbulent field and active harmonic forces. Configurations obtained are for turbulent field strength $V_0 = 1.1$ and force stiffness $K = 500$. Background color represents the vorticity values of the turbulent field. Time t_1 show the initial configuration of the system. Clearly, the ring pattern of active particles is not stable if harmonic interactions are considered. Black solid lines are for visual guidance. 71

6.3 Reference structure and coarse-graining volume Ω. **a.** Model A : Floppy Swarm, Active particle spaced equally on a ring. Around particle i coarse-graining volume (pink shaded) is defined and consists two left and right neighbours. **b.** Model B : Rigid Swarm, Active particles equally spaced on a ring (dark blue) surrounded by layer of concentric ghost particles (light blue). Coarse-graining volume (pink shaded) around particle i consists of total 8 particles. 72

6.4 Model A: Time evolution ($t_1 < t_2 < t_3$) of model-A for different strength of non-affine force $h_X = -200, -1000$ and $V_0 = 1.1$. Background color represents the vorticity values of the turbulent field. Clearly, transformations of the circular ring to elliptical shapes are allowed and cost no energy because these shapes are related to the reference circle by an affine transformation. Solid black lines are for visual guidance. 75

6.5 Model A : **a.** Variation of $< X >$ with respect to strength of non-affine forces h_X. A decrease in value of $< X >$ shows the stability of the patterned as strength of non-affine field is increased. **b.** Variation of $< X >$ with respect to strength of non-affine forces V_0. Increase in value of $< X >$ with increase in strength of velocity V_0 indicates the destabilising effect of turbulent flow. **c.** Scaling form, $< X >$ varies linearly with $V_0^2/|h_X|$. . . . 76

6.6 Model B: Time evolution ($t_1 < t_2 < t_3$) of model-A for different strength of non-affine force $h_X = -0.4, -1.6$ and $V_0 = 1.1$. Background color represents the vorticity values of the turbulent field. Clearly, due to presence of ghost particles active particles in a definite ring pattern is stabilized. . . . 77

6.7 Model B: **a.** Variation of $< X >$ with respect to strength of non-affine forces h_X. A decrease in value of $< X >$ shows the stability of the patterned as strength of non-affine field is increased. **b.** Variation of $< X >$ with respect to strength of non-affine forces V_0. Increase in value of $< X >$ with increase in strength of velocity V_0 indicates the destabilising effect of turbulent flow. **c.** Scaling form, $< X >$ varies linearly with $V_0^2/|h_X|$. . . . 77

6.8 Model-A: **a.** Time series of total power spent by the active forces. **b.** Time series of average value of X in the steady state. Both **a.** and **b.** are obtained for the value of $N = 32$, $h_X = -1000$ and $V_0 = 0.3$ averaged over 30 different realisations of the flow field. 78

6.9 Model-B : **a.** Time series of total power spent by the active forces. **b.** Time series of average value of X in the steady state. Both **a.** and **b.** are obtained for the values of $N = 128$, $h_X = -2.0$ and $V_0 = 1.0$ averaged over 20 different realisations of the flow field 79

6.10 Distribution of time series of averaged power around zero for **a.** Model-A and **b.** Model-B obtained for the parameters as in Fig 6.8, 6.9. The peak of the distribution indicates the energy-efficiency of the stabilization algorithm. 80

6.11 Plot of longitudinal structure factor $S^{||}(r)$ as a function of distance r measured at Eulerian points (solid line), using velocities of individual particles(blue diamond), and using non-affine forces (yellow dots). The simulation was done for the ring size of radius $R_s = 2$, box size $L = 40$ and for $N = 128$ particles. In above the parameters were set to, **a.** for Model A, $V_0 = 0.1$, $h_X = -1000$ and **b.** for Model B $V_0 = 1.0$, $h_X = -2$. For dots and diamonds, simultaneous binning was done on distances and the value of structure factor. It is observed that for model B, the statistics for the underlying turbulent field can be obtained solely through the non-affine forces. 81

6.12 Plot of term II of Eq. (6.21) as a function of time for both Model A (red) and B (blue). The term II is averaged over 50 different realization of the flow field evaluated for the set $(h_X, V_0) = (-1000, 0.1)$ and $(-2, 0.1)$ for Model A and B respectively. For better statistics sum over all equivalent pair of $i - j$ are considered. 83

6.13 Non-affine correlation between particle $i = 0$ and j for Model A and B. The correlations are obtained for values same set of parameters as in Fig. 6.12 averaged over 50 different realisations of the flow field. For better statistics, further averaging over equivalent pair with fixed $i - j$ is done. 84

B.1 Square lattice with tagged particles used to create coarse-grained set Ω. The pink shaded region represents coarse-graining region around particle 0 with coordinates $\mathbf{R}_0 = (0, 0)$. The coarse-grained set $\Omega(0)$ consists nearest and next nearest neighbours. Similarly, coarse-graining volume for particles is also constructed (see text). 104

List of Tables

3.1 The Frobenius norm (the square root of the sum of the absolute squares of the elements) of the commutator $[\mathsf{P}, \mathsf{C}]$, made dimensionless by dividing it by the corresponding norm of C, for a number of lattices in 2d and 3d at $\beta = 1$. Corresponding parameter values for stiffness are quoted in the last column. Also note that the norm of P is essentially the square-root of total number of non-affine modes in each case. 40

1

Introduction

1.1 Order and fluctuations in systems of particles

Ordered arrangements of atoms are quite common in nature, For example, a crystalline solid is formed from the liquid when translation and orientation symmetries are broken as a result of a thermodynamic phase transformation [1]. Similar liquid to crystalline phase transitions are observed when macroscopic colloidal particles spontaneously arrange themselves into ordered crystals [8–11]. Even in an amorphous solid, such as a glass [12–15], where no obvious order is discernible, one may still argue that translational and orientational degrees of freedom are frozen, giving rise to a fixed, though random, arrangement of atoms. Ordering, in some cases may also have a purely dynamic, as opposed to thermodynamic origin such as in active, ordered flocks of birds, schools of fishes or swarms of insects or even inanimate objects such as colloidal particles acted upon by non-equilibrium forces [16–19]. Clearly, in the latter case, the role of “atoms” are being played by the active particles (birds, fishes, insects etc.). In this thesis, we shall interchangeably use the word atom or particle to describe the discrete entities whose ordering is of interest.

In all of these cases, fluctuations tend to destabilise order. At any non-zero temperature, atomic fluctuations in the crystalline solid tend to restore the symmetries that gave rise to crystallisation [1]. This is true even for dynamically ordered structures, for example active flocks or swarms, where random fluctuations of direction of the velocity arising either from internal noise or coupling to external fluctuating fields, such as a turbulent flow of wind or water, introduces disorder [20].

Within the current accepted paradigm, one classifies fluctuations in atomic positions as being either “smooth” or “singular”. The former comprise long wavelength, smooth variations of the elastic displacements and density fields [21, 22] where the local connectivity or the local neighbourhood of atoms is not disturbed significantly. In contrast, the latter are *defects*, where the displacement becomes discontinuous [3, 23, 24] leading to topological changes in the local neighbourhood. Such a classification has proved to be immensely useful in understanding many commonly observed properties of solids [2] as well as melting [1] and failure of solids in response to external mechanical loads [3, 4]. This viewpoint has also been extended with some success towards understanding the mechanical properties of amorphous solids [25]. However, in contrast to crystals, the lack of long ranged structural order in amorphous solids precludes a clear distinction between continuous and discontinuous displacements [25–29]. In active flocks too, the interaction between smooth and neighbourhood changing, singular, displacement fluctuations have a profound effects on the orientation and stability of the flock [20].

In this thesis, we study a different way of classifying fluctuations of the displacement field in particle systems [5–7, 30–40] which, has produced many insights on the nature of ordering. We begin with an idea first used to study mechanical deformation in glasses [41], it was shown that any set of atomic displacements of an atom and its neighbors, within a specified "coarse graining" region, may be decomposed into two mutually orthogonal sub-spaces using a well defined projection formalism [5–7]. The *affine* component of these displacements represents homogeneous linear transformations of a reference configuration within the coarse graining volume. Ignoring trivial uniform displacements, these are isotropic expansion, shear strains and local rotations. Since, in general, not all displacements can be described completely by these linear transformations, inevitably, a *non-affine* component remains. By construction, the affine and the non-affine parts of the displacements are linearly independent [5]. Conjugate fields may be defined, which enhance or suppress each part independently of the other. The affine displacements couple to local stresses (and torques) while the non-affine component of the displacement couples to a new "non-affine" field [6, 35–37].

Enhancing non-affine fluctuations by increasing temperature, applying large strains or the non-affine field leads to the creation of defects [6, 31, 37]. Indeed, atomic fluctuations that act as precursors to the formation of defects such as dislocation dipoles have been shown to be the most prevalent, though not the sole, non-affine displacement even within a small oscillation, harmonic, approximation [6, 31]. On the other hand, one may also suppress non-affine displacements by changing the sign of the conjugate field. The system of particles is now structurally stabilised such that the formation of defects and consequent changes in the local neighbourhoods surrounding every atom is precluded. We show in this thesis that this is sufficient, under certain conditions, for stabilising the system of particles into any desired lattice symmetry regardless of inter-atomic interactions among the particles.

The rest of this chapter is organised as follows. In the next section (Section 1.2) we introduce the two main categories of particulate systems for which details of atomic displacement fluctuations may be extracted viz atoms in a computer or experiments with colloidal particles. A practical reason for studying displacement fluctuations is that it allows one to estimate elastic moduli through the fluctuation response theorem [1]. We briefly review these attempts in Section 1.3. This is followed by an overview and summary of the rest of the thesis in Section 1.4.

1.2 A crystal in a box: statistics of atomic fluctuations

Till the middle of the last century, our knowledge of displacement fluctuations of atoms in a solid was at most indirect, based on, say, measured Debye-Waller factors of X-ray diffraction peaks for crystals [1]. The relative intensity of the diffraction peaks as a function of the wave number gives a measure of the mean squared fluctuations of atoms about their mean positions. The mean positions of atoms in solids became observable due to the invention of field-ion microscopes by Müller and Bahadur in 1955 [42]. About the same time, Alder and Wainwright [43] invented the technique of molecular dynamics where atomic trajectories could be followed in detail by solving Newton's laws in a digital computer; initially for just 100 hard spheres. Since then, of course, molecular dynamics simulations have been used to obtain microscopically detailed data for up to a trillion (10^{12}) atoms [44]. While access to microscopic time resolved data for atomic displacements in real atomic solids is still elusive, experimental systems namely, "colloidal crystals" offer a way to access this information [8, 9, 45–47]. We now discuss briefly how information from fluctuations can be used to obtain macroscopic elastic properties from simulations and experimental data on colloidal solids.

1.2.1 Computer simulations

Computer simulations of atomic systems [48] fall into two broad categories. In the first category one lists methods where equations of motion are solved. When dissipationless Newton's laws are numerically solved using discrete time steps, this is a molecular dynamics (MD) simulation. Alternately, depending on the experimental situation of interest, one may also solve the Langevin equation that involves viscous forces. In the second category comes simulation methods where one is interested only in the equilibrium ensemble and dynamical information is not needed. In such cases, one uses Monte Carlo (MC) methods where a Markov chain of configurations are generated using a suitable scheme such as the Metropolis algorithm. Besides, certain class of relaxation phenomena can be studied using Monte Carlo methods as well. There are many excellent textbooks which explain these methods in detail [48, 49]. In this thesis we report results obtained from MD simulations, performed using the open source LAMMPS code [50, 51], as well as Langevin dynamics and MC simulations performed with codes developed in-house.

All computer simulation methods require that the nature of the interactions between the particles constituting the solid be known. Details of the interaction potentials used are described at appropriate places in the thesis.

1.2.2 Experiments with colloidal solids

Colloidal crystals are composed of particles of silica, latex, microgels etc. with sizes ranging from 100 nm to a few microns and suspended in a fluid due to mutually repulsive forces of steric or electrostatic origin [8–11, 45–47, 52]. Under suitable conditions, these particles can arrange themselves into periodic lattices, vibrating around their ideal positions due to Brownian motion. There are now many different kinds of colloidal crystals possible. One may obtain extremely pure defect free crystals using super-paramagnetic colloidal particles trapped at a liquid solid interface [53, 54]. These particles interact with long-ranged dipolar interactions whose strength may be manipulated using an external magnetic field. Using a magnetic field which has a small amplitude oscillating component, one can anneal out defects and obtain large defect-free crystalline arrangements of these colloids. Charge stabilized colloids [8, 52, 55] on the other hand are stabilized by electrostatic repulsion between charges of the same (usually positive) sign on the colloidal particles, which are screened by counter-ions in the aqueous medium within which these particles are suspended. The interactions in this case may be controlled by introducing salt, which changes the screening length. Crystalline states of charge stabilized colloids occur when salt concentration is low and screening length large. Sterically stabilized colloids [48] have silica particles that have their surfaces covered by a layer of polymenrs. Entropic forces prevent two such colloidal particles from coming close to each other and thereby prevent aggregation. The density of these particles as well as the size of the surface polymers decide whether the colloid remains in the fluid state or crystallizes. In ionic microgel colloidal particles [56] the interaction potential can be manipulated by temperature as well as electric field. The size of these particles depends on the amount of cross-linking present in the polymers within each particle that determines the quantity of water retained and hence the size. These particles shrink as temperature is increased and the system can undergo a re-entrant liquid to crystal transition.

Colloidal particles can also be manipulated using light. Since these particles are dielectric, they tend to accumulate towards regions where the intensity of light is high. There has been a lot of work related to studying the effects of external, standing wave laser patterns on colloids [57–59]. Colloidal solids may also be manipulated using laser tweezers creating defects such as dislocations and grain boundaries [1, 59, 60]. The main advantage for studying colloids is that these particles may be readily observed using optical microscopic techniques and thus information at the microscopic, "atomic" level may be obtained with nothing much more than a camera and particle tracking software [47, 61]. Since time scales of motion of these particles are large, even non-equilibrium processes, such as phase transformation kinetics, may be studied [32].

1.3 Elastic constants from atomic fluctuations

Once instantaneous atomic positions $\{\mathbf{r}_i\}$ are available either from computer simulations or from experiments on colloidal particles, a host of mechanical and other information may be obtained by analysing this data. The advantage of this procedure is that when $\{\mathbf{r}_i\}$ are obtained, the subsequent analysis may be carried out without knowing the nature of the system or inter-particle interactions - the analysis is agnostic to all these details. We now describe past work [61–63] where this information has been used to obtain elastic moduli of crystalline solids.

Atomic fluctuations need to be analysed with respect to a reference configuration. This is either the ideal lattice positions at a particular density and temperature or simply the position of the tagged particles averaged over the entire data set. In what follows, and in all the work presented in this thesis, the existence of a tagged reference is essential. There are several advantages and at least one disadvantage of this approach, namely, the analysis becomes untenable if defects are produced or existing defects annihilate each other. Therefore, we first review the calculations where defect-free crystals are analysed and mention other approaches where this restriction is, at least partially, relaxed.

1.3.1 The defect free case

The elastic moduli of crystals are related to the equal time equilibrium spatial correlation functions of the local strains. The local strains may be obtained by either computing spatial derivatives of the atomic displacements away from the tagged reference lattice [62] or by fitting an average deformation matrix which best describes the instantaneous positions when operated on the reference coordinates [47, 61]. The latter procedure is identical to the one used in this thesis and will be described in detail in Chapter 2. Elastic strains are then the symmetric part of the fitted deformation matrix.

The local strains around each particle are used to obtain the equilibrium strain-strain correlation functions. Integrating the strain-strain correlation function over subsystems, one obtains a length scale dependent estimate of the elastic compliance. Finally, a finite size scaling procedure may be used to obtain the compliance matrix or it's inverse, viz, the elastic moduli in the thermodynamic limit. These estimates have been shown to be in excellent agreement with elastic moduli obtained in simulations and experiments by other means [47, 61, 63].

1.3.2 The crystal with defects

In this thesis, as mentioned already, we use a tagged reference configuration in order to obtain the atomic displacements and strains. A tagged reference configuration consists of the set of positions of tagged or numbered lattice sites. This means that it is necessary to maintain a one to one correspondence between each point in the reference configuration and an atom. Atomic exchanges are not allowed. Similarly, creating and annihilation of point and topological defects also cannot be considered. While, this is indeed a restriction, for ideal crystals far away from melting or under small deformation loads this restriction does not prevent us from obtaining useful results. Nevertheless, there has been some attempts at relaxing this restriction, which we describe briefly below.

One way to remove dependence on a tagged reference configuration is to focus on the local density $\rho(\mathbf{r}) = \sum_i \delta(\mathbf{r} - \mathbf{r}_i)$ which may be computed from the the atomic positions $\{\mathbf{r}_i\}$. In a crystal, this quantity is a periodic function, peaked at every lattice point at the centre of every unit cell. Mutual exchanges of particles across unit cells does not change $\rho(\mathbf{r})$. While in an ideal crystal where every lattice site is occupied, the integral $\int_{cell} \rho(\mathbf{r}) d\mathbf{r} = 1$. Presence of point defects such as vacancies and interstitial change this value away from unity. Hydrodynamic equations for variations of the local density of atoms and vacancies in the crystal may be written down formally [22, 64, 65].

Theoretical approaches, such as the density wave theory of Ramakrishnan and Yussouf [66, 67] connect the shape of $\rho(\mathbf{r})$ to the elastic constants. This connection involves the second functional derivative of the Helmholtz free energy of the crystal with respect to variations of $\rho(\mathbf{r})$, known as the direct correlation function $c(\mathbf{r}, \mathbf{r}')$. This function is not known for the crystalline solid. Note that while this is related to its structure factor measured in X-ray or neutron diffraction experiments [1], obtaining $c(\mathbf{r}, \mathbf{r}')$ for a solid from experiments (unlike a liquid) is non-trivial. In order to use this theory therefore, further, often uncontrolled, approximations are required, showing that discarding the tagged reference configuration comes at a price. Nevertheless, there has been some progress in using a density functional and hydrodynamic framework for obtaining elastic constants of colloidal crystals containing point defects [68, 69].

1.4 Non-affine displacements: a summary of the thesis

In this thesis, we present a systematic study of atomic fluctuations using the decomposition of displacements into affine and non-affine components. We shall see that this decomposition leads to a deeper understanding in several disparate contexts apart from merely providing a way to compute elastic constants. We shall see the connection between stability of a global pattern and local connectivity as encoded in the tagged reference. This will give us insights into the kinds of fluctuations that are benign, i.e. do not destroy order in any substantial way and those which do. This insights is then put to practical use for stabilising colloidal crystals and swarm of self propelled robotic agents such as swarm of drones [34–36].

After a detailed presentation of the projection formalism in Chapter 2, we begin with a study of small amplitude non-affine displacements in periodic crystals in order to discover features that are common to all crystalline solids and differentiate them from those that depend on details of the crystal structure, dimensionality and interaction parameters. This work is presented in Chapter 3 [34]. The eigenvalue spectrum of the Hessian of the coarse-grained Hamiltonian taken with respect to local atomic displacements and projected onto the non-affine subspace [6], always shows a prominent *gap* between the largest eigenvalues and the others, for all Bravais lattices with a mono-atomic basis that we have investigated (cubic family in 3d; hexagonal and tetragonal family in 2d). The gap increases with the size of the coarse graining volume. For open lattices featuring a multi atom basis, the gap is much less prominent, although large eigenvalue floppy modes continue to resemble precursors for known defects [34]. The relative prominence of modes in the non-affine eigenvalue spectrum for open lattices is more sensitive to the nature of the interactions compared to those in close packed crystals. Spatial correlation functions of the affine and non-affine modes are similar in nature among the various crystal structures studied. Affine and non-affine modes couple at higher order in displacements [5]. This coupling measures the susceptibility of the crystal to producing non-affine displacements in response to small external stress. We find that open crystals (lattice with a multi-atom basis and have lower packing fraction than the close packed structure such as triangular lattice) are more susceptible than close packed ones by almost an order of magnitude.

In Chapter 4 we study in detail the relation between lattice defects and the prominent non-affine modes [34]. The dominant non-affine eigenmode corresponding to the largest eigenvalue features displacements that may be identified with defect precursors [6, 7]. We show that in the 2d triangular lattice, this dominant non-affine displacement mode generates slip along a close packed plane while in the 3d FCC lattice the dominant non-affine displacements produce local deviations in crystallographic planes generating slips and stacking faults. [1, 3].

In Chapter 5 we show how atomic displacements in colloids may be manipulated and colloidal crystals with any given interaction may be arranged in any structure whatsoever if it is only possible to suppress non-affine displacements away from this reference configuration. Special, dynamic, feedback controlled laser traps have been proposed, though not yet experimentally realized, which may be able to perform this feat. Unlike static traps, the structures stabilized by such a process are translationally invariant and possess all allowed zero modes [35].

Finally, in Chapter 6 we go beyond atomic and colloidal solids and show that the ideas discussed in this work may also be used to stabilize swarms of autonomous robotic agents [16, 17, 20, 36, 70, 71] which are able to communicate with each other and modify their motion depending on their local configuration. Suppressing non-affine displacements in these swarms leads to stabilisation of any desired pattern.

We finally conclude the thesis in Chapter 7 with a brief review of the work presented and potential future directions along with other important and active work on non-afffine displacements.

2

The projection formalism for non-affine displacements

In this chapter, we present the method we use to project out local atomic displacements into affine and non-affine components. In the most general setting, non-affine displacements are those atomic displacements that cannot be captured by a homogeneous deformation. For example, imagine an ideal (defect free) crystal at zero temperature consisting of atoms placed at their reference position. The Cauchy-Born rule [72] (CBR) states that any external deformation caused by changing the shape of the boundary of the solid is distributed homogeneously among the atoms of the crystal, which are shifted appropriately from their reference position. This, of course, amounts to stating that for an ideal crystal there are no non-affine deformations at zero temperature. At finite temperature, one expects this rule to hold on the average, with the (finite size scaled) elastic moduli [47, 61] setting the scale for the displacement fluctuations averaged within some local coarse graining volume Ω.

While this is more or less true, there is a subtle point here that needs attention. Indeed, atomic displacement fluctuations within Ω decompose naturally into *two* mutually orthogonal subspaces. One, designated as affine, consists of fluctuations for which the CBR holds locally and instantaneously, while the other is the set of non-affine displacement modes for which the CBR is violated. While the former may be directly connected to the elastic moduli, the latter represents fluctuations that act as precursors for defects.

We elaborate this decomposition principle in this and the next chapter and show explicitly the connection to lattice defects in chapter 4.

2.1 The Falk-Langer least square fit formalism

Solids are characterised by their structural rigidity and resistance to small applied strain [2]. However, for large strains, solids (crystalline or amorphous) may deform plastically [73]. For crystalline solids, this is often understood in terms of the dynamics of lattice defects, such as dislocation dipoles($2d$) or loops($3d$) [3]. On the other hand, identification of such defects in amorphous solids is challenging due to the lack of long-range structural order. However, particle rearrangement responsible for the plastic flow of an amorphous solid is localised [41, 74]. Such localised regions, otherwise known as “Shear Transformation Zones(STZ)”, flow faster than the rest of the material and have led to several phenomenological theories of plastic deformation [25]. The idea of non-affine displacements originated first, as a way to identify STZs from configurations obtained from simulations of amorphous solids. We use a modified version of this original formulation as described below.

Under an applied stress, particles undergo displacements $\{\mathbf{u}_i\}$ relative to a chosen reference configuration $\{\mathbf{R}_i\}$. In this microscopic picture, Falk and Langer [41] identified STZ as the regions where the particle displacements deviate substantially from those generated by a local homogeneous strain field. Therefore, the least square residual (χ) associated with site i, is defined to identify STZ,

$$\chi_i = \min_{\mathcal{D}} \sum_{j\in\Omega} \left[(\mathbf{u}_j - \mathbf{u}_i) - \mathcal{D}\left(\mathbf{R}_j - \mathbf{R}_i\right)\right]^2, \tag{2.1}$$

where $\mathcal{D}$ is a homogeneous strain field which closely approximates the actual particle displacements. The sum over j extends over the set Ω consisting all the neighbours in the interaction range of particle i. The component of particle displacements which can be represented by the best fit strain field, i.e. $\mathcal{D}\left(\mathbf{R}_j - \mathbf{R}_i\right)$ is termed as affine and the component which cannot is called non-affine. This decomposition of particle displacements into affine and non-affine parts is more profound and not limited to the deformation of amorphous solids due to external loads. In principle, any system micro- or macroscopic, regardless the underlying source of deformation, particle displacements away from specified reference configuration can always be decomposed into affine and non-affine parts.

In their original formulation, the positions $\{\mathbf{R}_i\}$ were chosen as the instantaneous positions of the atoms at some earlier time step. This is necessary for amorphous configurations where a natural choice for ideal atomic positions does not exist. In a crystal, on the other hand, the zero temperature ($T = 0$) ideal lattice positions provides a natural choice for the reference $\{\mathbf{R}_i\}$. This choice of the reference is used in next section and the rest of the thesis.

2.2 The projection method for lattices with mono-atomic basis

In the view of section 2.1, particle displacements in a disordered solid under external load carries a non-affine component. Presence of this non-affine part, even at zero temperature, is primarily due to inhomogeneities where the space dependent elastic constants change the local environment in a solid. For a homogeneous crystalline solid, displacements due to external stress $\mathbf{\Sigma}$ are affine and can be expressed as a linear transformation of the reference configuration, $\mathbf{u}_i = \mathcal{D}\mathbf{R}_i$. Here, $\mathcal{D}$ is the local deformation tensor and obeys the constitutive relation $\mathcal{D} = \mathsf{K}^{-1}\mathbf{\Sigma}$, where K being the matrix of elastic constants. At finite temperature, non-affine displacements in homogeneous solids may also arise purely due to thermal fluctuations.

A previous study [5] on a crystalline network of harmonically bonded particles revealed that any thermal distortion of coarse-graining region Ω can be decomposed into affine and non-affine parts using a well defined projection formalism. Furthermore, the statistics of non-affine fluctuations and the affine distortion $\mathcal{D}$ was obtained by integrating out phonons with wavelength comparable or smaller than the coarse-graining volume. Below, we briefly outline the projection formalism which was utilised to study mono-atomic lattices and state significant outcomes of the earlier studies [5–7, 30–33].

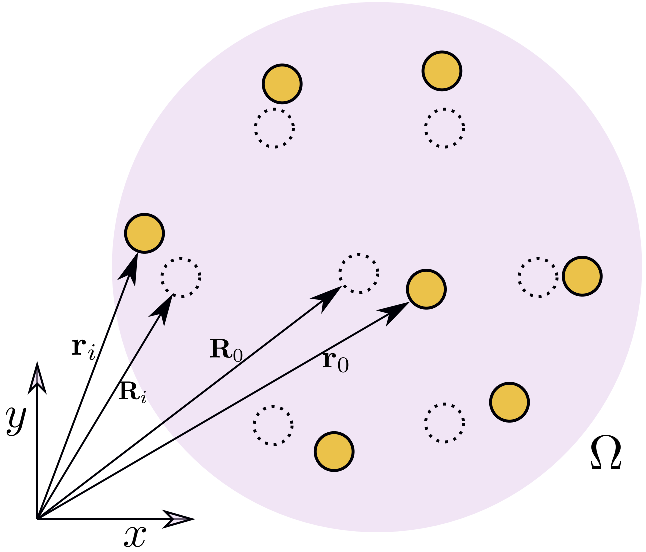

Fig. 2.1. Schematic showing coarse-graining volume Ω around set of particles arranged in triangular lattice. Dotted circle represents zero temperature reference position and colored circles are the instantaneous positions.

Consider a d-dimensional lattice with N lattice sites in thermal equilibrium. For particles in our system, we denote $\{\mathbf{u}\}$ be the set of displacement vectors away from the zero temperature reference configuration $\{\mathbf{R}\}$. Next, around any particular particle 0, a coarse-graining volume Ω consisting all the nearest neighbours of particle 0 is constructed (See Fig. 2.1). For any distortion of Ω consisting N_Ω particles, displacements consists both affine and non-affine part. In such cases (discussed in Sec. 2.1), a local affine deformation tensor is defined which minimises Eq.(2.1)

$$\chi_0 = \min_{D} \sum_{i\in\Omega} \left[(\mathbf{u}_i - \mathbf{u}_0) - \mathcal{D}\left(\mathbf{R}_i - \mathbf{R}_0\right)\right]^2 .$$

Here, χ measures the non-affinity in coarse-grained region Ω around particle 0. Since all lattice sites are equivalent, therefore the subscript can be dropped from χ_0.

To simplify the notation, relative displacements $(\mathbf{u}_i - \mathbf{u}_0)$ for all i were arranged into a $N_\Omega d$ dimensional block column vector $\boldsymbol{\Delta}$ such that element $\Delta_{i\alpha}$ represents α^{th} spatial component of relative displacement of particle i. In the similar fashion, elements of $\mathcal{D}$ are arranged in a d^2 dimensional vector $\mathbf{e} = (\mathcal{D}_{11}, \mathcal{D}_{12}...\mathcal{D}_{1d}, \mathcal{D}_{21}...\mathcal{D}_{N_\Omega d})$. With this notation, the above equation can now be expressed as,

$$\chi = \min_{\mathbf{e}} \left[\boldsymbol{\Delta} - \mathsf{Re}\right]^2 , \tag{2.2}$$

where R is a $N_\Omega d \times d$ dimensional block matrix with elements $\mathsf{R}_{i\alpha,\gamma\gamma'} = \delta_{\alpha\gamma}\left(R_{i\gamma'} - R_{0\gamma'}\right)$. The minimisation of Eq.(2.2) yields

$$\mathbf{e} = \mathsf{Q}\boldsymbol{\Delta}, \tag{2.3}$$

$$\chi = \boldsymbol{\Delta}^{\mathrm{T}}\mathsf{P}\boldsymbol{\Delta}. \tag{2.4}$$

Considering I as the identity matrix, one has,

$$\mathsf{P} = \mathsf{I} - \mathsf{RQ} \tag{2.5}$$

$$\mathsf{Q} = (\mathsf{R}^{\mathrm{T}}\mathsf{R})^{-1}\mathsf{R}^{\mathrm{T}}. \tag{2.6}$$

Note that the local homogeneous strain field $\mathbf{e}$ minimises Eq.(2.2) and provides the affine part of the deformed Ω. Evidently, matrix P and Q depends only on the zero temperature reference configuration and satisfies the following properties,

- P is a $N_\Omega d$ dimensional symmetric matrix, i.e., $\mathsf{P}^{\mathrm{T}} = \mathsf{P}$

- P is idempotent, i.e., $\mathsf{P}^2 = \mathsf{P}$

$$\begin{aligned}
\mathsf{P}^2 &= \left[\mathsf{I} - \mathsf{R}(\mathsf{R}^{\mathrm{T}}\mathsf{R})^{-1}\mathsf{R}^{\mathrm{T}}\right]^2 \\
&= \mathsf{I}^2 - 2\mathsf{R}(\mathsf{R}^{\mathrm{T}}\mathsf{R})^{-1}\mathsf{R}^{\mathrm{T}} \\
&+ \mathsf{R}(\mathsf{R}^{\mathrm{T}}\mathsf{R})^{-1}\left[(\mathsf{R}^{\mathrm{T}}\mathsf{R})(\mathsf{R}^{\mathrm{T}}\mathsf{R})^{-1}\right]\mathsf{R}^{\mathrm{T}} \\
&= \mathsf{P}.
\end{aligned} \tag{2.7}$$

- Since, P is idempotent, its eigenvalues are either 0 or 1. More precisely, the projection matrix P has d^2 zero eigenvalues and $N_\Omega d - d^2$ number of one eigenvalues correspond to affine and non-affine modes respectively.

- In a similar fashion, it is easy to show that $\mathsf{RQ} = \mathsf{I} - \mathsf{P}$ is also idempotent and has similar properties to P

- Note that $\mathsf{PQ}^{\mathrm{T}} = 0$.

Therefore, P being the projection matrix project out the non-affine component of $\boldsymbol{\Delta}$ with χ being the measure of non-affinity. Similarly $\mathsf{I} - \mathsf{P}$ projects onto the complementary space of affine deformations.

The statistics of χ and $\mathbf{e}$ is then obtained by considering the canonical distribution of the displacements $\{\mathbf{u}_i\}$ and momenta $\{\mathbf{p}_i\}$ at inverse temperature β. For harmonic interactions among particles with spring constant k and mass m, the Hamiltonian

$$\mathcal{H} = \sum_i \frac{\mathbf{p}_i^2}{2m} + \frac{k}{2}\sum_{\langle ij \rangle}((\mathbf{u}_i - \mathbf{u}_j)\cdot\hat{\mathbf{R}}_{ij})^2, \tag{2.8}$$

produces the displacements vector $\boldsymbol{\Delta}$ with a Gaussian distribution of mean zero and variance proportional to the temperature$(1/\beta)$. Non affinity χ, as defined, is quadratic in $\boldsymbol{\Delta}$, hence average thermal contribution to non-affinity can be measured.

$$\begin{aligned}
\langle\chi\rangle &= \mathrm{Tr}\left(\left\langle \mathsf{P}\boldsymbol{\Delta}\boldsymbol{\Delta}^{\mathrm{T}}\mathsf{P}\right\rangle\right) \\
&= \mathrm{Tr}\left(\mathsf{P}\left\langle\boldsymbol{\Delta}\boldsymbol{\Delta}^{\mathrm{T}}\right\rangle\mathsf{P}\right) \\
&= \mathrm{Tr}\left(\mathsf{PCP}\right),
\end{aligned} \tag{2.9}$$

that is the sum of the eigenvalues of PCP. In Eq.(2.9), we have used the properties of the projection matrix ($\mathsf{P}^2 = \mathsf{P}$) and that the scalar variable χ can be written as a trace of $\mathbf{\Delta}^{\mathrm{T}}\mathsf{P}\mathbf{\Delta}$. Here we have defined,

$$\mathsf{C} \equiv \langle \mathbf{\Delta}\mathbf{\Delta}^{\mathrm{T}} \rangle. \tag{2.10}$$

The covariance matrix C is a $N_{\Omega} \times N_{\Omega}$ block matrix with each block of size $d \times d$. Due to the lattice symmetries, not all the components of C are independent and overall one has real symmetric C matrix. The components of C are then obtained by assuming plane wave solution for the displacements,

$$\mathbf{\Delta}_i = \int \frac{d\mathbf{q}}{V_{BZ}} \mathbf{u_q} \left(e^{\mathbf{q}\cdot\mathbf{R}_i} - e^{\mathbf{q}\cdot\mathbf{R}_0} \right).$$

and integrating over all the wave-vectors $\mathbf{q}$ correspond to the first Brillouin zone with volume $V_{BZ} = \sum_{\mathbf{R}} \int d\mathbf{q} \exp(i\mathbf{q}\cdot\mathbf{R})$. Thus the components of C are

$$\begin{aligned} \mathsf{C}_{i\alpha,j\gamma} = \langle \Delta_{i\alpha}\Delta_{j\gamma} \rangle = & \frac{1}{\beta} \int \frac{d\mathbf{q}}{V_{\mathrm{BZ}}} D^{-1}_{\alpha\gamma}(\mathbf{q}) \left(e^{i\mathbf{q}\cdot\mathbf{R}_j} - e^{i\mathbf{q}\mathbf{R}_0} \right) \\ & \times \left(e^{-i\mathbf{q}\cdot\mathbf{R}_i} - e^{-i\mathbf{q}\cdot\mathbf{R}_0} \right). \end{aligned} \tag{2.11}$$

Here, $D(\mathbf{q})$ is the dynamical matrix and can be calculated analytically for any given harmonic lattice [2]. Likewise, we note that $\langle \mathbf{e} \rangle = 0$ due to the Gaussian distribution of $\mathbf{\Delta}$, but in the presence of external stress $\mathbf{\Sigma}$ linear response yields,

$$\langle \mathbf{e} \rangle_{\mathbf{\Sigma}} = \left\langle \mathbf{e}\mathbf{e}^{\mathrm{T}} \right\rangle_{\mathbf{\Sigma}=0} \mathbf{\Sigma}, \tag{2.12}$$

which is in accordance with the Hooke's law. The zero stress compliance is obtained in the same spirit of Eq.(2.9), hence $\langle \mathbf{e}\mathbf{e}^{\mathrm{T}} \rangle = \mathsf{QCQ}^{\mathrm{T}}$. This analysis, therefore, offers a way to obtain elastic constants from fluctuations of the affine part of the displacements [61–63]. The stress $\mathbf{\Sigma}$ is the thermodynamic conjugate to $\mathbf{e}$.

The projection matrix P depends on the reference configuration and is therefore exactly known. For the covariance matrix C, one can calculate numerically using Eq.(2.11), or through simulation. Once P and C are known matrix PCP can be diagonalised. It has $N_{\Omega}d$ eigenvalues of which d^2 are zero. Thermal average of non-affinity parameter is therefore sum of these non zero eigenvalues (Eq.(2.9)). The eigenvectors correspond to non zero eigenvalues gives the non-affine distortion of Ω and are shown in Fig. 2.2 for the case of two dimensional triangular lattice [5]. The structure of the null space of PCP can be understood as being spanned by the eigenvectors correspond to d^2 non zero eigenvalues of the complementary space $(\mathsf{I} - \mathsf{P})\mathsf{C}(\mathsf{I} - \mathsf{P})$. The affine modes for triangular lattice are shown in Fig. 2.3. These independently fluctu-

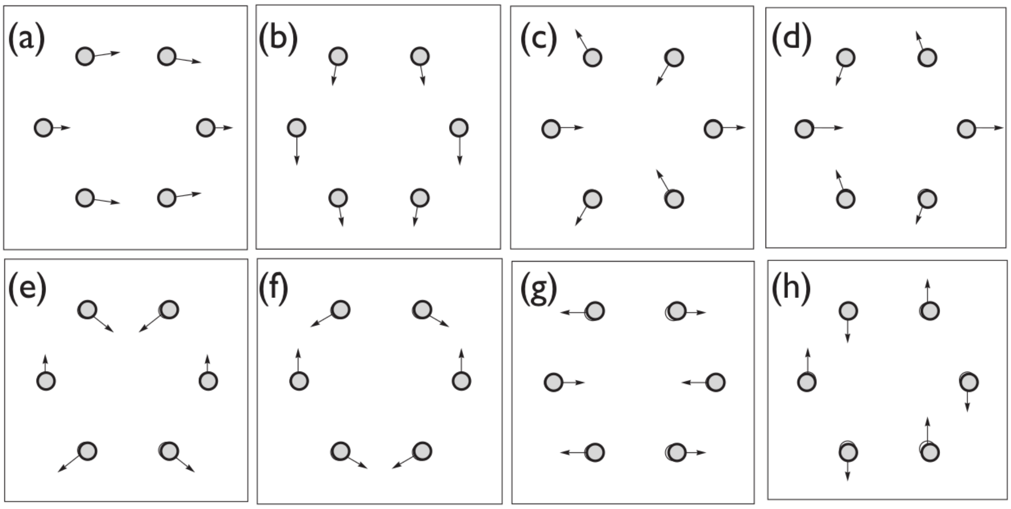

Fig. 2.2. From [5]. **(a)** to **(h)**, eigenvectors correspond to non zero eigenvalues of PCP for the case of triangular lattice. The $N_\Omega = 6$ resulting 12 eigenvalues in two dimensions. Four eigenvalues out of twelve are zero and correspond to affine modes and are shown in Fig 2.3.

ating affine and non-affine modes forms a complete basis for the distortion of Ω. Note that shuffle modes as discussed in Ref [75], is a special case of non-affine displacements discussed here.

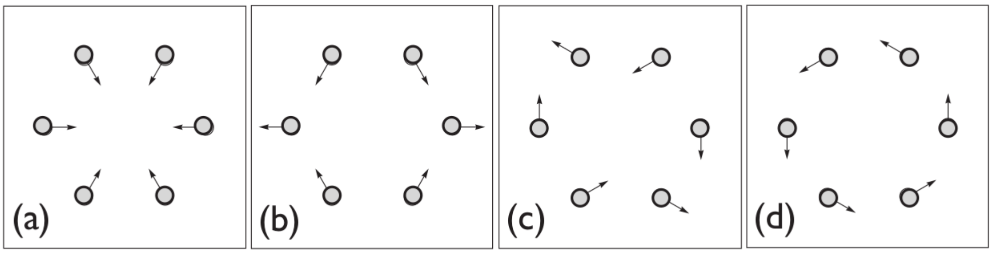

Fig. 2.3. From [5]. **(a)** to **(d)**, eigenvectors correspond to non zero eigenvalues of $(\mathsf{I}-\mathsf{P})\mathsf{C}(\mathsf{I}-\mathsf{P})$. The eigenvectors correspond to four non zero eigenvalues represents the affine transformation of the reference lattice, volume change, uni-axial strain, shear, and rotation.

For any observable $A(\mathbf{\Delta})$, thermal average over the coarse-graining can be obtained by microscopic Hamiltonian, thus,

$$\langle A \rangle = \frac{1}{Z_\Omega} \int \prod_{i\alpha} d\Delta_{i\alpha} A(\mathbf{\Delta}) \exp\left(-\frac{1}{2}\mathbf{\Delta}^{\mathrm{T}}\mathsf{C}^{-1}\mathbf{\Delta}\right) \tag{2.13}$$

with Z_Ω as a normalization constant. Taking $A = e^{ik\chi + i\boldsymbol{\kappa}^{\mathrm{T}}\mathbf{e}}$ in the above equation gives characteristic function $\Phi(k, \boldsymbol{\kappa})$ for the joint probability distribution of χ and e.

$$\begin{aligned}
\Phi(k,\boldsymbol{\kappa}) &= \left\langle e^{ik\chi + i\boldsymbol{\kappa}^{\mathrm{T}}\mathbf{e}} \right\rangle \\
&= \frac{1}{Z_\Omega} \int \prod_{i\alpha} d\Delta_{i\alpha} \times \exp\left[-\frac{1}{2} \boldsymbol{\Delta}^{\mathrm{T}} \mathsf{C}^{-1} \boldsymbol{\Delta} + ik\boldsymbol{\Delta}^{t} \mathsf{P} \boldsymbol{\Delta} + i\boldsymbol{\kappa}^{\mathrm{T}} \mathsf{Q} \Delta \right],
\end{aligned} \tag{2.14}$$

where, in above, we have used Eq.(2.3, 2.4). Completing the square followed by Gaussian Integral, above equation yields

$$\begin{aligned}
\Phi(k,\boldsymbol{\kappa}) =& \frac{1}{[|(\mathsf{I} - 2ik\mathsf{PCP})|]^{1/2}} \exp\left(-\frac{1}{2} \boldsymbol{\kappa}^{\mathrm{T}} \mathsf{QCQ}^{\mathrm{T}} \boldsymbol{\kappa} \right) \\
& \times \exp\left[-ik\boldsymbol{\kappa}^{\mathrm{T}} \mathsf{QC}(\mathsf{I} - 2ik\mathsf{PC})^{-1} \mathsf{PCQ}^{\mathrm{T}} \boldsymbol{\kappa} \right].
\end{aligned} \tag{2.15}$$

Marginal distributions now can be obtained by numerically inverting the characteristic function and appropriately setting k or $\boldsymbol{\kappa}$ equal to zero. Similarly, average of other higher moments can be obtained by taking appropriate derivatives of Eq.(2.15). Note that non-affinity χ and strain e couples at higher order. A straightforward implication of this coupling is seen in the presence of external stress. Upon substituting $\boldsymbol{\kappa} \to \boldsymbol{\kappa} - i\boldsymbol{\Sigma}$ in Eq.(2.15), one finds,

$$\langle \chi \rangle_{\Sigma} = \langle \chi \rangle_{\boldsymbol{\Sigma}=0} + \boldsymbol{\Sigma}^{\mathrm{T}} \mathsf{QC}[\mathsf{P},\mathsf{C}]\mathsf{Q}^{\mathrm{T}} \boldsymbol{\Sigma}. \tag{2.16}$$

Here, the components of matrix $\boldsymbol{\Sigma}$ have been arranged in a column vector accordingly. Interestingly, the contribution due to the external stress $\boldsymbol{\Sigma}$ depends on the commutator $[\mathsf{P},\mathsf{C}]$ that vanishes only in one-dimensional systems. Further, the first non-zero cross correlations of order $O(k\boldsymbol{\kappa}^2)$,

$$\langle \chi \mathbf{e}\mathbf{e}^{\mathrm{T}} \rangle - \langle \chi \rangle \langle \mathbf{e}\mathbf{e}^{\mathrm{T}} \rangle = 2\mathsf{QC}[\mathsf{P},\mathsf{C}]\mathsf{Q}^{\mathrm{T}}, \tag{2.17}$$

has a linear dependence on $[\mathsf{P},\mathsf{C}]$. For the triangular lattice, the above outlined correlation is zero only for the strains associated with rotation and isotropic volume change [5]. This is understood, as large stresses (mainly uni-axial and shear) change the local neighbourhood of particle significantly and thus contributes to non-affinity. To express cross correlations between higher moments of χ and e, higher order commutators of P and C are required, making $[\mathsf{P},\mathsf{C}]$ an important quantity to computed.

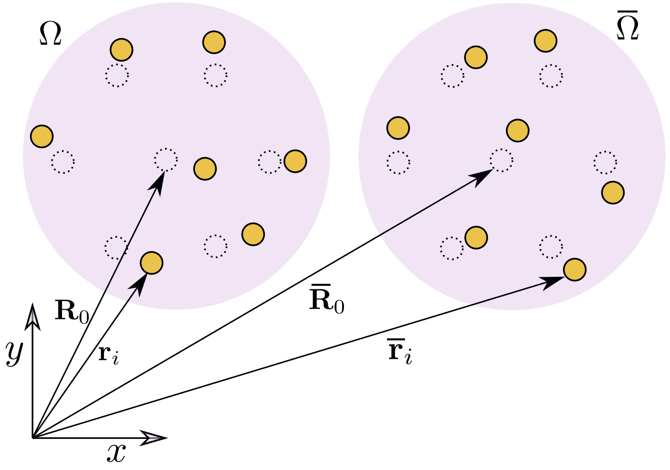

Fig. 2.4. Schematic showing the two coarse-graining volume for cross correlations.

2.2.1 Spatial direct- and cross- correlations

As discussed above, lattice symmetries ensures that the non-affine parameter calculated over two distant neighborhoods in a crystal (see Fig. 2.4) have the same thermal average. Spatial, two point correlations of non-affine parameters ($\chi \equiv \chi(\mathbf{R}_0)$, $\bar{\chi} \equiv \chi(\bar{\mathbf{R}}_0)$) is expressed as

$$\langle\chi\bar{\chi}\rangle - \langle\chi\rangle\langle\bar{\chi}\rangle = 2\mathrm{Tr}(\mathsf{P}\bar{\mathsf{C}}\mathsf{P})(\mathsf{P}\bar{\mathsf{C}}\mathsf{P})^{\mathrm{T}}. \tag{2.18}$$

In order to evaluate the joint covariance matrix $\bar{\mathsf{C}} \equiv \langle\boldsymbol{\Delta}\boldsymbol{\Delta}^{\mathrm{T}}\rangle$, one needs to simultaneously consider displacement differences in two coarse-graining region. A expression similar to Eq.(2.11) can also be obtained for the joint covariance matrix,

$$\bar{C}_{i\alpha,j\gamma} = \frac{1}{\beta}\int \frac{d\mathbf{q}}{V_{\mathrm{BZ}}} D^{-1}_{\alpha\gamma}(\mathbf{q})\left(e^{i\mathbf{q}\cdot\mathbf{R}_i} - e^{i\mathbf{q}\cdot\mathbf{R}_0}\right)\left(e^{-i\mathbf{q}\cdot\bar{\mathbf{R}}_j} - e^{-i\mathbf{q}\cdot\bar{\mathbf{R}}_0}\right). \tag{2.19}$$

The spatial correlation for χ decays exponentially for the triangular lattice [5, 6]. Similarly, strain-strain correlation are

$$\left\langle \mathbf{e}\bar{\mathbf{e}}^{\mathrm{T}}\right\rangle = \left\langle \mathsf{Q}\boldsymbol{\Delta}\bar{\boldsymbol{\Delta}}^{\mathrm{T}}\mathsf{Q}^{\mathrm{T}}\right\rangle = \mathsf{Q}\bar{\mathsf{C}}\mathsf{Q}^{\mathrm{T}}.$$

Provided the dynamical matrix of the lattice $D(\mathbf{q})$, these correlations are easy to evaluate in Fourier space Eq.(2.19). Using the Fourier component of $\bar{\mathsf{C}}$ from Eq.(2.19), strain correlations takes the following form,

$$\langle\mathbf{e}\bar{\mathbf{e}}^{\mathrm{T}}\rangle(\mathbf{q}) = \mathsf{Q}\bar{\mathsf{C}}(\mathbf{q})\mathsf{Q}^{\mathrm{T}}.$$

In the case of a triangular lattice with the harmonic Hamiltonian in Eq. 2.8, explicit expressions of strain correlations for volume change ($e_v = e_1 + e_4$), uni-axial ($e_u =$

$e_1 - e_4$), shear ($e_s = e_2 + e_3$), and local rotation ($\omega = e_2 - e_3$) obtained at long wavelength limit are

$$\begin{aligned}
(\beta a^2 k)\left\langle e_v^2 \right\rangle(\mathbf{q}) &\approx \frac{8}{9}, \\
(\beta a^2 k)\left\langle e_u^2 \right\rangle(\mathbf{q}) &\approx \frac{8}{9} + \frac{64}{9}\frac{q_x^2 q_y^2}{\left(q_x^2 + q_y^2\right)^2}, \\
(\beta a^2 k)\left\langle e_s^2 \right\rangle(\mathbf{q}) &\approx \frac{8}{3} - \frac{64}{9}\frac{q_x^2 q_y^2}{\left(q_x^2 + q_y^2\right)^2}, \\
(\beta a^2 k)\left\langle \omega^2 \right\rangle(\mathbf{q}) &\approx \frac{8}{3}.
\end{aligned} \tag{2.20}$$

Note that the combination of spring constant k, temperature $1/\beta$ and the lattice constant a is dimensionless. Therefore, the elastic constants of the triangular lattice may be obtained from the $\mathbf{q} \to 0$ limit of the correlations functions.

This completes the description of projection formalism used for mono-atomic lattices. In the next section, we first generalise the formalism to multi-atom basis and in d-dimensions and then use it to study various lattices in two and three dimensions. In subsequent chapters of the thesis, we use this formalism to study non-affine fluctuations in crystals and swarms.

2.3 Generalisation to lattices with multi-atom basis

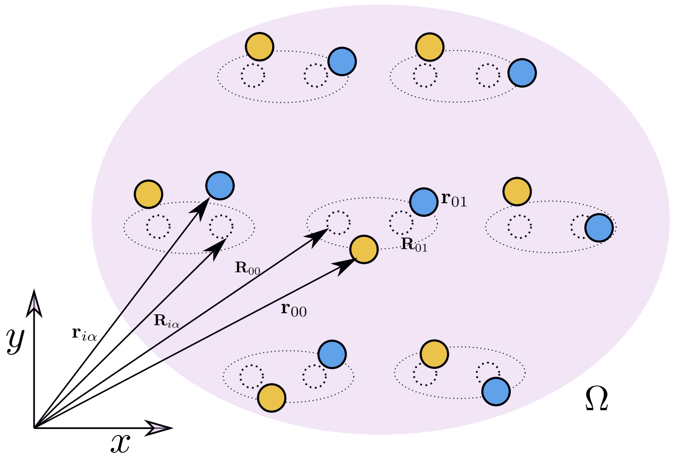

Fig. 2.5. Schematic showing coarse-graining volume Ω for lattice with basis. Different color represents two different basis atoms and dotted circles are zero temperature position of the particles. Each cell (dotted ellipse) denotes the lattice sites, here arranged in a triangular lattice. The particular schematic here has two basis atom, however, more basis atoms can be added.

We show below how this decomposition may be carried out for a generic crystalline solid. We consider a d dimensional lattice with N lattice sites and N_b basis particles per site. The total number of particles in the system is $N \times N_b$. We take $\{\mathbf{R}_{i\alpha}\}$ as the equilibrium position vector for any site $i \in \{0, 1, 2 \ldots N-1\}$, where $\alpha \in \{0, 1, 2 \ldots N_b - 1\}$ represents the index of a basis particle. To distinguish affine and non-affine displacements we consider relative displacements of pairs of atoms whose reference positions are within some fixed coarse-graining distance $\mathfrak{r}$ of each other (see Fig. 2.5). Specifically, the coarse-graining region around the basis on lattice site i is defined as

$$\Omega(i) = \{(j\gamma, i\alpha) | 0 < |\mathbf{R}_{j\gamma} - \mathbf{R}_{i\alpha}| \leq \mathfrak{r} \wedge (j \neq i \vee \gamma > \alpha)\}. \tag{2.21}$$

In words, $\Omega(i)$ contains all pairs of indices $(j\gamma, i\alpha)$ of particles within the specified distance $\mathfrak{r}$; at least one of these particles has to belong to the basis around lattice site i. The last constraint in Eq.(2.21) merely avoids double-counting of pairs *within* the basis, by insisting that index pairs of the form $(i\gamma, i\alpha)$ have got ordered basis indices, $\gamma < \alpha$. We denote the number of particle pairs in $\Omega(i)$ by N_Ω and number the elements of $\Omega(i)$ in some arbitrary fashion as

$$\Omega(i) = \{(j_n\gamma_n, i\alpha_n), n = 1 \ldots N_\Omega\}$$

We note that the lattice symmetries mean that all neighborhoods $\Omega(i)$ for different i are just translated copies of each other.

When the lattice is deformed particles undergo displacements and take new positions $\{\mathbf{r}_{i\alpha}\}$; we write the displacement from their equilibrium positions as $\mathbf{u}_{i\alpha} = \mathbf{r}_{i\alpha} - \mathbf{R}_{i\alpha}$. It has been shown [5–7] that the displacements in a given deformed coarse-graining volume can be expressed as a linear combination of independent affine and non-affine deformations. For a fully affine deformation of the coarse-graining volume around lattice site i there is by definition a local $d \times d$ dimensional deformation matrix $\mathcal{D}$ such that

$$\mathbf{u}_{j_n\gamma_n, i\alpha_n} = \mathcal{D}\mathbf{R}_{j_n\gamma_n, i\alpha_n}, \qquad n = 1 \ldots N_\Omega \tag{2.22}$$

using the abbreviations $\mathbf{u}_{j_n\gamma_n, i\alpha_n} = \mathbf{u}_{j_n\gamma_n} - \mathbf{u}_{i\alpha_n}$ and $\mathbf{R}_{j_n\gamma_n, i\alpha_n} = \mathbf{R}_{j_n\gamma_n} - \mathbf{R}_{i\alpha_n}$. In general, $\{\mathbf{u}_{i\alpha}\}$ will have contributions from non-affine transformations as well. In such cases $\mathcal{D}$ is defined as the matrix that minimizes

$$\chi_i = \min_{\mathcal{D}} \left(\sum_{n=1}^{N_\Omega} \left(\mathbf{u}_{j_n\gamma_n, i\alpha_n} - \mathcal{D}\mathbf{R}_{j_n\gamma_n, i\alpha_n}\right)^2 \right) \tag{2.23}$$

Therefore χ_i is a measure of the *non-affinity* at the given lattice site i.

We now introduce some simplified notation by rearranging components of $\mathbf{u}_{j_n\gamma_n} - \mathbf{u}_{i\alpha_n}$ for all n into a column vector $\boldsymbol{\Delta}$ of length $N_\Omega d$ with elements

$$\Delta_{n\mu} = u^{\mu}_{j_n\gamma_n,i\alpha_n}$$

where $\mu = 1 \ldots d$ denotes the spatial components of the displacement vectors. Similarly a column vector $\mathbf{e}$ of length d^2 is obtained by arranging the elements of $\mathcal{D}$ in order $(\mathcal{D}_{11}, \mathcal{D}_{12} ... \mathcal{D}_{1d} ... \mathcal{D}_{d1}, \mathcal{D}_{d2} ... \mathcal{D}_{dd})$. With these definitions, Eq. (2.23) may be written concisely as

$$\chi_i = \min_{\mathbf{e}} \left([\boldsymbol{\Delta} - \mathsf{R}\mathbf{e}]^2 \right) \tag{2.24}$$

Here we have introduced a block matrix R whose elements are given by

$$\mathsf{R}_{n\mu,\nu\nu'} = \delta_{\mu\nu} R^{\nu'}_{j_n\gamma_n,i\alpha_n}$$

and the entries of the vector $\mathsf{R}\mathbf{e}$ are given by $\sum_{\nu\nu'} \mathsf{R}_{n\mu,\nu\nu'} e_{\nu\nu'}$ in the obvious way. Once Eq. (2.24) is minimized, we obtain the residual contribution from non-affine deformation and the “best-fit” affine strain. These can be expressed as

$$\chi_i = \boldsymbol{\Delta}^{\mathrm{T}} \mathsf{P} \boldsymbol{\Delta} \tag{2.25}$$

$$\mathbf{e} = \mathsf{Q} \boldsymbol{\Delta}. \tag{2.26}$$

with the matrices $\mathsf{P} = \mathsf{I} - \mathsf{R}\mathsf{Q}$ and $\mathsf{Q} = \left(\mathsf{R}^{\mathrm{T}} \mathsf{R} \right)^{-1} \mathsf{R}^{\mathrm{T}}$. Note that P is a projection matrix ($\mathsf{P}^2 = \mathsf{P}$), which, when acting on the space of $\boldsymbol{\Delta}$, extracts only the non-affine component of the displacements. It can be seen that P has d^2 zero and $N_\Omega d - d^2$ non-zero eigenvalues corresponding to the affine and non-affine subspaces respectively. As usual $\mathsf{I} - \mathsf{P}$ will then project out the affine component of $\boldsymbol{\Delta}$. The elements of the best-fit affine transformation matrix $\mathcal{D}$ from Eq. (2.26) can be written explicitly as

$$\mathcal{D}_{\mu\nu} = \sum_{\nu'} (\mathbf{M}^{-1})_{\nu\nu'} \sum_{n} R^{\nu'}_{j_n\gamma_n,i\alpha_n} \Delta_{n\mu} \tag{2.27}$$

in terms of the matrix M with elements

$$M_{\nu\nu'} = \sum_{n} R^{\nu}_{j_n\gamma_n,i\alpha_n} R^{\nu'}_{j_n\gamma_n,i\alpha_n}.$$

For the lattices considered in this paper, M is diagonal due to lattice symmetries (see also the discussion in Ref. [5]) so that Eq.(2.27) simplifies to

$$\mathcal{D}_{\mu\nu} = \frac{1}{\sum_n (R^{\nu}_{j_n\gamma_n,i\alpha_n})^2} \sum_n R^{\nu}_{j_n\gamma_n,i\alpha_n} \Delta_{n\mu} \tag{2.28}$$

Due to translational invariance, the properties of χ_i are the same for all lattice sites i, for any lattice and dimension. We therefore abbreviate χ_i simply as χ in the following.

We now obtain the statistics of $(\chi, \mathbf{e})$ in the classical canonical ensemble for any lattice and dimension. For any given Hamiltonian $\mathcal{H}$ the canonical probability distribution is

$$\mathbb{P}(\mathbf{p}, \mathbf{u}) = \frac{1}{Z} e^{-\beta \mathcal{H}(\mathbf{p},\mathbf{u})} \tag{2.29}$$

Here we restrict the Hamiltonian to the *harmonic approximation*,

$$\mathcal{H} = \sum_{i\alpha} \frac{\mathbf{p}^2_{i\alpha}}{2m_{i\alpha}} + \frac{1}{2} \sum_{i\alpha,j\gamma} \sum_{\mu\nu} u^{\mu}_{i\alpha} \phi^{\mu\nu}_{i\alpha,j\gamma} u^{\nu}_{j\gamma} \tag{2.30}$$

where $\mathbf{p}_{i\alpha}$ are the momenta, $m_{i\alpha}$ the masses and $\phi^{\mu\nu}_{i\alpha,j\gamma}$ are the elements of the Hessian. The Hamiltonian can be easily diagonalized if one takes a plane wave ansatz for the displacements. We therefore write

$$\mathbf{u}_{i\alpha} = \int \frac{d\mathbf{q}}{V_{BZ}} \mathbf{u}_{\alpha}(\mathbf{q}) e^{i\mathbf{q}\cdot\mathbf{R}_{i\alpha}}$$

and similarly

$$\mathbf{u}_{i\alpha,j\gamma} = \int \frac{d\mathbf{q}}{V_{BZ}} \mathbf{u}_{\alpha}(\mathbf{q}) \left(e^{i\mathbf{q}\cdot\mathbf{R}_{i\alpha}} - e^{i\mathbf{q}\cdot\mathbf{R}_{j\gamma}} \right)$$

where the integration runs over the first Brillouin zone with volume given by $V_{BZ} = \sum_{\mathbf{R}_{i0}} \int d\mathbf{q} \exp(i\mathbf{q}\cdot\mathbf{R}_{i0})$ and $\mathbf{q}$ is the wave vector. The Lattice Green's Function (LGF) may be obtained as the inverse $\mathbf{G}(\mathbf{q}) = \mathbf{D}^{-1}(\mathbf{q})$ of the dynamical matrix $\mathbf{D}(\mathbf{q})$ with elements

$$D^{\mu\nu}_{\alpha\gamma}(\mathbf{q}) = \sum_i \phi^{\mu\nu}_{i\alpha,0\gamma} e^{i\mathbf{q}\cdot(\mathbf{R}_{i\alpha} - \mathbf{R}_{0\gamma})} \tag{2.31}$$

With the knowledge of the LGF, thermal averages of different quantities are easy to calculate. For example the displacement correlator reads in Fourier space

$$\left\langle u^{\mu}_{\alpha}(\mathbf{q}) u^{\nu}_{\gamma}(\mathbf{q}') \right\rangle = G^{\mu\nu}_{\alpha\gamma}(\mathbf{q}) \delta(\mathbf{q} + \mathbf{q}') V_{BZ},$$

and in real space

$$\left\langle u^{\mu}_{i\alpha} u^{\nu}_{j\gamma} \right\rangle = \frac{1}{\beta} \int \frac{d\mathbf{q}}{V_{BZ}} G^{\mu\nu}_{\alpha\gamma}(\mathbf{q}) e^{i\mathbf{q}\cdot(\mathbf{R}_{i\alpha} - \mathbf{R}_{j\gamma})}. \tag{2.32}$$

Along similar lines, for our coarse-graining volume one can obtain the thermal average of any observable $A(\boldsymbol{\Delta})$ as

$$\langle A(\boldsymbol{\Delta})\rangle = \frac{1}{\mathcal{Z}}\int d\boldsymbol{\Delta}\, A(\boldsymbol{\Delta})e^{-\frac{1}{2}\boldsymbol{\Delta}^{\mathrm{T}}\mathsf{C}^{-1}\boldsymbol{\Delta}} \tag{2.33}$$

with the normalisation constant $\mathcal{Z} = (2\pi)^{N_\Omega d/2}\sqrt{|\,\mathsf{C}\,|}$. The covariance matrix C in the above equation can be obtained from the LGF via

$$\begin{aligned}
\mathsf{C}_{n\mu,m\nu} &= \langle \Delta_{n\mu}\Delta_{m\nu}\rangle \\
&= \int \frac{d\mathbf{q}}{\beta V_{BZ}}\Big[G^{\mu\nu}_{\gamma_n\gamma_m}(\mathbf{q})e^{i\mathbf{q}\cdot\mathbf{R}_{j_n\gamma_n,j_m\gamma_m}} \\
&\quad - G^{\mu\nu}_{\alpha_n\gamma_m}(\mathbf{q})e^{i\mathbf{q}\cdot\mathbf{R}_{i\alpha_n,j_m\gamma_m}} \\
&\quad - G^{\mu\nu}_{\gamma_n\alpha_m}(\mathbf{q})e^{i\mathbf{q}\cdot\mathbf{R}_{j_n\gamma_n,i\alpha_m}} \\
&\quad + G^{\mu\nu}_{\alpha_n\alpha_m}(\mathbf{q})e^{i\mathbf{q}\cdot\mathbf{R}_{i\alpha_n,i\alpha_m}}\Big]
\end{aligned} \tag{2.34}$$

To obtain the statistics of $(\chi, \mathbf{e})$ we make use of Eq. (2.33) and obtain the characteristic function $\Phi\,(\mathrm{k}, \boldsymbol{\kappa})$ for the joint probability distribution $\mathbb{P}(\chi, \mathbf{e})$.

$$\begin{aligned}
\Phi\,(\mathrm{k}, \boldsymbol{\kappa}) &= \exp\left(-\frac{1}{2}\boldsymbol{\kappa}^{\mathrm{T}}\mathsf{QC}\left(\mathsf{I} - 2i\mathrm{k}\mathsf{PC}\right)^{-1}\mathsf{Q}^{\mathrm{T}}\boldsymbol{\kappa}\right) \\
&\quad \times \frac{1}{\sqrt{|\,\mathsf{I} - 2i\mathrm{k}\mathsf{PCP}\,|}}.
\end{aligned} \tag{2.35}$$

Using the identity

$$\left(\mathsf{I} - 2i\mathrm{k}\mathsf{PC}\right)^{-1} = \mathsf{I} + \left(\mathsf{I} - 2i\mathrm{k}\mathsf{PC}\right)^{-1}\left(2i\mathrm{k}\mathsf{PC}\right)$$

the last result can be written in terms of the characteristic function for the marginals as follows:

$$\Phi\,(\mathrm{k}, \boldsymbol{\kappa}) = \mathit{\Phi}_\chi(\mathrm{k})\,\mathit{\Phi}_{\mathbf{e}}(\boldsymbol{\kappa})\mathrm{e}^{-i\mathrm{k}\boldsymbol{\kappa}^{\mathrm{T}}\mathsf{QC}(\mathsf{I}-2i\mathrm{k}\mathsf{PC})^{-1}\mathsf{PCQ}^{\mathrm{T}}\boldsymbol{\kappa}} \tag{2.36}$$

where

$$\mathit{\Phi}_\chi(\mathrm{k}) = \frac{1}{\prod_l \sqrt{1 - 2i\mathrm{k}\sigma_l}} \tag{2.37}$$

$$\mathit{\Phi}_{\mathbf{e}}(\boldsymbol{\kappa}) = e^{-\frac{1}{2}\boldsymbol{\kappa}^{\mathrm{T}}\mathsf{QCQ}^{\mathrm{T}}\boldsymbol{\kappa}} \tag{2.38}$$

and the σ_l are the eigenvalues of PCP. For $\boldsymbol{\kappa} = 0$ and $\mathrm{k} = 0$, $\Phi\,(\mathrm{k}, \boldsymbol{\kappa})$ reduces to $\mathit{\Phi}_\chi(\mathrm{k})$ and $\mathit{\Phi}_{\mathbf{e}}(\boldsymbol{\kappa})$ respectively. The term in the exponential governs the (non-linear) coupling between the non-affine and affine components of the displacements. Previous work has shown that this coupling is significant only for large uniaxial and shear strains [5]. For smaller strains, it can largely be ignored.

With the knowledge of the characteristic function, thermal averages and other higher order moments may be computed such as

$$\langle\chi\rangle = \mathrm{Tr}\left(\mathsf{PCP}\right) \tag{2.39}$$

$$\left\langle \mathbf{e}\mathbf{e}^{\mathrm{T}} \right\rangle = \mathsf{QCQ}^{\mathrm{T}} \tag{2.40}$$

From Eq. (2.39) it is clear that $\langle\chi\rangle$ is a sum over the eigenvalues of (PCP). Each eigenvalue represents the contribution of a specific *non-affine mode* to χ. It has been shown [6] that these eigenvalues are elements of the inverse Hessian of the free energy in the direction of the non-affine mode in configuration space. A large eigenvalue implies a small value of the local curvature of the free energy minimum. We shall see later in this paper that the corresponding *eigenvectors* are precisely those atomic displacement fluctuations that lead to lattice defects or other imperfections tending to destroy crystalline order. The non-affine mode corresponding to the largest eigenvalue therefore has the highest contribution to this process.

The non-affine parameter χ depends linearly on temperature T (at low T, where a harmonic theory applies) and is inversely proportional to the strength of the interaction. Due to the fact that the underlying distribution of $\mathbf{\Delta}$ is Gaussian, $\langle\mathbf{e}\rangle$ vanishes unless an external stress is present. Finally, the leading order non-linear coupling between non-affine and affine modes is given by

$$\left\langle \chi\mathbf{e}\mathbf{e}^{\mathrm{T}} \right\rangle - \langle\chi\rangle\left\langle \mathbf{e}\mathbf{e}^{\mathrm{T}} \right\rangle = 2\mathsf{QC}[\mathsf{P},\mathsf{C}]\mathsf{Q}^{\mathrm{T}}. \tag{2.41}$$

Two-point distributions and spatial correlation functions for χ and e may also be calculated following the procedure explained in Refs. [5–7]. Below we include a brief description for completeness.

2.3.1 Spatial direct- and cross- correlations

The spatial correlations of the non-affine parameter at two lattice sites i and k are given by ($\chi \equiv \chi_i$, $\bar{\chi} \equiv \chi_k$)

$$\langle\chi\bar{\chi}\rangle - \langle\chi\rangle\langle\bar{\chi}\rangle = 2\mathsf{Tr}(\mathsf{P}\bar{\mathsf{C}}\mathsf{P})(\mathsf{P}\bar{\mathsf{C}}\mathsf{P})^{\mathsf{T}} \tag{2.42}$$

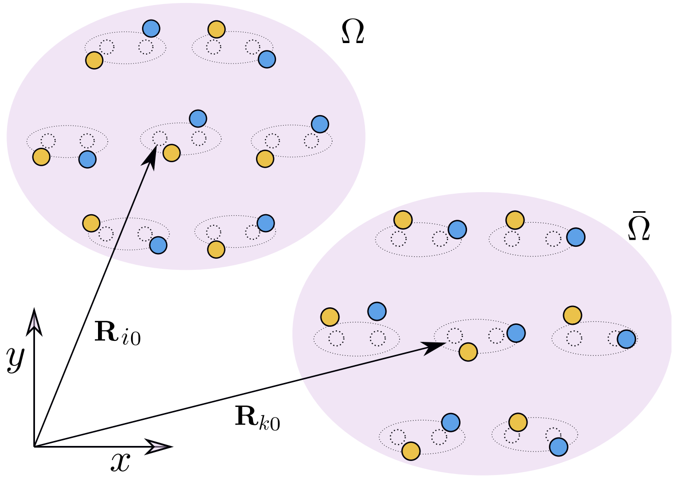

Fig. 2.6. Schematic showing two coarse-graining volume for cross correlations. Two distant neighborhoods Ω and $\bar{\Omega}$ are situated around lattice sites i and k respectively.

The two point covariance $\bar{\mathsf{C}}$ between relative displacements within two coarse-graining neighborhoods $\Omega \equiv \Omega(i)$ and $\bar{\Omega} \equiv \Omega(k)$ around lattice positions $\mathbf{R}_{i0}$ and $\mathbf{R}_{k0}$, respectively, is defined as

$$\bar{\mathsf{C}}_{n\mu,m\nu} = \langle \Delta_{n\mu} \bar{\Delta}_{m\nu} \rangle \tag{2.43}$$

It is obtained from an expression similar to Eq. (2.34) (see Ref. [5] for details):

$$\begin{aligned} \bar{\mathsf{C}}_{n\mu,m\nu} \quad = \quad & \int \frac{d\mathbf{q}}{\beta V_{BZ}} \Big[G^{\mu\nu}_{\gamma_n\gamma_m}(\mathbf{q}) e^{i\mathbf{q}\cdot\mathbf{R}_{j_n\gamma_n,l_m\gamma_m}} \\ & - G^{\mu\nu}_{\alpha_n\gamma_m}(\mathbf{q}) e^{i\mathbf{q}\cdot\mathbf{R}_{i\alpha_n,l_m\gamma_m}} \\ & - G^{\mu\nu}_{\gamma_n\alpha_m}(\mathbf{q}) e^{i\mathbf{q}\cdot\mathbf{R}_{j_n\gamma_n,k\alpha_m}} \\ & + G^{\mu\nu}_{\alpha_n\alpha_m}(\mathbf{q}) e^{i\mathbf{q}\cdot\mathbf{R}_{i\alpha_n,k\alpha_m}} \Big] \end{aligned} \tag{2.44}$$

where we have assumed that the elements of $\Omega(k)$ are numbered $(l_m\gamma_m, k\alpha_m)$. For all simple lattices in $2d$ and $3d$ with one particle basis, the correlations $\langle \chi\bar{\chi} \rangle - \langle \chi \rangle \langle \bar{\chi} \rangle$ are short ranged.

Strain-strain correlation may be obtained from

$$\left\langle \mathbf{e}\bar{\mathbf{e}}^{\mathrm{T}} \right\rangle = \left\langle \mathsf{Q}\boldsymbol{\Delta}\bar{\boldsymbol{\Delta}}^{\mathrm{T}}\mathsf{Q}^{\mathrm{T}} \right\rangle = \mathsf{Q}\bar{\mathsf{C}}\mathsf{Q}^{\mathrm{T}}. \tag{2.45}$$

It is often useful to consider these correlations in Fourier space, where they can be expressed as [5]

$$\left\langle \mathbf{e}\bar{\mathbf{e}}^{\mathrm{T}} \right\rangle(\mathbf{q}) = \mathsf{Q}\bar{\mathsf{C}}(\mathbf{q})\mathsf{Q}^{\mathrm{T}} \tag{2.46}$$

with the Fourier transform $\bar{\mathsf{C}}(\mathbf{q})$ defined via

$$\bar{\mathsf{C}}_{n\mu,m\nu} = \int \frac{d\mathbf{q}}{V_{BZ}} \bar{\mathsf{C}}_{n\mu,m\nu}(\mathbf{q}) e^{i\mathbf{q}\cdot\mathbf{R}_{i0,k0}}.$$

Comparison with Eq.(2.44) then shows that $\beta\bar{\mathsf{C}}_{n\mu,m\nu}(\mathbf{q})$ is given directly by the term in square brackets in Eq.(2.34). This follows from the fact that the particle pairs in $\Omega(k)$ are just those in $\Omega(i)$ translated by $\mathbf{R}_{k0,i0}$; e.g. in the first term of Eq.(2.44) one has after extracting the Fourier factor $e^{i\mathbf{q}\cdot\mathbf{R}_{i0,k0}}$ the phase term

$$\begin{aligned} e^{i\mathbf{q}\cdot(\mathbf{R}_{jn\gamma n,lm\gamma m}-\mathbf{R}_{i0,k0})} &= e^{i\mathbf{q}\cdot[\mathbf{R}_{jn\gamma n}-(\mathbf{R}_{lm\gamma m}-\mathbf{R}_{k0,i0})]} \\ &= e^{i\mathbf{q}\cdot(\mathbf{R}_{jn\gamma n}-\mathbf{R}_{jm\gamma m})} \\ &= e^{i\mathbf{q}\cdot\mathbf{R}_{jn\gamma n,jm\gamma m}} \end{aligned}$$

Correlations of the affine displacements viz. local volume change (e_v), uniaxial or deviatoric strain (e_u), shear strain (e_s) and rotation (w) respectively, may be obtained using the component forms as follow,

$$\begin{aligned} \left\langle e_v^2 \right\rangle(\mathbf{q}) &= E_{1111} + E_{2222} + 2E_{1122} \\ \left\langle e_u^2 \right\rangle(\mathbf{q}) &= E_{1111} + E_{2222} - 2E_{1122} \\ \left\langle e_s^2 \right\rangle(\mathbf{q}) &= E_{1212} + E_{2121} + 2E_{1221} \\ \left\langle w^2 \right\rangle(\mathbf{q}) &= E_{1212} + E_{2121} - 2E_{1221}, \end{aligned} \tag{2.47}$$

Here we have used the same notation for the fourth rank tensor, $\mathsf{E} = \mathsf{Q}\bar{\mathsf{C}}(\mathbf{q})\mathsf{Q}^{\mathrm{T}}$ as in Ref. [5], and $\langle e_v^2 \rangle(\mathbf{q})$ etc. are strain correlators in Fourier space. Expressions for 3d can be obtained in similar fashion, for instance, strain correlation in 3d for volume, uniaxial and shear in the $x-y$ plane are as follows,

$$\begin{aligned} \left\langle e_v^2 \right\rangle(\mathbf{q}) &= E_{1111} + E_{2222} + E_{3333} + 2\left(E_{1122} + E_{1133} + E_{2233}\right) \\ \left\langle e_u^2 \right\rangle(\mathbf{q}) &= E_{1111} + E_{2222} + E_{3333} - 2\left(E_{1122} + E_{1133} - E_{2233}\right) \\ \left\langle e_s^2 \right\rangle(\mathbf{q}) &= E_{1212} + E_{2121} + 2E_{1221}. \end{aligned} \tag{2.48}$$

Other components of the shear strain (and rotation) can be written down by analogy. As before (see Sec. 2.2.1), the $\mathbf{q} \to 0$ limit of the correlation function obtains the elastic compliances or moduli of the lattice.

2.4 Summary and conclusion

In this chapter we have introduced and described the projection formalism for decomposing particle displacements from a reference configuration into affine and non-affine components. While the affine components of the displacements preserve local connectivity, the non-affine component tend to disrupt them. We show later in this thesis how one can selectively enhance or suppress the non-affine component without affecting the affine part. Since our formulation is based on the existence of tagged reference, it does suffer from one fault, namely, exchange of particle tags even in the reference structure is classified as non-affine “displacement”. Thereby explicitly breaking the permutation symmetry of particle tags. This issue however does not affect any of the conclusion of this thesis since particles cannot normally exchange positions without any prior displacements.

In the next chapter, we use this knowledge to analyse displacements in a few chosen crystal lattices in two and three dimensions.

3

Non-affine displacements in $2d$ and $3d$ crystals

In this chapter, we use the methods of Chapter 2 to obtain statistics of affine and non-affine displacements for a number of lattices in two (2d) and three (3d) dimensions. In 2d we consider lattices both with a single atom basis such as the triangular and square lattices as well as those with a multi-atom basis like the planar honeycomb and the Kagome lattices. In 3d we confine ourselves to a study of cubic systems, namely, the simple cubic, body centered and face centered cubic lattices. In order to keep the discussion general we model the interactions by harmonic springs. Our results are therefore valid for any crystalline solid at sufficiently low temperatures where anharmonic effects may be neglected.

3.1 Model Hamiltonian

A typical Hamiltonian for a set of atoms interacting among themselves by harmonic springs is given by,

$$\mathcal{H} = \sum_{i\alpha} \frac{\mathbf{p}_{i\alpha}^2}{2m} + \sum_{\langle i\alpha, j\gamma\rangle} \frac{k_{i\alpha,j\gamma}}{2} \left(\mathbf{u}_{i\alpha,j\gamma} \cdot \hat{\mathbf{R}}_{i\alpha,j\gamma}\right)^2 \tag{3.1}$$

Here $k_{i\alpha,j\gamma}$ determines the spring constant acting between particle pairs $i\alpha, j\gamma$. The $k_{i\alpha,j\gamma}$ are chosen such that the lattice is stable and satisfies Maxwell's stability criteria [76]. In particular, we take $k_{i\alpha,j\gamma}$ to be equal to k_1 for nearest neighbors and k_2 for next nearest neighbors; interactions beyond the second neighbor shell are neglected. Additionally, throughout the paper, the nearest neighbor bond strength k_1 and the lattice constant a are chosen to be unity without any loss of generality. This sets the scales for energy and length respectively.

We have also, in some cases, studied the effect of including simple three body bond-angle dependent potentials in order to introduce an energy cost for bond bending.

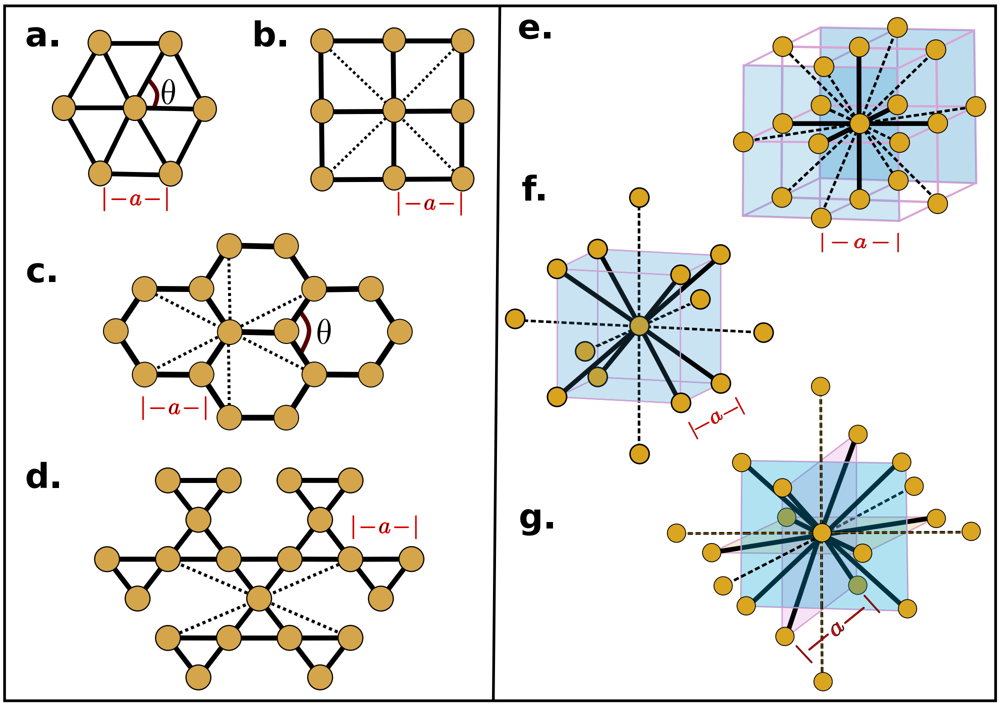

Fig. 3.1. Schematic diagram showing the triangular **a.**, square **b.**, planar honeycomb **c.**, kagome **d.**, simple cubic **e.**, body centered cubic **f.** and face centered cubic **g.** lattices. The nearest neighbor bonds are shown in bold while the next nearest neighbor bonds, whenever present, are drawn using dashed lines. The parameter a is the lattice constant, chosen to be unity. The equilibrium bond angle θ_0 has also been marked for the triangular and honeycomb lattices. In the 3d cases shaded color regions have been added to make the cubic geometry clearer.

These interactions are very well documented in the literature mostly on the system like graphene [77, 78]. To model bond bending we take the Kirkwood [79] model,

$$\mathcal{H}_{bend} = \frac{k_b}{2} \sum_{\langle i\alpha, j\gamma, k\delta \rangle} \left(\Delta\theta_{i\alpha,j\gamma,k\delta}\right)^2 .$$

which in the small oscillation approximation can be written as

$$\begin{aligned} \mathcal{H}_{bend} \quad & \simeq \tfrac{k_b}{2} \textstyle\sum_{\langle i\alpha,j\gamma,k\delta\rangle} [\cot\theta_0 (\hat{\mathbf{R}}_{j\gamma,k\delta} \cdot \mathbf{u}_{j\gamma,k\delta} \\ & + \hat{\mathbf{R}}_{i\alpha,k\delta} \cdot \mathbf{u}_{i\alpha,k\delta}) - \tfrac{1}{\sin\theta_0} (\hat{\mathbf{R}}_{i\alpha,k\delta} \cdot \mathbf{u}_{j\gamma,k\delta} \\ & + \hat{\mathbf{R}}_{j\gamma,k\delta} \cdot \mathbf{u}_{i\alpha,k\delta})]^2 \end{aligned} \qquad (3.2)$$

where θ_0 is the equilibrium angle and angular brackets denote triples of particles where $i\alpha$ and $j\gamma$ are both nearest neighbors of $k\delta$.

In the following section we discuss our results for specific lattices in 2d and 3d. In Fig. 3.1 we have shown these lattices schematically and indicated the bonding interactions that we have considered.

We are now in a position to use the methods described in Chapter 2 to obtain the statistics of coarse grained non-affine and affine displacements of particles interacting through the Hamiltonians presented in Sec. 3.1 for a collection of 2d and 3d lattices (see Fig. 3.1). As discussed above, the statistics of χ can be obtained once one has knowledge of the matrix PCP. The projection matrix P only depends upon the reference position of particles in the lattice and can be constructed easily. The covariance matrix C can be calculated using Eq. (2.34) once one knows the dynamical matrix $D(\mathbf{q})$. For the harmonic interactions with nearest (and next nearest) neighbors we can compute $D(\mathbf{q})$ in a straightforward manner for all lattices; the results are listed in Appendix A.1. The probability distribution for χ can then be obtained using the eigenvalues of PCP. We have also checked our results by directly simulating the model systems using standard molecular dynamics in the canonical ensemble [48] as implemented in the LAMMPS simulation package [50]. All our results scale linearly with temperature $k_BT = \beta^{-1}$, where k_B is the Boltzmann constant. We have used different temperatures for different lattices only for ease of presentation. Our results for $P(\chi)$

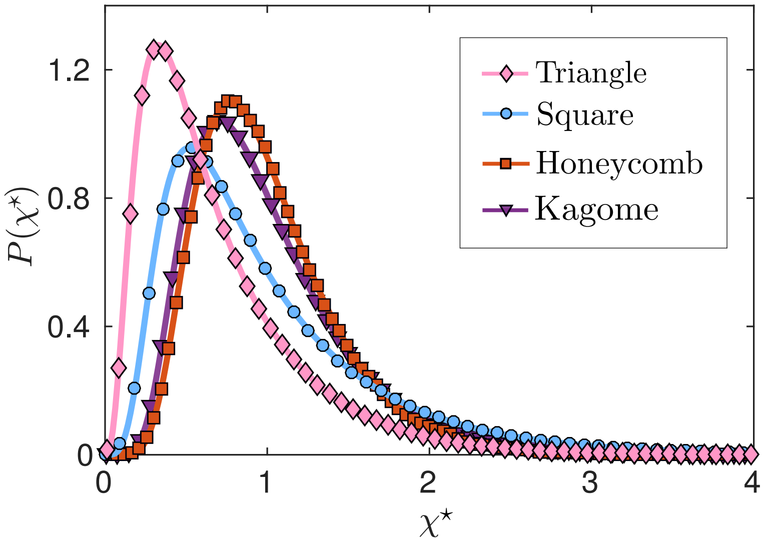

Fig. 3.2. Scaled distribution $P(\chi^\star)$ for all 2d lattices where $\chi^\star = \chi/\langle\chi\rangle$. The solid colored lines are from our analytic calculations and the points are simulation results (using $N = 1024$ except for Honeycomb, where $N = 512$ and Kagome, where $N = 300$). Triangular: light pink with $k_b = 0$; Square: sky blue, $k_2 = 0.5$; Honeycomb: brown, $k_2 = 0.5$ and Kagome: purple, $k_2 = 0.5$. The distribution for square and triangle plotted here is for the smallest coarse-graining volume used in Sections 3.1.1 and 3.1.2. Whereas, for other lattices coarse-graining volume is same as shown in Fig 3.6 and 3.8.

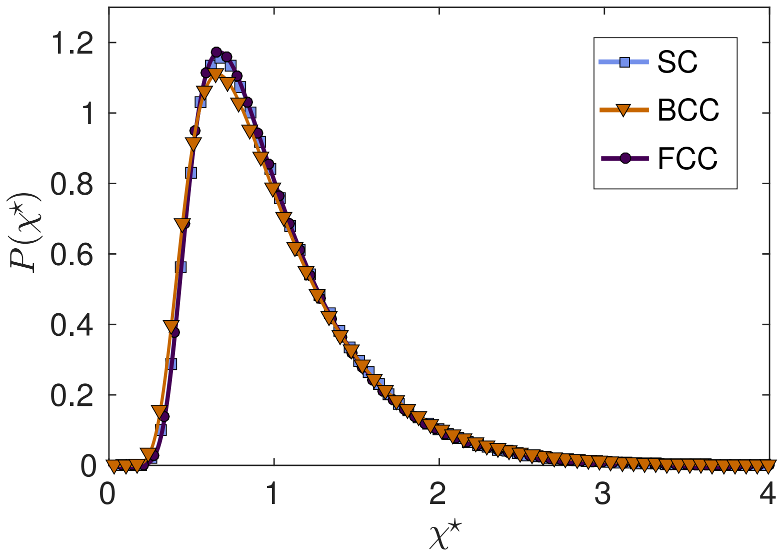

Fig. 3.3. Scaled distribution $P(\chi^\star)$ for all 3d lattices, where $\chi^\star = \chi/\langle\chi\rangle$. The meaning of the symbols is the same as in Fig. 3.2. The distribution is plotted for SC: sky blue, $k_2 = 0.5$, $N = 1000$. BCC : brown, $k_2 = 0.5$, $N = 2000$. FCC: purple, $k_2 = 0.75$, $N = 4000$. The coarse-graining volume is described in the text.

obtained by numerically inverting $\Phi_\chi(k)$ are shown in Fig. 3.2 and Fig. 3.3 together with the results from direct simulations. All the averaging is done over at least 1000 well equilibrated and uncorrelated configurations. Needless to say, the agreement is perfect as expected.

Once our formalism is thus established for all the systems considered in 2d and 3d, we turn to each lattice in detail below. We show that using our method one can find the most prominent non-affine displacement modes (eigenvectors of PCP) for any lattice. Often these modes turn out to be precursors for the most commonly observed defect structures for a given lattice system. We note that the relative probabilities of different non-affine modes also depend on the lattice and the interactions and can be easily captured using our approach.

3.1.1 The triangular lattice in $2d$

The triangular lattice is the only close packed structure observed in 2d [1]. It has just one basis particle per site. We have previously established that the most prominent non-affine mode, i.e. the eigenvector corresponding to the largest eigenvalue of PCP, corresponds to the incipient dissociation of a tightly packed dislocation-anti-dislocation pair [6]. To reach this conclusion we used a coarse-graining volume that included only six nearest neighbor particles (see Fig. 3.4). This makes PCP a 12×12 matrix

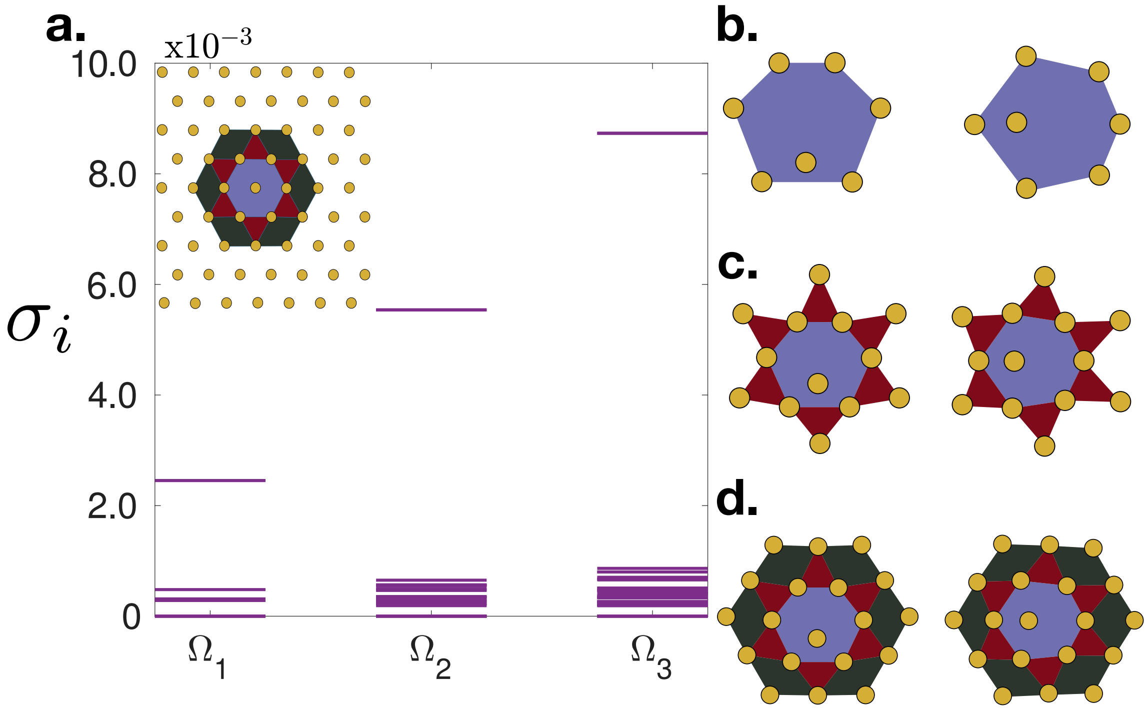

Fig. 3.4. Non-affine modes for triangular lattice with different sizes of the coarse graining volume Ω at inverse temperature $\beta = 1000$ with no next nearest neighbor bonds. **a.** The spectrum of the eigenvalues of PCP is shown for three different choices of Ω (inset), which consists of all particles within the first (Ω_1 - light blue), second (Ω_2 - magenta) and third (Ω_3 - dark green) nearest neighbor shells. The reference positions of particles are shown by small yellow circles. The horizontal lines show the eigenvalues. Note the large gap between the largest eigenvalue and the rest of the spectrum. **b.** The two degenerate eigenvectors corresponding to the largest eigenvalue of PCP. Note that a nearest neighbor bond is being stretched and a next near neighbor bond nearly perpendicular to it has been shortened. This mode is same as the one discussed in Ref. [6]. This displacement tends to replace the six-fold neighborhoods by two five- and two seven-fold neighbors producing a tightly bound dislocation–antidislocation pair. **c.** and **d.** show that increasing Ω does not affect the nature of this mode.

with 4 zero eigenvalues. The non-zero eigenvalues correspond to the independently fluctuating non-affine modes. We have now extended this calculation to include larger Ω. Our results are shown in Fig. 3.4. We recover the two degenerate, non-affine modes with the largest eigenvalue described in [6]. We see that these modes continue to be present if one increases the size of the coarse-graining volume $\Omega_1 < \Omega_2 < \Omega_3$. At the same time the gap between the first eigenvalue and the others increases significantly.

It is interesting that as the size of Ω increases, additional vibrational modes go on to populate the lower eigenvalues, keeping the gap intact. We show later in this chapter that this phenomenon is quite general and observed for many (but not all) lattices. We will comment further on this observation in the discussion (Section 4.5).

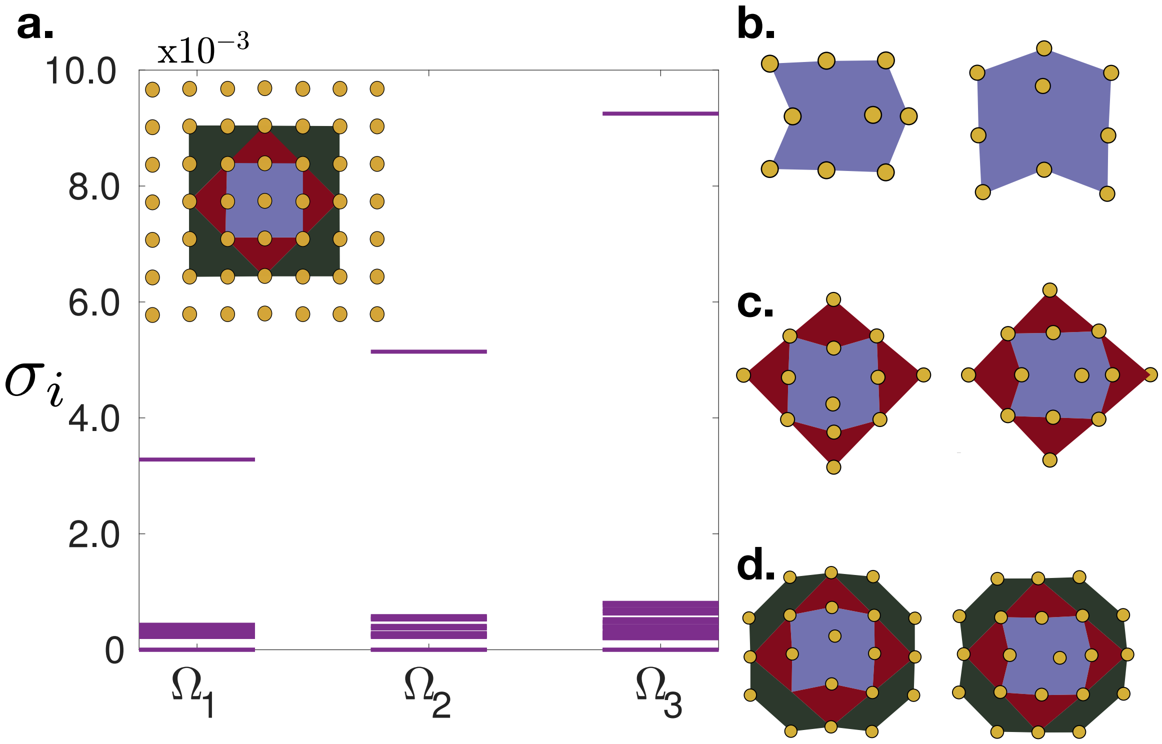

Fig. 3.5. Non-affine modes for square lattice with different sizes of the coarse graining volume Ω. The parameters are $k_2 = 0.5$, $\beta = 1000$. **a.** The spectrum of the eigenvalues of PCP is shown for three different choices of Ω (inset). The color code is the same as in Fig. 3.4**b** The two degenerate eigenvectors corresponding to the largest eigenvalue of PCP. These modes tend to shift a row of atoms relative to adjacent rows **c.** and **d.** show that, as in the triangular case, increasing Ω does not affect the nature of these modes.

3.1.2 The square lattice in $2d$

For the square lattice, we need to include both nearest and next nearest neighbor bonds in order to satisfy the Maxwell criterion for stability [76], viz. for free boundary conditions, a stiff frame consisting of p points in d dimensions should at least have $c = pd - d(d+1)/2$ connections among the points. We have also chosen the smallest Ω such that all particles to which the central particle is bonded by nonzero interactions are included. This yields an Ω containing four neighbor and four next neighbor particles. Hence, one obtains PCP as a 16×16 matrix. This has 16 eigenvalues with eight non-zero values. As the size of Ω and with it the degree of coarse-graining, is increased one then observes the same effect on the square lattice as in the triangular lattice (see Fig. 3.5). Again there is a gap in the eigenvalue spectra between the largest eigenvalue and the rest; this gap increases with the coarse-graining scale chosen. Fig 3.5 shows, in addition to the coarse-graining volumes and the eigenvalue spectra, the softest degenerate eigenmodes. The nature of the mode corresponding to the largest eigenvalue is somewhat different to the triangular lattice case. Instead of introducing defects, it tends to shift the middle row of atoms with respect to its neighboring rows in a direction parallel to the rows. One can easily see that this corresponds to a precursor that can take a square lattice to a triangular one by a shuffle of alternate layers [35]. We now consider more complex lattices in $2d$ such as honeycomb and kagome.

3.1.3 The planar honeycomb lattice in $2d$

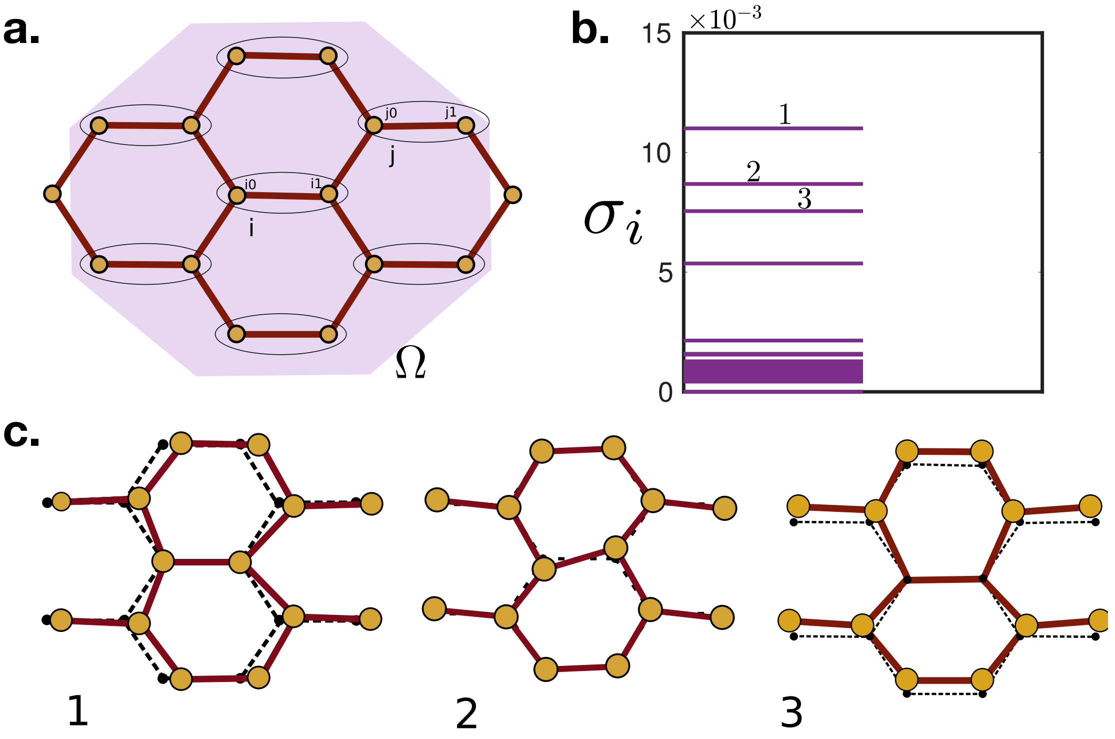

Fig. 3.6. Non-affine modes and spectra for the planar honeycomb, with $k_2 = 0.5$ and $\beta = 500$. **a.** Schematic of the lattice and the coarse graining volume (pink shaded region) used, with ellipses drawn around each pair of atoms that is in the same basis. **b.** The eigenvalue spectrum. Note that there is no single prominent eigenmode with a large gap as in the triangular and square structures. **c.** Plots of the first three non-degenerate non-affine eigenmodes in the order of prominence (magnitude of eigenvalue). Eigenmode 2 represents an incipient Stone-Wales defect.

The planar honeycomb (or simply honeycomb!) lattice occurs in many condensed matter systems, the most noteworthy being graphene [77]. A honeycomb lattice is essentially a triangular lattice with a two particle basis. As shown in Fig 3.6, a cell (ellipse) indexed i has two particles labeled $\alpha \in \{0, 1\}$. Each basis particle has three neighbors and six next nearest neighbors. The coarse-graining volume for a honeycomb lattice Fig. 3.6, is constructed as mentioned in Section 2.3 with $\mathfrak{r}$ the next nearest neighbor distance, i.e. $\sqrt{3}a$. Thus, Ω consists of a total of 17 pairs of particles. (The two particles in the basis each have 3 nearest neighbors and 6 next nearest neighbors, giving 18 particle pairs; excluding from this the double-counted pair of basis atoms yields 17 pairs.) As per the prescription, P can be constructed and will be a 34×34 dimensional matrix. The dynamical matrix is a 4×4 matrix with two eigenvalues corresponding to the acoustic branches and the other two to the optical ones. These eigenvalues and eigenvectors of the dynamical matrix are used to calculate the covariance matrix C as shown in Eq. (2.34). Our experience by numerical study of the triangular and square lattices shows that increasing the size of Ω does not influence the nature of the most prominent non-affine modes, although it does considerably increase computational complexity.

The planar honeycomb structure has been studied in detail in an earlier publication [7]. We include here some of those results for completeness. The probability distribution of χ is shown in Fig. 3.2 together with the results of other lattices. Fig. 3.6 shows the non-affine eigenvalue spectra. We observe that, in contrast to the triangular and square lattice, there is no clear gap between the largest eigenvalue and the others. We suspect that the presence of optical modes produces an eigenvalue spectrum that does not have pronounced gaps between different modes. It has also been shown in [7] that the nature of this spectrum remains unaffected if one softens the lattices by reducing the value of spring constant k_2. In fact, as one softens the lattice these eigenvalues grow without bound, producing more non-affinity in the system. This is obvious because C is proportional to the lattice Green's function which itself diverges when the spring constant vanishes.

Eigenvectors of PCP corresponding to the first three largest eigenvalues are plotted in Fig. 3.6. Intriguingly, the second mode represents the precursor to a Stone-Wales (SW) defect [80]. In SW a central bond flips by $90°$ creating pentagonal and heptagonal voids. One of the questions that was not addressed in [7] was what, if any, is the effect of introducing a bending rigidity [79, 81] to the bonds? We take up this issue below.

Bond bending rigidity may be modeled as a three body potential given by Eq.(3.2). The dynamical matrix corresponding to bond bending can be obtained in closed form (see Appendix A.1). The total dynamical matrix, which is the sum of the dynamical matrices for bond stretching and bending, is used to calculate C.

Fig. 3.7 shows how the spectrum of non-affine (non-zero) eigenvalues of PCP changes upon increasing the bending constant k_b. We have included a similar calculation for the triangular lattice for comparison. Because the triangular lattice is isotropic, addition of a bond bending cost only stiffens the lattice and decreases the eigenvalues and consequently their sum, χ. We see that 5-7 defect precursor modes as discussed above

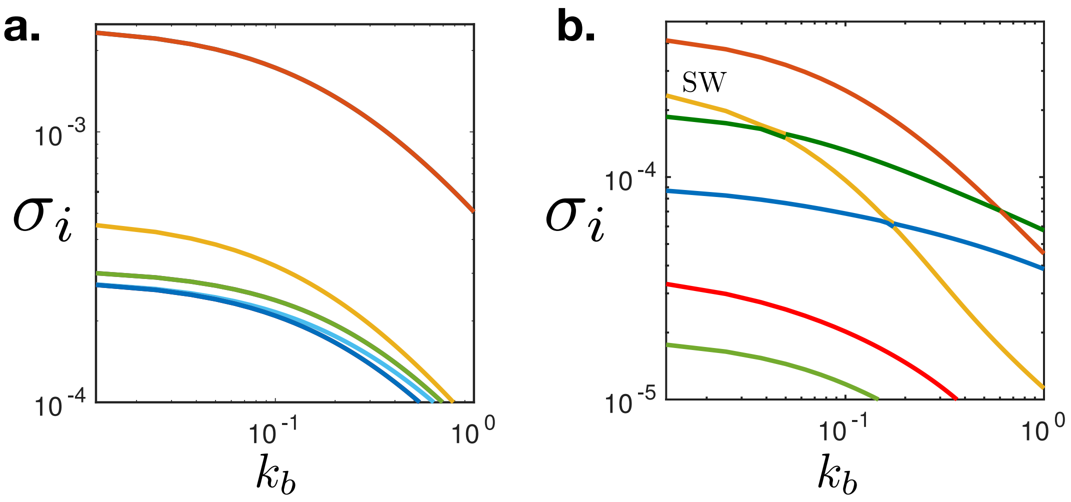

Fig. 3.7. Plot of the eigenvalues σ_i of PCP (colored lines, top panel) as a function of the bond angle rigidity parameter k_b, showing the effect of including bending rigidity of bonds in the triangular **a.** and planar honeycomb **b.** structures. While the relative prominence of the modes is unaffected in the triangular lattice except for the breaking of degeneracy of some low probability modes, in the honeycomb lattice the mode corresponding to the SW defect precursor (yellow) is strongly suppressed with increasing k_b (see text).

continue to be the most prominent modes in the system. Less importantly, the addition of bond bending also breaks the degeneracy of some of the modes corresponding to small eigenvalues.

In contrast to the triangular lattice, the relative prominence of non-affine modes in the planar honeycomb is strongly dependent on the value of the bending constant. Fig. 3.7 shows the first six eigenvalues against k_b. Several crossovers among the different modes are visible in these spectra. We notice that the SW mode, which earlier was the second most prominent mode in the system, becomes strongly suppressed as one increases k_b. This was to be expected because the SW defect requires that nearest neighbor bonds become flexible. Our projection formalism is hence very general and can pick out the dominant defect precursor modes for arbitary lattice symmetry and interactions.

3.1.4 The Kagome lattice in $2d$

The Kagome lattice structure is found in many natural minerals and has interested physicists and chemists because of its unusual magnetic properties [1, 82]. Similar to the planar honeycomb, a kagome lattice has a triangular symmetry, but with three basis particles in each cell. Each particle in the cell has four nearest neighbor and four next nearest neighbors. The dynamical matrix (Appendix A.1) $D(\mathbf{q})$ becomes a 6×6 matrix

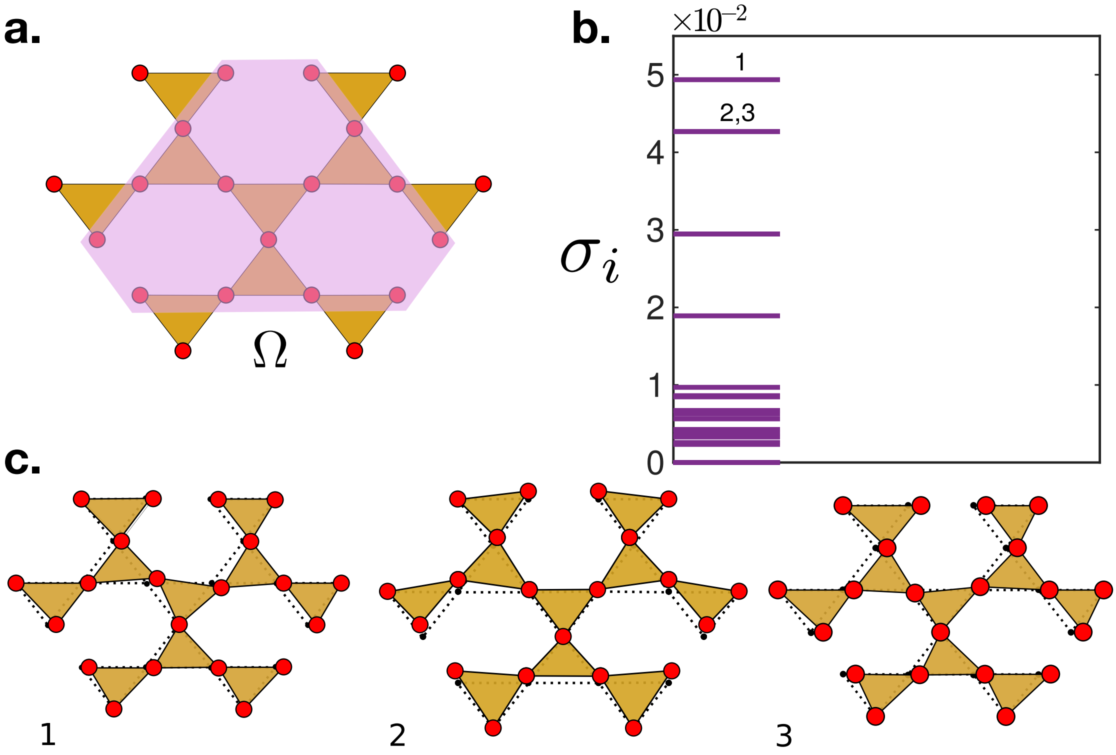

Fig. 3.8. **a.** Schematic of the Kagome lattice and coarse-graining volume Ω (pink shaded region), **b.** the spectrum of non-affine modes and **c.** 1-3, the three most prominent non-affine modes. Parameters used: $k_2 = 0.5$, $\beta = 100$.

and has two acoustic branches and four optical ones. Fig. 3.8 shows the coarse-graining volume Ω, which contains 21 pairs of particles up to the next nearest neighbor distance so that P becomes a 42×42 matrix. Accordingly, PCP has 38 non-zero eigenvalues corresponding to non-affine eigenmodes. The probability distribution $P(\chi)$ is shown in Fig 3.2. Fig 3.8 shows the eigenvalue spectrum. Similarly to the planar honeycomb we notice the absence of any large gap among the eigenvalues. The non-affine modes for the largest eigenvalues are shown in Fig. 3.8. These modes turn out to be the well known floppy modes [83]. If the next nearest neighbor bonds are stiffened or bond angle dependent potentials are introduced, the amplitudes of these floppy modes decrease, exactly as in the honeycomb lattice.

3.1.5 The simple cubic lattice in $3d$

Our discussion of lattices in three dimensions begins with the simple cubic (SC) lattice, having a single basis atom in a cubic cell with six nearest neighbor and twelve next nearest neighbor particles. We assume that these particles are connected by springs

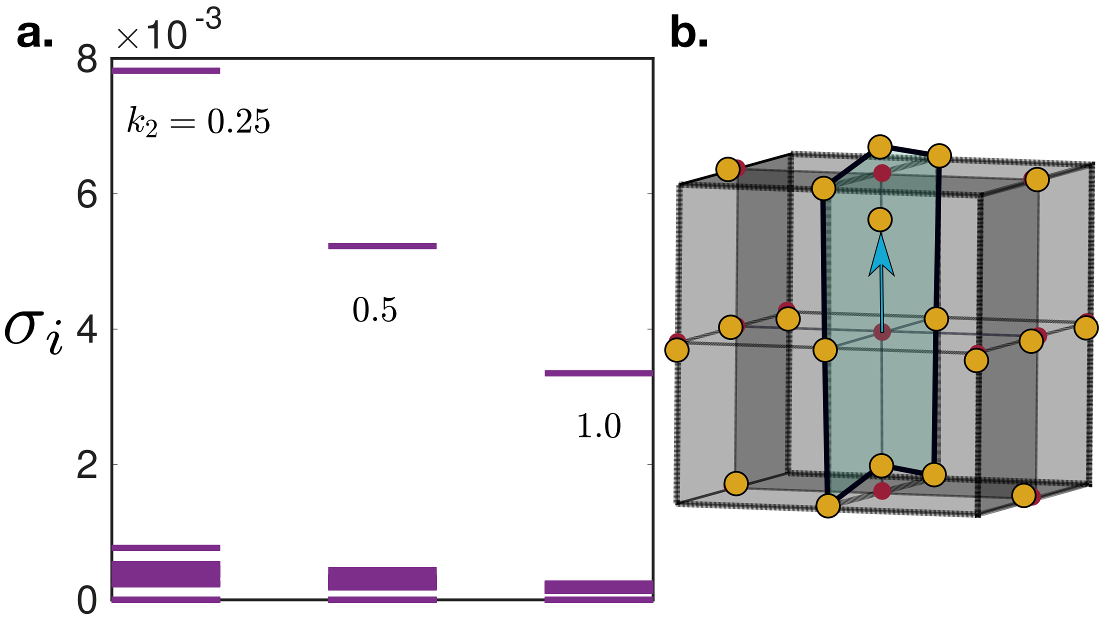

Fig. 3.9. **a.** Plot of the eigenvalues of the SC lattice for three different values of k_2: 0.25, 0.5 and 1.0. **b.** The non-affine mode corresponding to the largest eigenvalue for $k_2 = 0.5$ and $\beta = 1000$. Note that this is similar to what is obtained for the square lattice.

with stiffness constant k_1 for nearest neighbors and k_2 for next nearest neighbors. The dynamical matrix (Appendix A.1) can be calculated and has three acoustic branches comprising one longitudinal and two transverse phonon modes. We proceed in a similar fashion as in 2d to calculate C. The projection matrix has 54 eigenvalues out of which 9 are zero corresponding to nine affine modes in $3d$. Similar to the triangular and square lattices in 2d, we find that a large gap exists between the largest eigenvalue of PCP and the rest, see Fig. 3.9. For the SC, we find that three degenerate modes correspond to this largest eigenvalue, one of which is shown In Fig. 3.9. Note that the displacement pattern in the blue shaded plane in SC is similar to that in the square lattice. Indeed the SC lattice may be regarded as a stacking of 2d square lattices. The other two degenerate modes show the same movement in the other two orthogonal planes of the SC. This leads to the interpretation that the most prominent non-affine mode of the SC lattice simply tend to convert the stacked planes from square to triangular symmetry, hence generating 3d close packed structures [1].

The eigenvalue spectra in Fig. 3.9 also show that χ decreases as one stiffens the lattice by increasing the stiffness constant k_2. However, this increase in stiffness does not affect the qualitative features of the spectrum including the continuing presence of a gap.

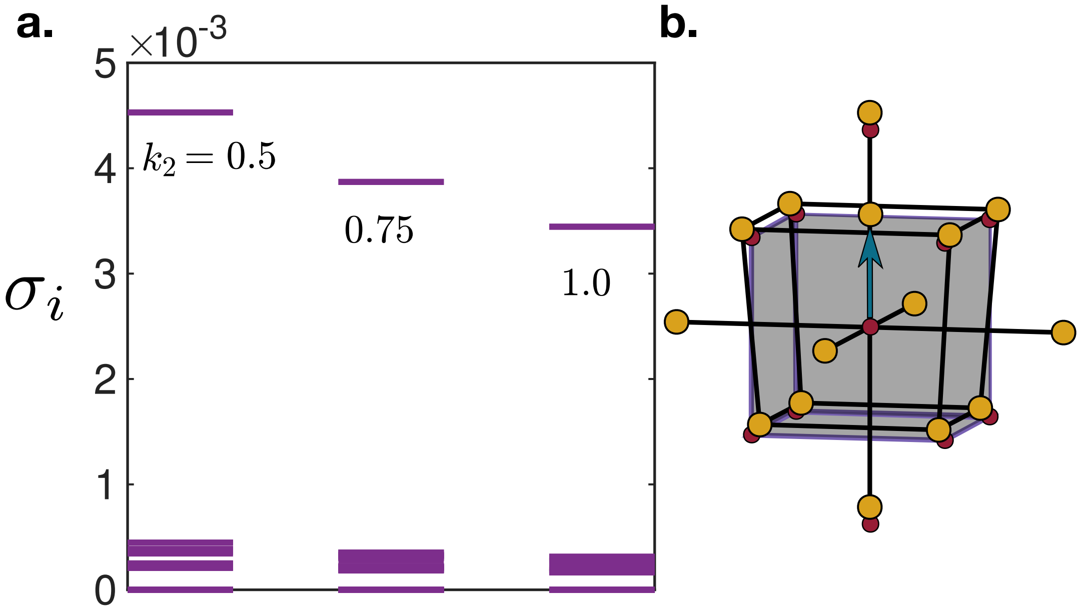

Fig. 3.10. **a.** Plot of the non-affine eigenvalues of the BCC lattice for three different values of k_2: 0.5, 0.75 and 1.0 at $\beta = 1000$. **b.** One of the non-affine modes with the largest eigenvalue for $k_2 = 0.75$.

3.1.6 The body-centered cubic lattice in $3d$

The body centered cubic (BCC) lattice may be thought of either as a system with a single-atom basis, or as a SC lattice with a two atom basis [1]. For reasons of computational simplicity we choose the former view to construct our coarse-graining volume: this consists of 14 particles with 8 nearest neighbors having bond stiffness $k_1 = 1$ and 6 next nearest neighbors with bond stiffness k_2. Since Ω comprises 14 particles, in three dimensions P becomes a 42×42 matrix, and has 33 non-zero eigenvalues corresponding to the non-affine part.

After performing the projection analysis, we find that a gap below the largest eigenvalue is present regardless of the choice of k_2. We notice that as for all other lattices discussed above, $\langle \chi \rangle$ decreases with an increase in the stiffness of the lattice, see Fig. 3.10. BCC has three degenerate modes related to the largest eigenvalue. One of these is shown in Fig. 3.10, where we notice that the centre particle has moved along the $[001]$ direction. The other two modes show a displacement of the centre particle in the two orthogonal directions. These dominant modes together represent the motion of the body centered particle to one of the six faces of the cubic unit cell, which can be viewed as generating locally a single atomic plane of the FCC lattice by an atomic shuffle.

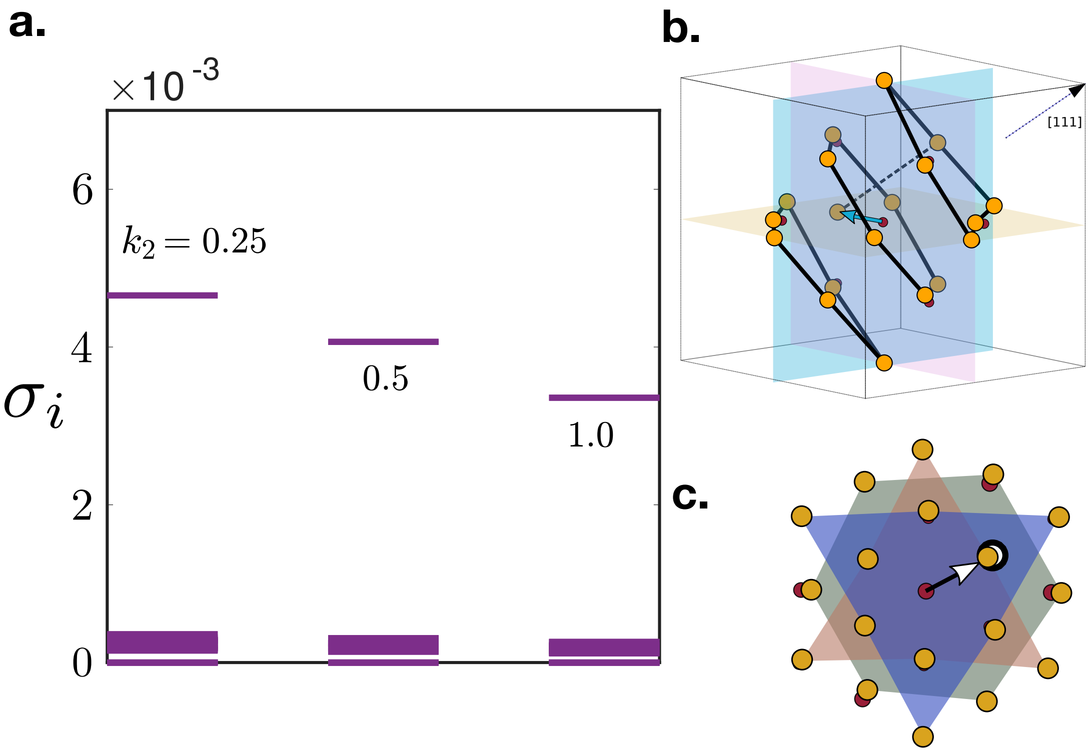

Fig. 3.11. **a.** Plot of eigenvalue spectra of FCC for different choice of k_2 : 0.25, 0.5 and 1.0 at $\beta = 1000$. **b.** The eigenmode corresponding to the largest eigenvalue for $k_2 = 0.5$. **c.** Same as **b.** but viewed from the $[111]$ direction. Notice that the central particle has displaced out of plane and sits below a particle from a different stacking layer, resulting in a stacking fault in the FCC system.

3.1.7 The face centered cubic lattice in $3d$

The coarse-graining volume for the face centred cubic (FCC) lattice, we construct around a single atom basis, similar to the BCC case. It consists of 12 nearest neighbor particles and 6 next neighbors. We thus have $18 \times 3 = 54$ eigenvalues of PCP, of which 9 eigenvalues representing affine deformations are zero. The eigenvalue spectrum again shows a prominent gap between the three largest degenerate (and mutually orthogonal) eigenmodes and the rest. It is also obvious from the spectra that $\langle \chi \rangle$ decreases as one increases the stiffness of the lattice by increasing k_2.

One of the three non-affine modes corresponding to the largest eigenvalue is shown in Fig. 3.11. We show later that this mode is a precursor to either a slip or a stacking fault [1, 3]. The other two degenerate modes show the analogous deformation in orthogonal directions.

3.2 Coupling between affine and non-affine displacements

While the affine and non-affine components of the displacements are orthogonal to each other by construction, they couple at higher order [5]. This has the physical meaning of suggesting that at higher strains, fluctuations which tend to create lattice defects become more probable. While this has been noted in the triangular lattice [5, 37], here we undertake a systematic study involving many lattices.

In Section 2.3 we showed that this coupling is determined by the commutator $[\mathsf{P}, \mathsf{C}]$. We have computed this commutator for all the lattices considered in this paper and the results are shown in Table. 3.1. It is interesting to see that in $2d$ open lattices like the planar honeycomb and kagome have much larger values of this coupling than the mono atomic, more close packed ones. In $3d$ no marked trend is observed among the cubic crystal family; the differences are too small to be significant and may have a weak dependence on details of the interactions even after normalization.

Lattice Type	$\|\|C\|\|$	$\frac{\|\|[P,C]\|\|}{\|\|C\|\|}$	Parameters (k_2,k_b)
2d triangle	3.874	0.031	0.5, 0
2d triangle	1.290	0.013	0.5, 0.5
2d square	5.055	0.037	0.5, 0
2d honeycomb	9.362	0.160	0.5, 0
2d honeycomb	4.897	0.135	0.5, 0.5
2d kagome	9.910	0.113	0.5, 0
3d SC	9.361	0.024	0.5, 0
3d BCC	6.994	0.020	0.75, 0
3d FCC	7.279	0.025	0.5, 0

Tab. 3.1. The Frobenius norm (the square root of the sum of the absolute squares of the elements) of the commutator $[\mathsf{P}, \mathsf{C}]$, made dimensionless by dividing it by the corresponding norm of C, for a number of lattices in 2d and 3d at $\beta = 1$. Corresponding parameter values for stiffness are quoted in the last column. Also note that the norm of P is essentially the square-root of total number of non-affine modes in each case.

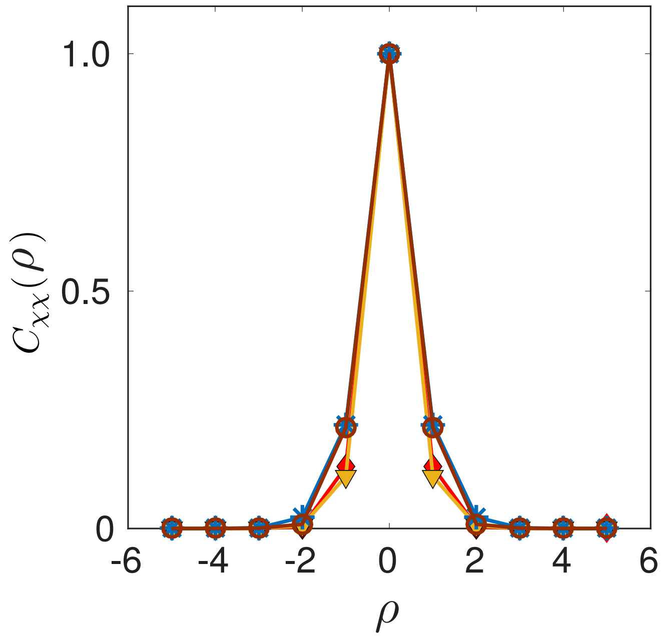

Fig. 3.12. Normalized χ correlations, $C_{\chi\chi}(\rho) = (\langle\chi(0)\chi(\rho)\rangle - \langle\chi(0)\rangle^2)/\left(\langle\chi(0)^2\rangle - \langle\chi(0)\rangle^2\right)$, for several different lattices as a function of distance $\rho = \mathbf{R}\cdot\hat{\mathbf{x}}/d_{nn}$ measured in units of the *nearest neighbor distance*, d_{nn} in the reference lattice along one coordinate axis. Brown and blue are for square and triangle lattices ($d_{nn} = a$); orange and red are for FCC ($d_{nn} = a/\sqrt{2}$) and BCC ($d_{nn} = a\sqrt{3}/2$) respectively.

3.3 Spatial correlations for $2d$, $3d$ mono-atomic lattices

We now look at two-point spatial correlations of χ and the affine strains $\mathbf{e}$. These have been extensively studied for two dimensional lattices both numerically [61, 63] and analytically [5–7]. The spatial correlation of the affine strain is important because it offers a way to obtain elastic properties of colloidal crystals from optical microscopy images [47].

The spatial correlations of χ for some of the lattices considered in this paper are shown in Fig. 3.12 in a single plot. These correlations are nearly isotropic and are plotted as a function of distance ρ measured in the units of nearest neighbor distance d_{nn} along one coordinate axis. The values of d_{nn} for different lattices are mentioned in Fig 3.12. We observe that the nature of the correlation function is similar for all lattices. It is a sharply decaying function that essentially vanishes after the second neighbor shell. More quantitatively, we observe that the correlations decay somewhat faster in higher dimensions.

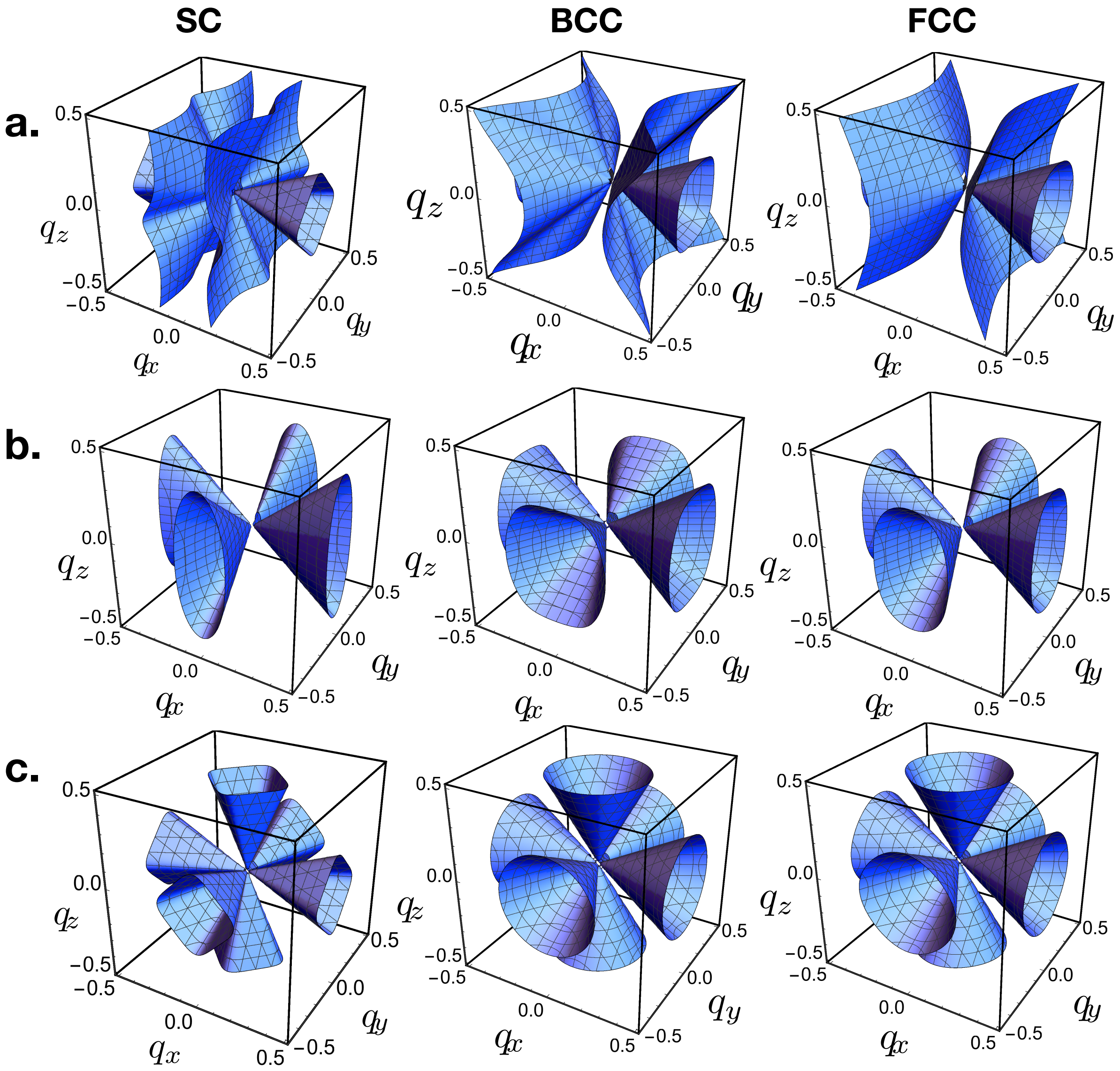

Fig. 3.13. Iso-strain surfaces for the strain-strain correlation functions in Fourier space and in the $\mathbf{q} \to 0$ limit for SC, BCC, FCC lattices. Figures shown for **a.** deviatoric $(e_{xx} - e_{yy} - e_{zz})$, **b.** shear $(e_{xy} + e_{yx})$ and **c.** volume $(e_{xx} + e_{yy} + e_{zz})$ strains. The values of the correlations at the iso-surfaces are different in each case and have been chosen for ease of presentation. They are listed in the Appendix A.2 along with the full algebraic expressions used to plot the iso-surfaces. The other parameters used are $k_2 = 1/6$ and $\beta = 1$ throughout.

The spatial correlations for the affine strains may be obtained using the procedure outlined in Section 2.3.1. These have a more non-trivial structure. They are anisotropic and can be long-ranged along particular directions [63]. In the $\mathbf{q} \to 0$ limit, analytic expressions for these correlation functions can be derived quite easily. For example, as defined in Eq. (2.47), the strain correlation functions for the square lattice are, $\beta\langle e_v^2\rangle(\mathbf{q}) = Q_v/Q$, $\beta\langle e_u^2\rangle(\mathbf{q}) = Q_u/Q$, and $\beta\langle e_s^2\rangle(\mathbf{q}) = Q_s/Q$ with the abbreviations

$$\begin{aligned}
Q &= q_x^2 q_y^2 + k_2\left(q_x^2+q_y^2\right)^2 + k_2^2\left(q_x^2-q_y^2\right)^2 \\
Q_v &= 2q_x^2 q_y^2 + k_2\left(q_x^2-q_y^2\right)^2 \\
Q_u &= 2q_x^2 q_y^2 + k_2\left(q_x^4+6q_x^2q_y^2+q_y^4\right) \\
Q_s &= \left(q_x^4+q_y^4\right) + k_2\left(q_x^2-q_y^2\right)^2
\end{aligned} \tag{3.3}$$

Similar expression for the triangular lattice have already been discussed in [5]. We observe that for $k_2 = 1/2$, where the square lattice becomes elastically isotropic [84, 85], the expressions in Eq. (3.3) differ from those for the triangular lattice only by an unimportant overall factor. The general shape of these correlation functions, viz. the "butterfly pattern", is also similar to results obtained in colloidal glasses using video microscopy techniques [86].

In three dimensions, the correlation functions are considerably more complicated, although analytic expressions in Fourier space in the small wave-number limit can still be worked out with some effort. The algebraic expressions are given in Appendix A.2 and they are plotted in Fig. 3.13.

3.4 Summary and conclusion

In this chapter we have studied the nature of thermally excited non-affine atomic displacements for a number of crystalline solids in 2d and 3d. In all cases, we showed the non-affine modes serves as the precursors to commonly observed lattice defects. We have discovered several features that are common to many lattice systems although close packed and open lattices show somewhat different properties. While in close packed lattices, the contribution to χ is dominated by a single non-affine mode (or degenerate, symmetry-related class of modes), in open lattices there is no such predominance. Further, in open lattices, the contribution of the different modes is much more sensitive to details of the interactions and they are more strongly coupled to affine fluctuations. Additionally, we observed that for both lattices in 2d and 3d, the spatial two-point correlation for χ decays exponentially; though somewhat faster in $3d$.

In the next chapter we show how non-affine fluctuations in crystals are related to deformation modes.

4

Non-affine displacements and deformation modes

4.1 Deformation of solids: a brief background

In earlier chapters we have studied the nature of thermally excited non-affine atomic displacements for a number of crystalline solids in 2d and 3d. We have discovered several features that are common to many lattice systems although close packed and open lattices show somewhat different properties. While in close packed lattices, the contribution to χ is dominated by a single non-affine mode (or degenerate, symmetry-related class of modes), in open lattices there is no such predominance. Further, in open lattices, the contribution of the different modes is much more sensitive to details of the interactions and they are more strongly coupled to affine fluctuations.

One of the important findings of earlier work [6, 7] was that non-affine displacement fluctuations serve as precursors to the formation of defects. In the triangular lattice, in the presence of strain, a dislocation-anti-dislocation pair separates and produces a slip plane [37] that has high values of χ. In this chapter we conclude this analysis by carrying out a simple exercise in order to better understand the relation between non-affine modes and defects[39, 40, 87, 88].

4.2 Deformation of the triangular solid

We consider, first, a triangular lattice where a slip is introduced such that a part of the lattice moves a lattice spacing in a close packed direction, compared to the rest. In the bulk, there is no contribution to χ as all atoms undergo either no motion or just a uniform translation. Thermal vibrations are neglected in this calculation and those that follow. We choose a coarse graining volume corresponding to the smallest Ω as shown in Sec. 3.1.1 centered on an atom lying in the slip plane. The Ω at the interface of the slipped and un-slipped regions is, of course, deformed (see Fig. 4.1). This deformation cannot be described by a homogeneous affine transformation of Ω

and therefore contributes to χ. Including thermal contributions would produce a $P(\chi)$ that is identical to the ones calculated in the bulk (Section 3.1), while in the vicinity of the slip, $P(\chi)$ would be displaced to higher χ values [37].

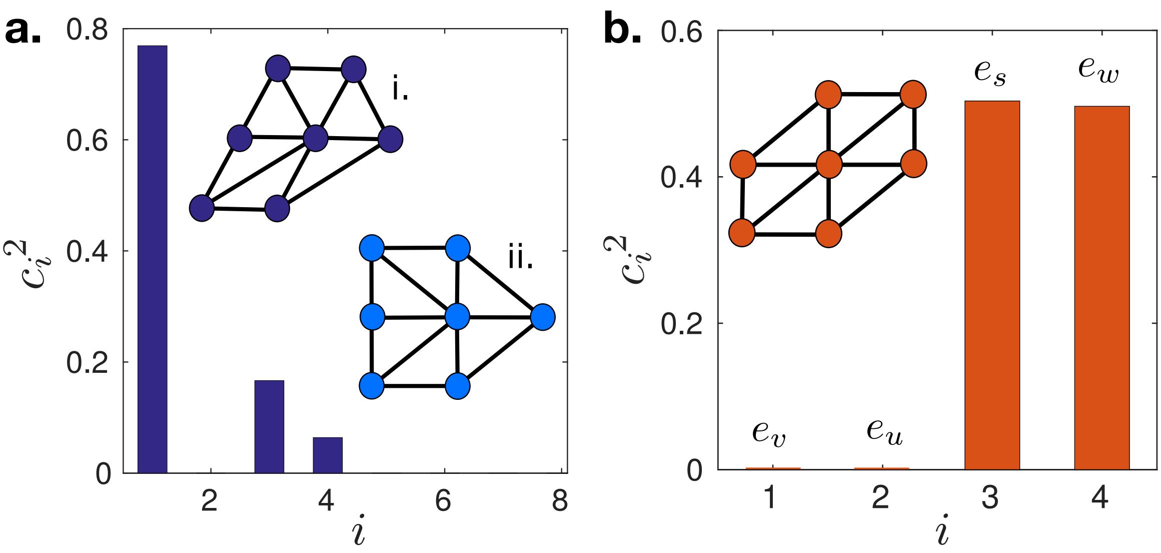

Fig. 4.1. **a.** Relative contribution from non-affine modes when a slip is introduced by translating the bottom half of a triangular lattice along a close-packed direction by a lattice spacing. **b.** The corresponding contribution of the four affine modes. Note that the largest contributions come from shear and rotation. The insets show the configuration of atoms in Ω after the slip (**a**-i) and the separate non-affine (**a**-ii) and affine (**b**) contributions. See text for details.

One can now project this deformation onto the non-affine and affine modes computed from thermal averages of displacements to find the contribution of individual modes to this deformation. In Fig. 4.1, we plot the bar-graph of the components $(c_i)^2$ obtained by projecting onto the affine and non-affine modes for this deformation, where c_i is the coefficient corresponding to the i^{th} mode in the expansion of the displacement as a superposition of non-affine and affine modes. We see that the largest contribution comes from the first two non-affine modes as expected. There is also a non-zero contribution from the affine modes, with the affine and non-affine modes contributing equally overall. This may be easily understood from the insets shown in Fig. 4.1**a** and **b**. In Fig. 4.1**a** (inset i), we show the configuration of particles where the two atoms belonging to the bottom-most row are displaced to the left by a lattice spacing relative to the upper two rows. The total non-affine contribution is shown in inset ii of the same figure. This shows a relative displacements to the right of the middle row consisting of three atoms. On the other hand, the affine contribution to the slip shown in Fig. 4.1**b** (inset) consists of *homogeneous* shear and local rotation as verified from the bar-graph. It is clear that the sum of the affine and non-affine displacements gives rise to the slipped configuration shown in Fig. 4.1**a** (inset i). The affine deformation produces an internal shear stress at the slip plane. When a crystal slips in response to an external homogeneous shear, the internal stress cancels the external stress locally. By introducing a finite density of such slip planes, any homogeneous stress may be expelled. In Ref. [37] such an expulsion process was shown to lead to yielding of crystalline solids at any shear stress, however small. Since the non-affine strains corresponding to the largest eigenvalues do not depend on the choice of Ω (see Section 3.1.1), the mechanism described is quite general.

4.3 Deformation of the square solid

We now turn to the square lattice. It is known [35] that a square lattice can transform to a triangular lattice by either a homogeneous, affine, shear or by a non-affine deformation where alternate rows of atoms shift by half a lattice spacing together with a homogeneous relaxation of the lattice parameters. We show this deformation in Fig. 4.2 (inset) and compute the projection onto the non-affine modes. As expected, there is an overwhelmingly large contribution from the non-affine mode with the largest eigenvalue. There is no affine component for this deformation.

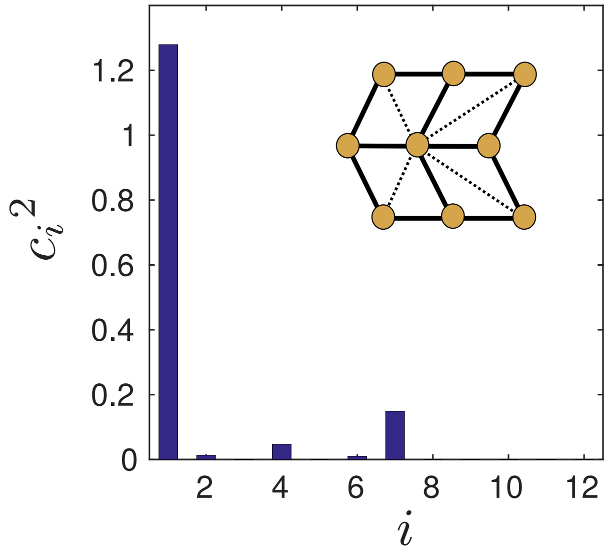

Fig. 4.2. Non-affine contribution in the square lattice when the middle row is displaced by half a lattice spacing. Note that this transformation tends to produce a triangular lattice symmetry starting from the original square lattice.

4.4 Deformation of the FCC solid

For the FCC lattice, we first create a slip along one of the close-packed planes, similar to the triangular case. Fig 4.3 shows the original position (triangle with a dotted boundary) and the new position (blue shaded triangle) of the closed packed plane. The bar-graph of ${c_i}^2$ corresponding to non-affine and affine modes makes it clear that slip in the FCC lattice behaves similarly to a slip in the triangular lattice: we also observe here that the total contributions of the affine and non-affine modes are equal. In the 3d FCC lattice apart from a slip, one can also consider a stacking fault. Fig 4.3 also shows this deformation where the closed packed plane is displaced by half a lattice parameter. The shaded blue region in Fig 4.3 represents the new position of the closed packed plane. Again during a stacking fault it is observed that the non-affine and affine parts contribute equally and the maximum contribution comes from the first three non-affine modes.

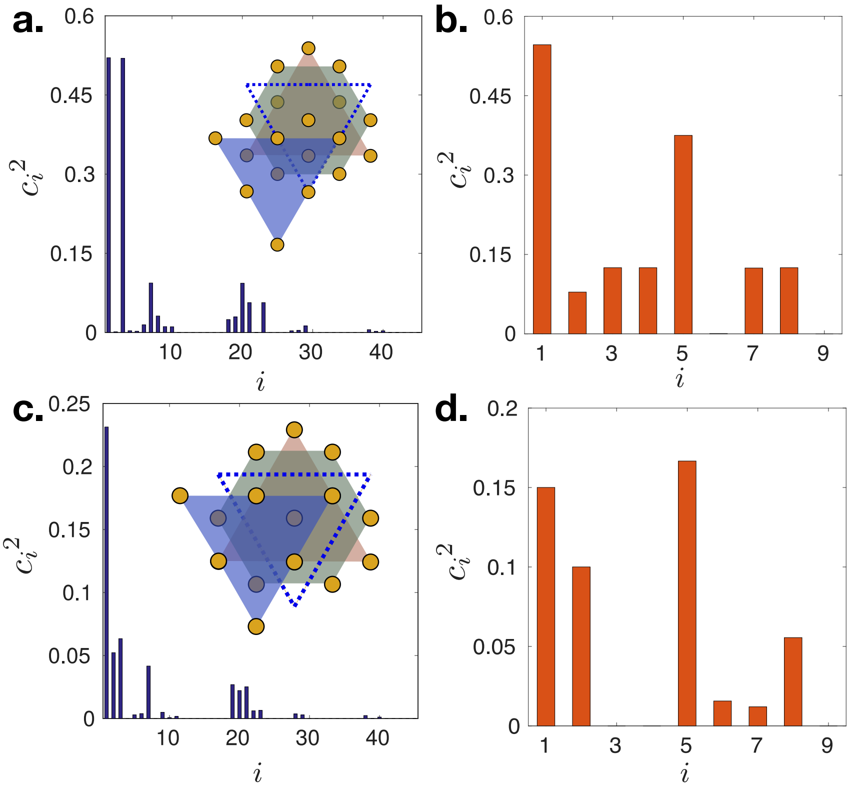

Fig. 4.3. Contribution from different **a.** non-affine and **b.** affine modes when one introduces a slip in the FCC lattice. The inset shows a schematic diagram of the lattice as seen from the $[111]$ direction. The original position of the close packed lattice plane is shown as a triangle with a blue dotted boundary and the final position as a blue shaded triangle. Contribution from a stacking fault from **c.** non-affine and **d.** affine modes. The inset shows, as before, the original and final positions of a close packed plane of atoms.

4.5 Summary and conclusion

The simple exercise described in this chapter therefore strengthens our claim that the non-affine modes that belong to the largest eigenvalues of PCP are related to fluctuations that tend to nucleate defects. We have seen in [37] that these fluctuations condense under external strain to cause plastic deformation in a 2d triangular crystal. The computations presented here show that non-affine modes deduced from small harmonic fluctuations at $T > 0$ are able to describe important processes that occur during large $T = 0$ deformations. We hope that this knowledge will enable us to study in detail mechanical properties of 3d cubic lattices.

We believe that our work brings out an interesting aspect concerning defects and the dynamics of deformation in crystalline solids [1, 3, 23]. Atomic fluctuations that generate defects in close packed crystals are shown to be determined by the non-affine modes with the largest eigenvalue. Representing fluctuations in crystals as consisting of smooth phonons and singular defects therefore amounts to making a "largest eigenvalue approximation" and neglecting other non-affine modes that make smaller contributions to the total χ. This approximation lies at the heart of all dislocation based theories of crystal plasticity [3, 23, 89, 90]. Such an approximation is excellent when the defect-like mode is separated from the others by a large gap in the spectrum of non-affine eigenvalues as in the triangular (Section 3.1.1) and FCC (Section 3.1.7) lattices. However, the approach may not work for crystal lattices where such a gap does not exist or is too small, e.g. for the planar honeycomb (Section 3.1.3) or kagome (Section 3.1.4) structures. In amorphous matter also this approximation may not be so useful, even if dislocation-like structures are identifiable [27]. In such cases, new continuum theories of deformation that include *all* non-affine modes (or at least a large class of them) may be needed. Furthermore, anharmonic effects may be important in amorphous systems, such that the harmonic approximation may itself break down [91, 92]. A more complex theory may be able to address such issues. Such a theory does not exist at present and we hope that our work provides sufficient motivation to the community for thinking along these lines.

In Chapter 2- 4, we have developed a procedure for decomposing atomic fluctuations into affine and non-affine parts. The non-affine displacements have been shown to be precursors for defects and are related to deformation modes of the solid.

In the next two chapters we show how this knowledge may be used for practical purposes viz. stabilising patterns in *colloidal crystals* and in *swarm of drones*. The key idea involves our ability to selectively bias non-affine fluctuations using the thermodynamically conjugate field h_X [6]. This field is analogous to external stress which couples to the affine part of the displacements, and can influence the formation of defects. Naturally, we ask is it sufficient to suppress the non-affine modes to stabilise the lattice ? If it is the case, does it depend on the nature of interactions or symmetry of the lattice. We try to answer these question in next chapter.

5

Stabilising colloidal crystals

In this chapter we show that any colloidal crystal of any desired symmetry can be stabilized regardless of interactions if non-affine fluctuations are suppressed using appropriate conjugate field.

Discovery and development of techniques to form stable, complex assemblies of colloidal particles has emerged as a rather vibrant sub-field of soft condensed matter physics and materials science [8–11]. Colloidal particles, synthesized using a variety of routes into an array of shapes and sizes from nanometers to microns are now, readily available for use [11]. Apart from many technological applications, assemblies of such colloids into ordered crystals offer us unique insights into properties of ordinary solids and their behaviour. This is facilitated by the relatively large size and consequent slow timescales [54, 93, 94] of a colloidal particle enabling one to use simple optical means to observe and manipulate them [47, 95, 96]. One encounters, mainly, two paradigms related to the assembly of colloids into complex structures.

In the first case, the interactions between colloidal particles are tuned. This may be done either by controlling the shape [97], by alloying [98, 99] or by adding specially reactive patches or tethers [100, 101]. Apart from this, confinement, either between glass plates [58, 59] or at an interface [102, 103], induce effective interactions between colloidal particles influencing their structure. While one obtains a degree of control over the symmetry and properties of the colloidal crystals so produced, producing complex structures is difficult and needs careful synthesis and/or cumbersome fine tuning of many parameters.

On the other hand, one may also produce ordered colloidal crystals using templates [104]. These templates may be either permanent, such as etched onto a surface, or reconfigurable, if produced by optical means [57, 105, 106]. The latter technique has the advantage that a large variety of crystal [105], quasi-crystal [57] and even random structures [106] may be produced. Nevertheless, periodic crystals induced by static templates necessarily suffer from a fundamental flaw.

While crystallisation due to inter-particle interactions, necessarily breaks the continuous translational and orientational symmetry of the liquid *spontaneously*, uniform translations of the crystal as a whole in any direction or global rotations about any axis still do not cost energy. This gives rise to Goldstone modes viz. acoustic phonons whose frequencies vanish with increasing wavelength (or decreasing wavenumber) [1]. On the other hand, templates break translational invariance *explicitly* by destroying spatial homogeneity [107]. Uniform translations of the whole crystal in one or more directions now cost energy and some or all vibrational modes become massive, i.e. their frequencies do not vanish with decreasing wavenumber. In the extreme case of deep periodic traps, particles do not interact with each other at all and oscillate independently in isolation, making the spectrum of vibrational frequencies resemble that of a trivial Einstein crystal [2]. This has a profound influence on scattering processes at small wave-numbers since fewer low energy vibrational modes remain. While for many applications, such as colloidal epitaxy [11, 104], this may not present a problem, for many others it is an issue to be addressed. For example, constructing colloidal models of solid-solid transformations [108] and interfaces [45], mechanical behaviour of crystals [3], crystal - glass transition [60] etc. require that such spurious effects be avoided.

The rest of the chapter is organised in the following way. In the next section we introduce our proposal, which uses a feedback mechanism to stabilise target structures for any kind of colloidal particle. This is followed by our specific results for, first a harmonic network of particles as a test case and then a colloidal solid modelled by an isotropic pair potential. We then indicate how our scheme may be generalised to more complex structures and to higher dimensions. Towards the end, we explain the mechanism behind our proposal and discuss its experimental realisation by comparing our strategy to other existing methods. Finally we conclude with a summary and outlook for future work.

5.1 The feedback loop

First, the target lattice S_T, is “read in” as a set of reference coordinates $\{\mathbf{R}_i\}$ (see Fig. 5.1). We assume, for simplicity that S_T is a Bravais lattice with a single particle basis. Later we show how this procedure may be generalised to more complex structures. Unlike a physical template, the target lattice or structure, which we wish to stabilise, remains in the memory of a computer coupled to an optical setup. Note that there is no restriction on the choice of $\{\mathbf{R}_i\}$. Next, around each particle i, we fix a neighbourhood Ω containing a fixed set of tagged particles whose instantaneous coordinates $\mathbf{r}_i$ are recorded. Particle positions undergo thermal fluctuations due to the presence of the solvent. Using the well defined projection formalism, which we have established in previous publications [5, 6], we separate these thermal particle displacements into affine

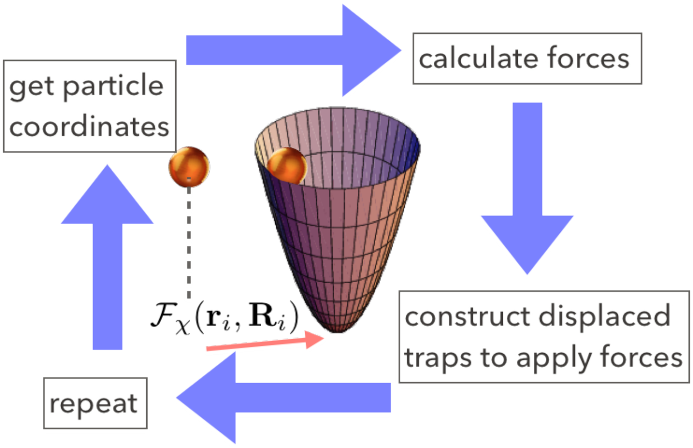
get particle coordinates
calculate forces
construct displaced traps to apply forces
repeat
$\mathcal{F}_\chi(\mathbf{r}_i, \mathbf{R}_i)$

Fig. 5.1. Schematic diagram showing the steps involved in generating feed-back controlled optical traps. The particle coordinates are obtained from video microscopy. The neighbourhood of each particle is recorded and the force $\mathcal{F}_\chi(\mathbf{r}_i, \mathbf{R}_i)$ (see text) calculated from the Hamiltonian 5.1. Next, the positions of optical traps needed for applying these forces are calculated and the traps deployed. If this procedure is continuously repeated for all particles at a rate comparable to typical vibrational frequencies of the colloidal particles, a uniform stabilising field is obtained.

and non-affine subspaces. A laser tweezer is used to exert additional forces, $\mathcal{F}_\chi(\mathbf{r}_i, \mathbf{R}_i)$ to particle i which bias displacement fluctuations so that the non-affine component of the displacements is suppressed. Since $\mathcal{F}_\chi$ depends on *instantaneous* particle positions, they need to be be continuously updated by tracking particle trajectories in real time. Since intrinsic timescales of colloids are large, this is achievable using current video microscopic and spatial light modulation technology [109]. We derive below $\mathcal{F}_\chi$ for any given S_T.

The additional forces are computed from the following extended Hamiltonian [6, 30], $\mathcal{H} = \mathcal{H}_0 + \mathcal{H}_X$. Here $\mathcal{H}_0$ represents *any* Hamiltonian for interacting particles and,

$$\mathcal{H}_X = -h_X \sum_i^N \sum_{jk \in \Omega} (\mathbf{u}_j - \mathbf{u}_i)^{\mathrm{T}} \mathsf{P}_{j-i,k-i}(\{\mathbf{R}_i\})(\mathbf{u}_k - \mathbf{u}_i). \tag{5.1}$$

$\mathcal{H}_X$ involves the "projection operator" P and the particle displacements $\mathbf{u}_i = \mathbf{r}_i - \mathbf{R}_i$. The projection operator is a function only of the reference lattice and, for any particle i, is given by $\mathsf{P}^2 = \mathsf{P} = \mathsf{I} - \mathsf{R}(\mathsf{R}^{\mathrm{T}}\mathsf{R})^{-1}\mathsf{R}^{\mathrm{T}}$ and $j \in \Omega$ is a neighbour of i . Note that Eq.(5.1) preserves translational invariance viz., $\mathbf{u}_i \to \mathbf{u}_i + \mathrm{constant}$. One can also show (Chapter 2) [5, 6, 34], that $\mathcal{H}_X = -h_X \sum_i \chi_i$ where χ_i is the least square error made replacing particle displacements in Ω by the "best fit" *affine* strains [41]. The quantity $\chi_i = \boldsymbol{\Delta}^{\mathrm{T}}\mathsf{P}\boldsymbol{\Delta}$ where $\boldsymbol{\Delta}$ is the column vector of displacement differences [5, 34] with components $\Delta_{j\alpha} = u_j^\alpha - u_i^\alpha$ between particles i and all its neighbours j within Ω. The projection operator therefore projects out the *non*-affine part of $\boldsymbol{\Delta}$ and χ_i is the local non-affine parameter. Finally, the forces $\mathcal{F}^i_\chi = -\partial\mathcal{H}_X/\partial\mathbf{u}_i$. We show below that *suppressing non-affine fluctuations using negative values of h_X is sufficient to stabilise S_T*. The Hamiltonian $\mathcal{H}_X$ introduces new interactions among particles, which guarantee that the target lattice S_T is stabilised as long as $|h_X|$ is larger than a system size dependent threshold.

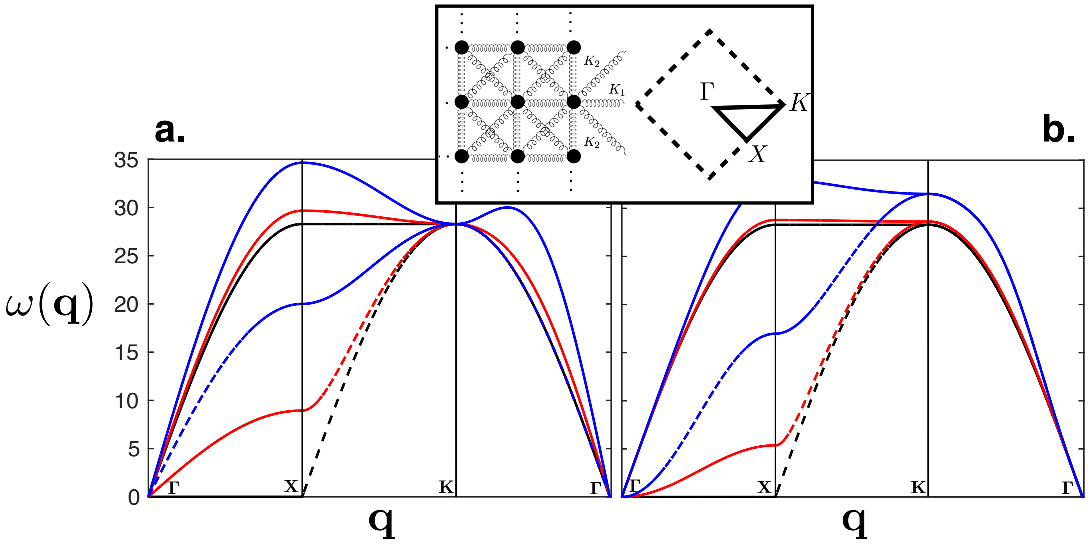

Fig. 5.2. **a.** Phonon dispersion curve $\omega(q)$ plotted along high symmetry directions for a square lattice network of vertices connected by springs. Both nearest neighbour and next nearest neighbour springs with spring constants $k_1, k_2 > 0$ are needed for stability. The longitudinal (transverse) modes are shown with solid (dashed) lines. The colours denote $k_2 = 0$ (black), 0.1 (red) and 0.5 (blue). **b.** Phonon dispersion for $k_2 = 0$ but now for various values of $h_X = 0$ (black), 0.003 (red), 0.03 (blue). Insets show the interaction volume Ω in the square lattice with bonds (left) and the high symmetry points of the corresponding Brillouin zone (right)

5.2 Application to colloidal crystals

5.2.1 Simple square lattice with harmonic interactions

It is instructive to demonstrate our procedure first for the case of N particles arranged as a 2d square lattice (see Fig. 5.2) interacting according to the Hamiltonian,

$$\mathcal{H}_0 = \sum_{i=1}^{N} \frac{\mathbf{p}_i^2}{2m} + \frac{k}{2}\sum_{i=1}^{N}\sum_{j\in\Omega, i<j} (|\mathbf{r}_j - \mathbf{r}_i| - |\mathbf{R}_j - \mathbf{R}_i|)^2. \tag{5.2}$$

Here $\mathbf{p}_i$ is the momentum of particle i, m the mass, $\mathbf{r}_i$ are the instantaneous positions, and $\mathbf{R}_i$ is the reference position in the target lattice. In this system, the length and energy scales are set by the lattice parameter l, and kl^2 respectively. The time scale is set by $\sqrt{m/k}$. We may chosee $l = m = k = 1$ without loss of generality. The dimensionless inverse temperature is given by $\beta = kl^2/k_BT$, with k_B the Boltzmann constant. The interactions have a range equal to the size of the coordination volume Ω. The nearest and next nearest neighbour vertices are connected by harmonic springs of strengths $k_1 = 1$ and k_2 respectively. The square lattice is mechanically unstable in the limit $k_2 \to 0$ due to softening of transverse phonon modes [110]. This is illustrated in Fig 5.2 **a** where we have plotted the phonon dispersion $\omega(\mathbf{q})$ for this harmonic square network for three different values of k_2. For $k_2 = 0$, frequencies correspond to the transverse mode becomes zero, resulting in an unstable square lattice. We now add the term proportional to h_X in (Eq.5.1) to the harmonic Hamiltonian $\mathcal{H}_0$ using the interaction volume, namely, the first and second neighbour shells of the square lattice as our choice of Ω (see Fig. 5.2 inset). The dynamical matrix [1, 2], corresponding to the full Hamiltonian $\mathcal{H}$ can be written as $D^{\mu\nu} = D_0^{\mu\nu} + D_X^{\mu\nu}$, where $D_0^{\mu\nu}$ is the dynamical matrix from $\mathcal{H}_0$ and

$$D_X^{\mu\nu}(\mathbf{q}) = -h_X \sum_{\mathbf{R}} \frac{\partial^2 X}{\partial u(\mathbf{R})^\mu \partial u(0)^\nu} e^{-i\mathbf{q}\cdot\mathbf{R}} \tag{5.3}$$

with the lattice sum over the reference set $\{\mathbf{R}_i\}$. After completing the sum over the square lattice, we obtain $D_X^{\mu\nu}(\mathbf{q}) = 2h_X \mathcal{A}_X(\mathbf{q})\delta^{\mu\nu}$ (details in Appendix B).

The function $\mathcal{A}_X(\mathbf{q}) \sim \mathbf{q}^4$ for small wave-numbers [32] so that $\mathbf{D}_X(\mathbf{q})$ does not affect the elastic properties, e.g. the speed of sound, of a mechanically stable lattice. Further, these results do *not* depend on the nature of $\mathcal{H}_0$. In Fig. 5.2**b** we plot the resulting phonon dispersion curves all at $k_2 = 0$ but for three different values of h_X. As h_X is made more negative, the transverse phonon mode appears to revive. One must note however that as $q \to 0$ the nature of $\mathcal{A}_X(\mathbf{q})$ dictates that the speed of transverse sound vanishes in the hydrodynamic limit. Nevertheless, for finite lattices, this limit is never reached since wave-numbers are cut off at $q = 2\pi/L$ where $L \propto N^{1/d}$ is the linear system size.

5.2.2 Simple square lattice with Gaussian interactions

Consider, next, a system of particles interacting by the soft, purely repulsive, "Gaussian core" model potential (GCM) [111, 112] where the harmonic interaction between particles i and j is replaced by the funtion

$$V_{ij} = \epsilon \exp(-r_{ij}^2/\sigma^2).$$

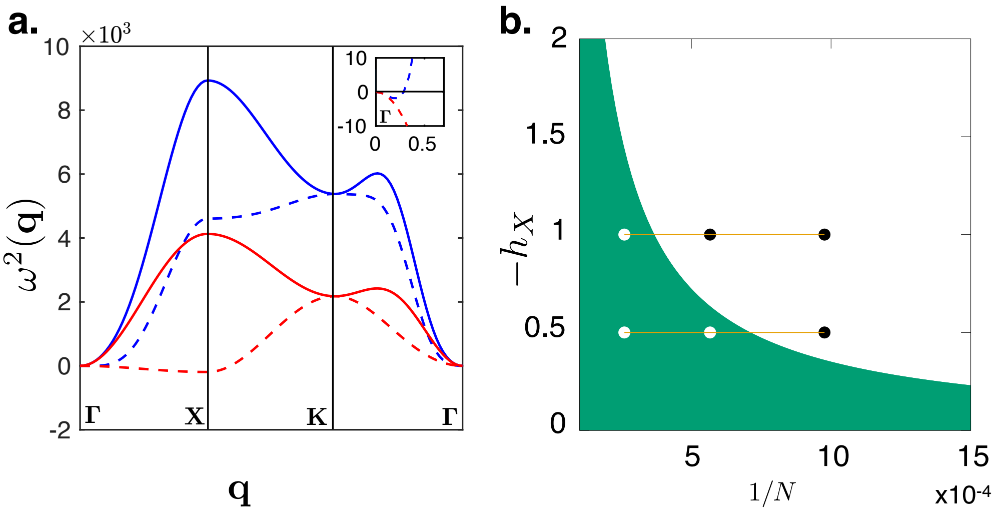

Fig. 5.3. **a.** Phonon dispersion curve $\omega^2(q)$ plotted along high symmetry directions for a square lattice of particles interacting with the GCM potential at $\rho = 0.5$ and $T = 1 \times 10^{-3}$. The small q region where $\omega^2 < 0$ is shown in the inset. We follow the same convention as in Fig. 5.2. There are two sets of curves for $h_X = 0$ (red curves) and $h_X = -0.5$ (blue curves). **b.** A stability diagram for finite size square lattices constructed from the dispersion curve in **a.** The green shaded region represents $-h_X$ values below which the square lattice becomes unstable ($\omega^2(q) < 0$). We have also marked six points on the graph such that black (white) circles denote stable (unstable) square lattices.

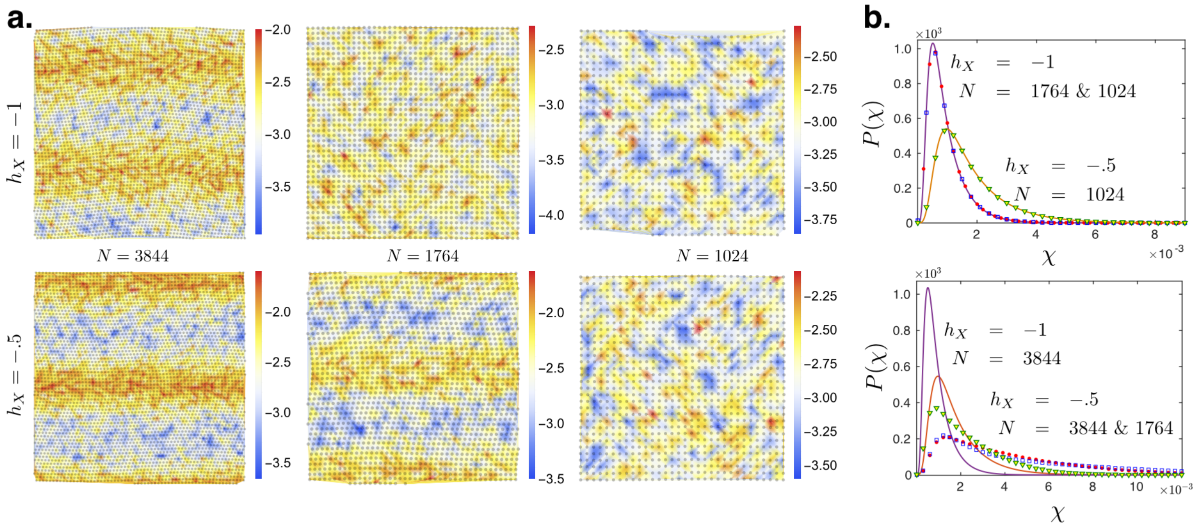

Fig. 5.4. **a.** Configurations obtained from Monte Carlo simulations after 6×10^6 MCS arranged according to the corresponding points marked off in Fig 5.3**b** verifying the stability condition. Colours correspond to the local value of χ. **b.** $P(\chi)$ obtained from the equilibrated configurations where the square lattice is stable (top) and unstable (bottom). The data points are computed from the results of our simulations and the lines are predictions of the harmonic theory [7]. The configurations and the curves are labelled by the corresponding h_X and N values.

Here $r_{ij} = |\mathbf{r}_i - \mathbf{r}_j|$ and the parameters ϵ and σ set the energy and length scales respectively and may be taken as unity. The GCM has been used to describe interacting star polymers which form a number of interesting solid phases in three dimensions.

In 2d, this system freezes into a triangular lattice with a possible intervening hexatic phase [113, 114]. GCM is also useful because the simple form of V_{ij} makes many analytic calculations possible. We study the model at reduced density $\rho = 0.5$ and temperature $T = 1 \times 10^{-3}$ where a triangular solid is stable [114]. The temperature used corresponds to about a tenth of the melting point of the stable triangular solid at this density. In general, we found that temperature plays a relatively minor role as long as anharmonic effects do not dominate and our results remain effectively valid even quite close to the melting point.

When particles interacting with the GCM potential are arranged in a *square* lattice, one obtains a mechanically unstable solid. Small displacement fluctuations from the ideal square lattice positions (where forces still vanish due to symmetry) makes the solid deform into the stable triangular structure via soft transverse modes [110]. This is clear from the calculated dispersion curve shown in Fig. 5.3**a** for $h_X = 0$.

We now turn on h_X defined exactly as in the case of the network. As h_X is decreased below zero, again, we see a revival of the transverse phonon mode. Unlike the network however, for all h_X, the transverse mode now has $\omega^2 < 0$ in a small region of $q \to 0$. Making h_X more negative can, nevertheless, restrict this region to extremely small q values which are not accessed by a solid of finite size due to the infra red cut-off discussed earlier. Since within a harmonic approximation, temperature enters only as a pre-factor, this leads to a T independent "stability diagram" as shown in Fig 5.3**b.**

To verify the stability diagram presented in Fig. 5.3**b** we perform Monte Carlo simulations with standard Metropolis updates [48] of a GCM solid with various N and h_X values keeping ρ and T same as before, equilibrating the system for a minimum of 10^6 Monte Carlo steps (MCS) starting from an initial square lattice. To check our results we obtained the probability distribution of the non-affine parameter $P(\chi)$ and compared it with the predictions from harmonic theory using the calculated dynamical matrix $D^{\mu\nu}$ as input [5, 7].

Equilibrated configurations from our simulations are presented in Fig. 5.4**a**. The h_X and N values for these configurations are marked in Fig. 5.3**b** It is clear that these results follow the expectations from our stability criterion. Once the stability threshold is breached, the square lattices destabilise due to $\mathbf{q} \to 0$ modulations. The local non-affine parameter χ rapidly rises as the crystal becomes unstable and is shown as a colour map. For all the stable square solids studied, our results were indistinguishable from the theoretical prediction though they deviate, as they should, if instability sets in (Fig. 5.4**b**). If ρ is increased, the harmonic approximation becomes more accurate and the magnitude of h_X needed to stabilise square lattices becomes even smaller.

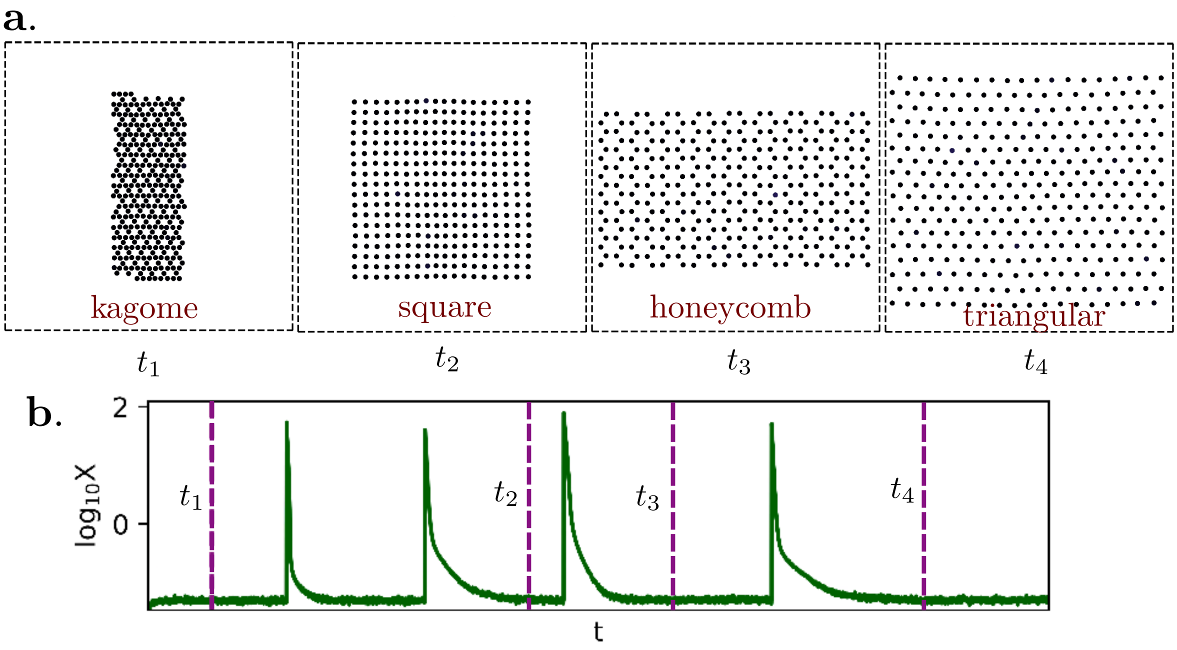

Fig. 5.5. Typical particle configuration from the simulation performed to stabilise complex and simple lattices. Particles in the simulation has Gaussian interaction with the parameters defined in the text and $h_X = -2$. In the beginning, non-affine forces are determined from the projection matrix P defined for kagome lattice. At latter time t, the projection matrix was switched from one lattice symmetry to the other. **a.** Typical configurations of stable lattices at different times. **b.** Plot of global non-affinty parameter X as a function of time. Signature of this switching is present in the peak values of X. Our simulations shows that complex lattice can be stabilised and the symmetry of the lattice can be changed at will. Note that at each switching of the projection matrix P, the density of the lattice has been reduced by increasing the size of the simulation box. This is done in order to avoid kinetically arrested states.

5.2.3 Complex open lattices

We now indicate how our procedure may be generalised in a straight forward manner to periodic crystalline structures of greater complexity. These lattices are "open" in the sense that their packing density is much lower than the "close-packing" density for the dimensionality considered and are usually metastable or unstable. The only close packed structure in 2d is the triangular lattice, while in three dimensions (3d), there are a large number of ordered close packed structures possible which are obtained by stacking 2d triangular planes in specific sequences. The face-centered cubic and hexagonal close backed lattices being the most common ones [1, 2]. Open lattices may be of two kinds. Firstly they may be sparsely coordinated primitive lattices. Maxwell's condition for stability [76, 83] requires that the coordination number, z must be strictly $> 2 \times d$, which amounts to $z > 4$ in 2d and $z > 6$ in 3d. The square lattice in 2d and the simple cubic lattice in 3d are marginal having 4 and 6 nearest neighbours respectively. Including the second coordination shell while constructing the coarse graining volume

Ω is essential in these cases. This ensures that phonon modes which are soft, such as the shear modes encountered in the 2d square lattice, involves particles within Ω. These modes need to be suppressed in order to to ensure stability of the lattice.

Open lattices may also result from decorating a primitive lattice with a basis i.e. a motif consisting of more than one inequivalent particles. For example, in 2d one has the planar honeycomb lattice where a dimer replaces every site of the triangular lattice [31]. Similarly, in the Kagome lattice, the equivalent motif contains five particles arranged as a pair of equilateral triangles, which share a vertex [83]. In 3d, the diamond cubic structure contains repeated vertex sharing tetrahedra.

Such lattices also contain "floppy" modes which involve relative twists of the basis with respect to the rest of the particles in the structure [7, 83]. In the planar honeycomb structure localised modes representing a twist of the dimer results in the creation of a Stone-Wales defect [7]. The coarse graining volume needs to be large enough to be able to describe such modes and Ω needs to contain all symmetry dictated particles belonging to copies of the basis, centred on each site of the primitive lattice. The single parameter h_X may then be used to suppress these modes. In this case therefore, our formulae for the relative displacement $\mathbf{\Delta}$ and projection P matrices need to be constructed accordingly and is discussed in Chapter 2.

Once a suitable Ω is chosen, N_Ω, R and P are known and the feedback loop can be implemented exactly as discussed earlier. Fig 5.5 shows the configurations of stabilised complex lattices obtained by minimising non-affine displacements. We also show that by switching the projection matrix P, during the simulation, is sufficient to change the symmetry of the lattice. As the complexity of the lattices increase, the calculation of the forces becomes more involved but always scale linearly with N_Ω. Real time feedback is therefore still limited by the response time of the optical system and not computation.

5.2.4 Stabilisation mechanism

We begin by commenting on the mechanism by which the S_T structure is stabilised. Consider the two crystal lattices the target, S_T, and the equilibrium structure that the solid prefers without h_X, viz. S_E. The lowest energy path from S_T to S_E (a) may involve non-affine displacements of particles within Ω, or "atomic shuffles" or (b) may be purely affine as is the case of structures connected by a group-subgroup relation [115]. Possibility (a) is easy to analyse since, in this case, the term involving h_X in Eq.(5.1) increases the energy of S_E relative to S_T stabilising the latter; any small fluctuation taking $S_T \rightarrow S_E$ *always* cost energy. Possibility (b) is more subtle.

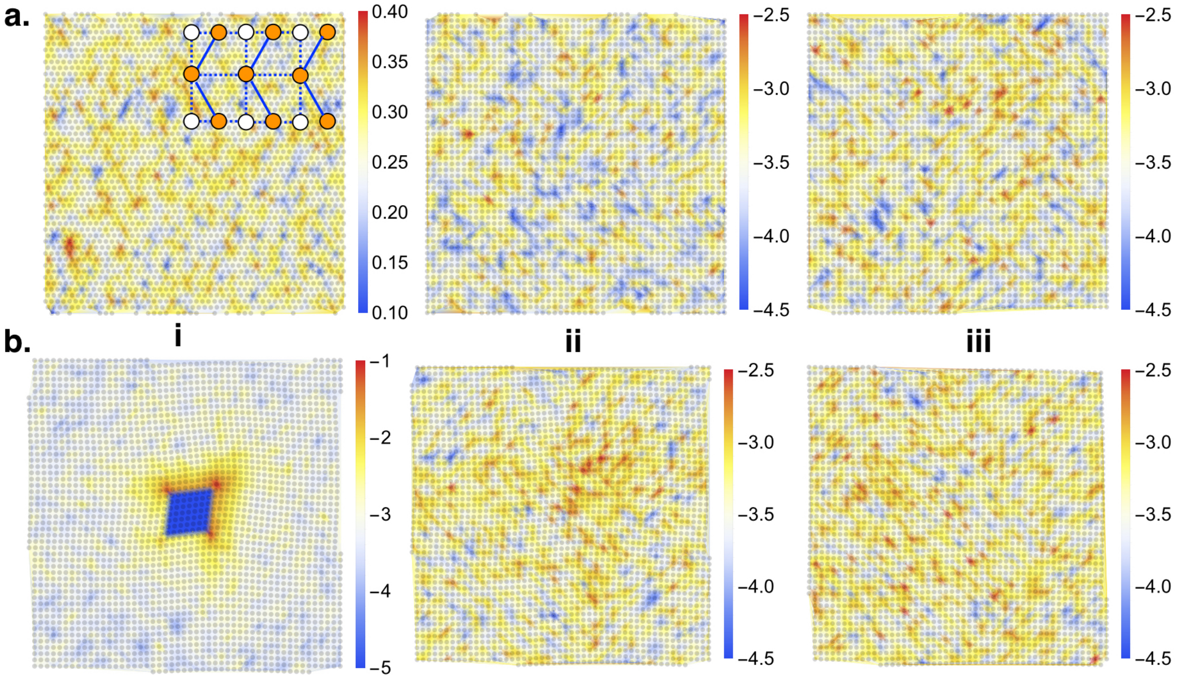

Fig. 5.6. Configurations showing the recovery of the square lattice after an initial distortion: **a.** The square lattice of 2500 GCM particles at $\rho = 0.5$ and $T = 1 \times 10^{-3}$ was distorted by displacing alternate rows of particles by half a lattice spacing (see schematic inset) producing a triangular lattice close to the S_E structure (**i**). Under a stabilising field of $h_X = -2.0$ the target lattice quickly recovers as seen in **ii** (4.8×10^4 MCS) and **iii** (24×10^4 MCS). **b.** Here we produce a patch of triangular lattice within a square matrix (**i**) and again let the solid recover the square structure: (**ii** and **iii** as above) under the influence of the same field as in **a**. The particles are coloured according to the value of the local χ values.

For example, both square and triangular crystals may be considered as special cases of a general *oblique* lattice and one can be obtained from the other by a purely affine transformation. Along this transformation path, which involves a bulk homogeneous strain, therefore, h_X will *not* contribute. However, such an event is statistically unlikely except for extremely small systems. What is more likely is that a small patch of particles locally transforms to the S_E structure creating χ at the interface. Within classical nucleation theory [1] the free energy cost of such a patch of size L_p is $\mathcal{F}_p = A\Delta\mathcal{F}L_p^2 + Bh_X L_p$, where we ignore interfacial terms independent of h_X. Here $\Delta\mathcal{F}$ is the bulk free energy difference per unit area between the two lattices and A, B are constants. This patch is stable only if it is larger than a critical size $L_p^* \sim -h_X/\Delta\mathcal{F}$ and costs interfacial energy $\sim h_X^2/\Delta\mathcal{F}$. L_p^* can be large if $\Delta\mathcal{F}$ is small and can be made even larger by tuning h_X. If $L_p^* > L$, again, a finite S_T crystal will be stable due to *the inability of the system to create a sufficiently low energy $S_E|S_T$ interface*.

It is possible to demonstrate both these mechanisms for the square to triangular transition. It is known that a mechanically unstable square lattice may decay, at nonzero temperatures into the stable triangular structure in many different ways [110]. For example, (a) alternate rows of particles in the square lattice may shift by half a lattice spacing hence producing a distorted triangular lattice which subsequently equilibrates. On the other hand a patch of particles inside the square matrix may undergo a distortion to the triangular structure (b). Our stabilisation strategy should be able to recover the target square lattice S_T from both (a & b) of these distortions.

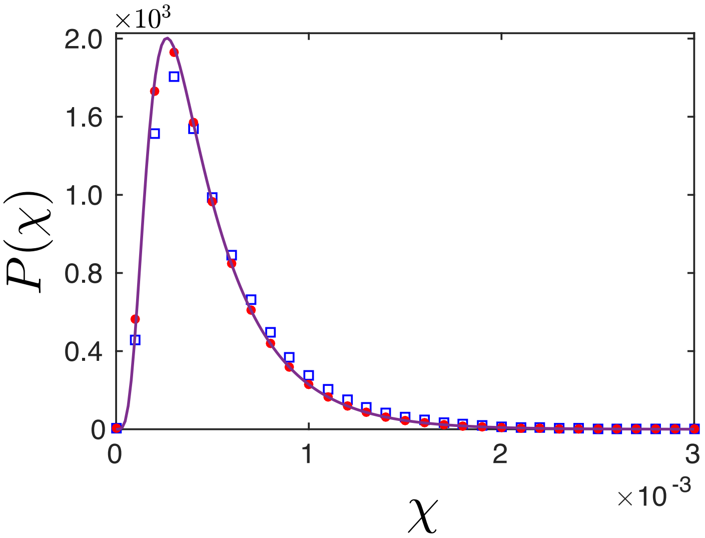

Fig. 5.7. The resulting $P(\chi)$ at the end of runs Fig. 5.6**a** (red circles) and Fig. 5.6**b** (blue squares), the solid line is the harmonic theory prediction [7].

In Figs. 5.6**a** and **b** we demonstrate this explicitly by starting from initial (square) configurations of a $N = 2500$ GCM solid incorporating these two kinds of distortions (a) and (b) and equilibrating with $h_X = -2.0$, where the square lattice is stable. In the first case (Fig. 5.6**a**), the local shuffles of particles cost energy and are quickly removed from the solid. In the second case, (Fig. 5.6**b (i)**) we first create a large patch of particles with local triangular order using an inhomogeneous affine strain. Next, we equilibrate the surrounding matrix keeping the particles within the patch immobile. This produces a mechanically relaxed (but high energy with large local χ) interface between a square solid and a triangular inclusion. The constraint is then removed and the whole system equilibrated. Fig. 5.6**b (iii)** shows that the sub-critical patch thus created disappears. As a check (Fig. 5.7) we ensure that $P(\chi)$ obtained from the equilibrated configurations again match theoretical predictions [5, 7].

In 2d, long wavelength displacement fluctuations are known to destroy crystalline order [1] and therefore a discussion of this effect is germane for the 2d square solid discussed here. Crystals in 2d posses only "quasi", rather than true, long ranged order since the mean squared displacement $\langle u^2 \rangle$ diverges as $\log L$. This is an effect of dimensionality and appears in the thermodynamic limit for any 2d crystal; even those with non-pathological phonon spectra. These fluctuations have also recently been observed even for amorphous solids [116–118] considerably increasing the scope of its general applicability. How do these fluctuations affect our results?

Our proposal is designed to stabilise *finite* sized crystals. Indeed, for any $|h_X|$, as the system size L is increased, one reaches a threshold above which the solid is no longer stable (see Fig. 5.3**b**). In order to stabilise larger systems, $|h_X|$ has to be increased as $\sim L^2 = N$. To obtain stable solids with large L requires large, and probably experimentally un-realisable, optical field strengths. The weak logarithmic divergence of displacements discussed above is therefore unobservable at the system sizes obtainable with any realistic $|h_X|$ and does not alter our results.

5.2.5 Experimental realisation of the stabilisation procedure

We now comment briefly on the foreseeable technical challenges which may need to be overcome to implement our proposal in the laboratory. Colloidal particles have sizes in the range 1nm to a few μm, with the larger sized particles being easier to trap and manipulate [11]. For colloids at the larger end of the size range, typical timescales are of the order of a second [54]. These particles need to be tracked in real time, forces calculated and applied using laser traps.

Particle tracking at frame rates of 10 kHz are possible using current technology [119] so this is not a rate limiting steps. Since the computations needed to calculate forces even for the most complex lattices are simple these are also quite fast. The crucial experimental step therefore is the deployment of the traps to generate forces.

For this purpose one may use spatial light modulator and holographic tweezer technology [109] which produce a reconfigurable optical surface based on inputs. Typical spatial resolutions of these devices are about $1-3$ μm which is appropriate for our purpose. The input frame rate can theoretically go from 500 upto 1 kHz, although actual frame rates can be much slower. In any case, considering that large colloids are slow, one has a reasonable margin of exploration.

Are the values of h_X for reasonably sized lattices too high to be realised in the lab? Quantitative estimate of the energy due to the h_X term shows that it is comparable to the energy of interactions which is of the order of a few k_BT. This is the regime where all previous optical manipulations of colloidal crystals have been traditionally performed [57, 105, 106]. However, spatial light modulators also decrease light intensity which depends on the make of the device; so higher laser powers are needed limiting the number of particles which may be trapped without causing excessive heating. An alternative procedure is to use time shared traps [120] in a dense enough array fixed in space with their intensities modified intermittently to approximate the optical potential surface.

Feedback controlled traps of a somewhat different nature has already been employed to study crystallisation of colloids [121]. The principle behind this implementation is quite different from ours. Instead of coupling to a local configuration dependent parameter such as χ, the trap responds to a global order parameter for crystallisation. The symmetry of the crystal is still determined by the inter-particle interactions and very limited control over crystal structure is possible.

5.3 Summary and conclusion

In conclusion, we present a proposal for producing crystalline templates for colloidal particles using dynamic, feedback controlled, laser traps. These templates are reconfigurable and can, in principle, stabilise any structure in any dimension. Unlike static templates, our method does not merely provide a restoring force to the target structure. All possible affine fluctuations about S_T are allowed, preserving all symmetries of the crystal. Only non-affine excursions away from S_T are *selectively* suppressed.

One may view the stabilising forces that we use as originating from an effective three-body potential viz, Eq. (5.1). The form of this potential depends on the reference configuration guaranteeing that these forces necessarily stabilise the target structure. Our method therefore *automatically* determines the potential which stabilises S_T. The advantage of our method is that no further assumption about particle interactions is necessary. While it may be possible, for the case of simple target structures, to guess interactions which give rise to them and perhaps design colloids which produce these structures [100], this becomes progressively difficult as the complexity of S_T increases. This is especially important when we realise that using a similar strategy even inhomogeneous structures such as surfaces and interfaces of any specified orientation as well as random glassy configurations may be stabilised.

Finally, we emphasise again that fast particle tracking and realisation of fast response times of light fields required for our method to work is feasible for colloidal solids because of their slow time scales. Similarly heating problems associated with these light fields should also be minimal especially since the magnitude of forces needed are small ($\ll k_BT$). Of course, only actual experiments can finally decide upon the feasibility of our proposal. We hope that our work motivates experimental work in this direction in the near future.

In the next chapter we show that the same principle involved in stabilising colloidal crystals as discussed in this chapter may be used for stabilising any given pattern in a swarm of active, autonomous vehicles such as drones and bots.

6

Stabilizing order in robotic swarms

6.1 Introduction

In the earlier chapters of this thesis we described how fluctuations of particles arranged in a particular order or pattern, defined by a set of reference coordinates $\{\mathbf{R}_i\}$, may be analyzed in terms of affine and non-affine components and the pattern stabilized by suppressing the latter. Our interest, so far, were limited to atomic and colloidal crystals where these particles were at least smaller than microns and were in thermodynamic equilibrium. Further, these particles were incapable of self-propulsion and responded mainly to thermal fluctuations and inter-particle interactions. In this chapter, we shall generalise our study to include a very different class of systems and immersed in non-equilibrium background environment. First, the particulate entity that needs to be ordered will typically be of macroscopic dimensions upwards of a few centimeters at least. Secondly, these entities will have a means of self-propulsion and would be able to communicate to each other. Finally, thermal fluctuations will be irrelevant in the length and time scales that we will be typically interested in. In this chapter we apply our methods as developed in the earlier chapters to stabilize patterns in swarms or flocks of autonomous, self-propelled, robots which either walk, or swim or fly in some medium. To be specific, we will study flocks of drones in a turbulent fluid.

Coordinated and collective behaviour of animals is readily seen in nature over a huge range of length scales from meters and kilometers to microns, in the case of bacterial swarms [18, 70, 71, 122–124]. Flocks of birds or school of fishes naturally organise themselves into ordered swarms against the destabilisation tendency of random turbulent noise. However, self propelled particles capable of flocking have been realized in labs [19, 125, 126]. Such active particles have demonstrated that flocking is not the result of active decision making but can arise spontaneously due to the presence of short and long range inter-particle interactions [16, 17, 127].

Many hydrodynamic models linking this spontaneous emergence of order to conservation laws and symmetry breaking have been introduced [127–130]. However, the simplest way to model flocking was formulated by Vicsek [16, 17]. The algorithm involves active particles moving with constant speed capable of aligning their velocity vector with the neighbours within some error. Despite the short range interactions and rotationally invariant dynamics of Vicsek model, spontaneous long range orientational order is observed by breaking the rotational symmetry of the system. Unlike equilibrium systems, spontaneous emergence of long range order is due to the fact that Vicsek model is inherently a non-equilibrium system with constant input of energy. While the spontaneous ordering of active particles have been shown in models like Vicsek, such large sized ordered flocks are found to be unstable in the presence of turbulent-like flow field [131, 132]. Furthermore, even though the long range orientational order is observed, positional order is not maintained.

Such positional order of active particles, however, may be required for many practical purposes. Patterns of drones or robotic agents or “bots” are useful for many purposes such as surveying unknown territory, taking measurements of scientifically or economically important quantities over a large area, pollinating, decontaminating, harvesting, or simply featuring in purely decorative drone shows [133, 134]. These agents may be deployed in air, water, land or in space. In many of these uses having the agents arranged in a specific pattern which may or may not vary in time is useful. Disruption of the pattern may occur due to many factors for e.g. atmospheric or ocean turbulence. Typical strategies for maintaining patterns in swarms may involve accurate measurement of the velocity of the fluid medium and compensating for the disruptive forces at the level of individual bots using computations performed at a central command and control station. Stabilising any given pattern in such a swarm is therefore energy expensive and requires extensive computation and communication overheads. These issues have prevented extensive use of large drone swarms, which tend to be relatively small, restricted over small spatial extents and operated in calm weather.

In this chapter we show that suppressing non-affine displacements away from the given reference pattern while allowing affine deformations such as translations, rotations etc. using a virtual non-affine field h_X solves many of these problems. Unlike, colloids, where we proposed dynamic, feed-back controlled laser traps for providing h_X, here it is provided by controlling the thrust vectors of the robots. The instantaneous local neighborhood of a drone within a swarm is used to compute these thrust vectors by comparing it with a desired reference residing in the memory of each drone. We show that the energy, or power, expended in the steady state fluctuates around zero. Finally, we show that under certain conditions, spatial correlations of the magnitude of the thrust mimics velocity correlations of the, possibly turbulent, fluid medium. In such cases, velocity structure factors of the turbulent fluid can be measured [135] *without measuring the velocity*! There are no restrictions of the length scales in such measure-

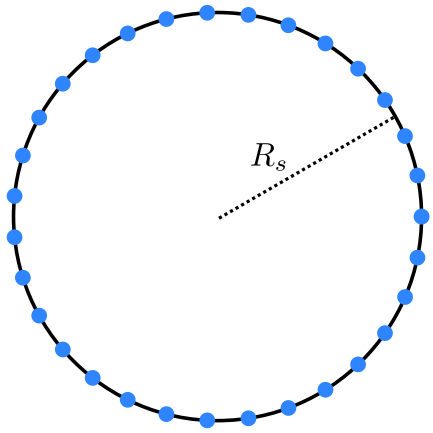

Fig. 6.1. Schematic of a swarm of bots (blue dots) the solid black lines joining the bots are a guide to the eye.

ments, making these ideal systems to deploy for studying atmospheric turbulence over kilometers.

The rest of this chapter is arranged as follows. In the next section 6.2, we discuss simplified models for swarms and the flow field. This is followed by section 6.3, where we begin our investigation for each model. We present our results for several quantities. In section 6.4, we summarize our results and critically comparing them for different models. Finally, we end the discussion by briefly commenting on the real word implications and feasibility of our stabilization algorithm.

6.2 A robotic swarm in a turbulent flow

Unlike atomic and colloidal solids where thermodynamics determines an *equilibrium* structure, there is no such restriction for robotic swarms, which can exists in any order or pattern desired by us. Indeed, swarms of airborne *drones* are routinely used for decorative drone-shows [133, 134]. To avoid unnecessary computational complexity however we assume, in what follows, a very simple structure for our swarm. We emphasize, however, that the principles described in this chapter apply to swarms of any shape and size without restriction.

Consider, therefore a system of bots placed at equal intervals on a ring of radius R_s (see Fig. 6.1). The particles are considered to be point like, have mass m and are allowed to move within a $2d$ square simulation box of length $L >> R_s$. Note that we show computations for a fully two dimensional swarm - a ring immersed in a $2d$ flow. Our method works equally well in any dimension as should be obvious from the work presented in the earlier chapters of this thesis. Extension to $3d$ is therefore feasible but at the cost of computational complexity.

At any time step t, due to the presence of a background flow field, the position $\mathbf{r}_i$ and velocity $\mathbf{v}_i$ of i^{th} particle is determined by the set of Stokes-drag or Langevin dynamics (LD) equations with a constant drag coefficient γ.

$$\frac{d\mathbf{r}_i}{dt} = \mathbf{v}_i\,, \tag{6.1}$$

$$m\frac{d\mathbf{v}_i}{dt} = -\gamma\left(\mathbf{v}_i - \mathbf{U}(\mathbf{r}_i, t)\right) + \mathcal{F}_i\,, \tag{6.2}$$

where $\mathbf{U}(\mathbf{r}_i, t)$ is the background spatio-temporal flow field measured at the particles' position $\mathbf{r}_i$ and time t. Note that, we do not take into account any reverse affect of the particles on the flow field. In other words, the system is under the constraints of dry hydrodynamics and lacks Galilean invariance. The particles, i.e. bots or drones, are *active* and capable of self propulsion. In the above outlined equation, $\mathcal{F}_i$ represents such active forces or thrusts produced by the bots' own propulsion system. A careful choice of active forces can stabilize the pattern against the turbulent flow. To show this we examine three different models of active forces discussed in Sec 6.2.2. Before we do that we need to specify the flow field used in our study. We do this below.

6.2.1 Modelling the flow field

In practice, our robotic agent will experience real turbulent flow obeying the Navier-Stoke's equations. However, for our proof of principle, an accurate solution to these equations is unnecessary. We use, therefore, a synthetic, multi-scale, spatio-temporally correlated turbulent-like flow field.

To model the velocity field we follow the method described in [136–138] i.e. the velocity of the field $\mathbf{U}(\mathbf{r}, t)$ at any given position and time is obtained from the Fourier series,

$$\mathbf{U}(\mathbf{r}, t) = V_0 \sum_{n=1}^{N_k} \Big[\mathbf{A}_n \cos(\mathbf{k}_n \cdot \mathbf{r} + \omega_n t) + \mathbf{B}_n \sin(\mathbf{k}_n \cdot \mathbf{r} + \omega_n t)\Big]. \tag{6.3}$$

Here N_k is the total number of Fourier modes included and V_0 is a dimensionless constant which determines the strength of the field. Although, $\mathbf{U}(\mathbf{r}, t)$ in the above equation is not a solution of Naiver-Stokes equation, the Fourier coefficients $\mathbf{A}_n$, $\mathbf{B}_n$ and distribution of modes $\mathbf{k}_n$, ω_n are chosen such that the velocity field produced is in-compressible and the energy spectrum follows Kolmogorov scaling $k^{-5/3}$. Therefore, for a $2d$ flow field, we take

$$\begin{aligned} \mathbf{A}_n &= a_n(\cos(\phi_n), -\sin(\phi_n)) \\ \mathbf{B}_n &= b_n(-\cos(\phi_n), \sin(\phi_n)) \\ \mathbf{k}_n &= k_n(\sin(\phi_n), \cos(\phi_n)), \end{aligned} \tag{6.4}$$

with phases ϕ_n chosen randomly from a uniform distribution between $[0, 2\pi)$. The choice of phases remains constant for all time but is different for different ensemble/realization of the field. Evidently, with the above choice of Fourier coefficients, we have $\mathbf{A_n} \cdot \mathbf{k_n} = \mathbf{B_n} \cdot \mathbf{k_n} = 0$ resulting an in-compressible field for any choice of ϕ_n,

$$\nabla_\mathbf{r} \cdot \mathbf{U}(\mathbf{r}, \mathbf{t}) = 0\,.$$

The magnitudes a_n and b_n in Eq. (6.4) are

$$|a_n|^2 = |b_n|^2 = E(k_n)\Delta k_n. \tag{6.5}$$

such that $E(k)$ is the energy spectra of the form $Ck^{-5/3}$ in the range $(k_1 = \frac{2\pi}{\zeta}) \leq k \leq (k_{N_k} = \frac{2\pi}{\eta})$ and zero otherwise. Where, ζ and η corresponds to largest and smallest length scale respectively. For a discrete set of k_n, Δk_n are defined as,

$$\Delta k_n = \begin{cases} (k_{n+1} - k_{n-1})/2 & , \quad 2 \leq \mathrm{n} \leq \mathrm{N_k} - 1 \\ (k_2 - k_1)/2 & , \quad \mathrm{n} = 1 \\ (k_{N_k} - k_{N_k - 1})/2 & , \quad \mathrm{n} = \mathrm{N_k} \end{cases} \tag{6.6}$$

with the wave-vector amplitudes k_n obeying any one of the following distributions.

$$k_n = \begin{cases} k_1 n^\alpha & \text{algebraic,} \\ k_1 \alpha^{n-1} & \text{geometric,} \\ n k_1 & \text{linear.} \end{cases} \tag{6.7}$$

and $n = 1, 2, 3...N_k$. Value of α for the above distributions is obtained by setting k_1 and k_{N_k} equal to $2\pi/\zeta$ and $2\pi/\eta$, thus

$$\alpha = \frac{\ln(\zeta/\eta)}{\ln(N_k)} \quad \text{for algebriac,}$$

$$\alpha = (\zeta/\eta)^{1/N_{k-1}} \quad \text{for geometric.}$$

Additionally, the frequencies ω_n determines the unsteadiness of the field and is proportional to the eddy turn over time, $\omega_n = \lambda\sqrt{k_n^3 E(k_n)}$, with λ as a dimensionless constant of order 1.

In our analysis, we choose linear distribution of wave-modes with $C = 0.5$. However, any other choice of mode distribution do not affect our results. We also set ζ equal to the length of the simulation box L with a total of $N_k = 500$ modes. For each realisation of the flow field (choice of ϕ), λ is reset at every twentieth time step of our LD simulation to a value chosen from Gaussian distribution of mean 1 and standard deviation 0.25.

6.2.2 Modelling active forces

Study of a spring-mass like system immersed in a turbulent flow field has given us much insights [139–143]. Such studies have shown, a spring-mass chain system can preferentially sample the vortex flow. Different motions of the spring-mass chain, such as different regimes of "flapping" motions can yield valuable information about the flow field itself such as the scaling of the velocity structure function, energy flux of the turbulent fluid, characteristic times of eddies etc [144–146]. Therefore, it is natural to ask about the stability of the system of particles, if the active forces are of harmonic in nature. Is a swarm, where virtual harmonic interactions are assumed within drones capable, in general, of maintaining it shape? To investigate, we consider our model swarm in the shape of a ring of particles with forces given by,

$$\mathcal{F}_i^\alpha = -K\sum_j (|\mathbf{r}_{ij}| - |\mathbf{R}_{ij}|)\frac{r_{ij}^\alpha}{|\mathbf{r}_{ij}|}, \tag{6.8}$$

where sum over j is extended over the neighbours of i and α represents the spatial coordinate.

Although, harmonic forces used above are translationally invariant and depends only on the positions of neighbours, we note that such system when immersed in turbulent flow do not maintain its pattern regardless the value of stiffness k. Time evolution

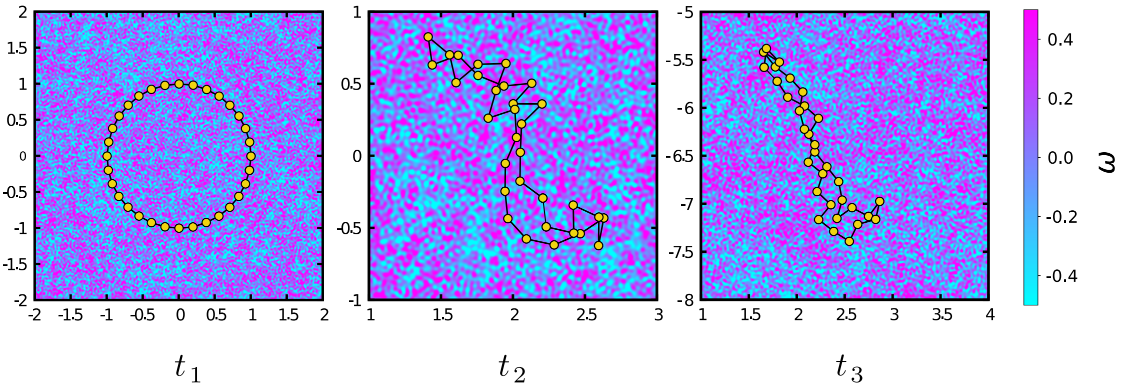

Fig. 6.2. Typical time evolution ($t_1 < t_2 < t_3$) of the ring in the presence of turbulent field and active harmonic forces. Configurations obtained are for turbulent field strength $V_0 = 1.1$ and force stiffness $K = 500$. Background color represents the vorticity values of the turbulent field. Time t_1 show the initial configuration of the system. Clearly, the ring pattern of active particles is not stable if harmonic interactions are considered. Black solid lines are for visual guidance.

in Fig 6.2 shows deformation of the ring into an entangled state. Further, large time simulation shows no recovery from this intertwined state of the ring.

Particle displacements observed in the case of harmonic active forces show the existence of zero energy collapse modes [83]. Though, the connectivity between the neighbours is preserved due to the harmonic bonds, the swarm can deform without any energy cost. Such deformations can be avoided by making use of more complicated interactions between particles. One approach is to include more connections between neighbors until the Maxwells criterion for rigidity is met [76]. This requires information of distant neighbours and cause communication overheads. Clearly, simple two-body interactions are not enough and the one requires three-body forces or forces that prefer particular bond angles as used in, say, Chapter 3 (honeycomb case Sec 3.1.3). Even in the presence of such interactions, the desired pattern may not be the unique ground state [147]. In addition, formulating such harmonic interactions can be cumbersome for more complex patterns.

Throughout this chapter, we explain how to achieve this and stabilize a given pattern in a swarm with the desired target configuration being the unique ground state of the system. Our algorithm is similar to that used for colloids in Chapter 5, although we do not need external traps to generate the necessary forces. As discussed in Chapter 2, any set of particle displacements can be projected onto affine and non-affine subspace. The non-affine part of the displacements, in contrast to affine, involves particle rearrangements and change the local connectivity of the neighborhood (Chapter 2). We have also shown in Chapter 5 that a system of colloidal particles in thermal equilibrium can be stabilized into any desired lattice symmetry if it is only possible to suppress non-affine displacements [35]. The stabilization procedure proposed does not require the specifics of inter-particle interaction or noise but the information of the desired reference structure. Since, minimising non-affine displacements away from a reference configuration is essentially a linear optimization problem, therefore, the desired reference structure being the unique ground state is guaranteed.

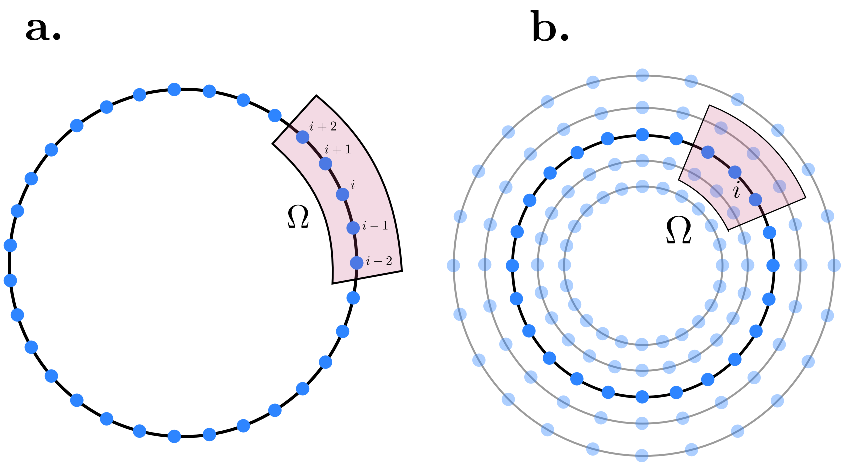

Fig. 6.3. Reference structure and coarse-graining volume Ω. **a.** Model A : Floppy Swarm, Active particle spaced equally on a ring. Around particle i coarse-graining volume (pink shaded) is defined and consists two left and right neighbours. **b.** Model B : Rigid Swarm, Active particles equally spaced on a ring (dark blue) surrounded by layer of concentric ghost particles (light blue). Coarse-graining volume (pink shaded) around particle i consists of total 8 particles.

We borrow this idea of selectively suppressing non-affine displacements while simultaneously allowing affine transformations for our active forces. While detailed discussions of the projection formalism are given in the previous chapters of this thesis, we briefly recall below the main ideas relevant to the context of the present study.

For any desired pattern, which we wish to stabilise such as ring, the reference configuration of each tagged particle $\mathbf{R}_i$ remains in the memory of robotic agents. We study two different models namely “Model A : Floppy swarm” and “Model B : Rigid swarm”, see Fig 6.3. For both the models, around each particle i, a coarse-grained region $\Omega(i)$ consisting the ids of neighbours of i^{th} particle is defined. As discussed in Chapter 2, in d dimension for a given coarse-graining volume consisting N_Ω number of particles there exist $N_\Omega d - d^2$ non-affine modes. Therefore for our $2d$ system, Ω should always consist of more than two neighbour particles in order to have non-affine displacements. In other words, any motion of two particles in $2d$ is always affine.

In Model A we use a coarse-graining volume Ω consisting of five particles viz. two left and right neighbours of the central particle. On the other hand, in model-B active particle are sandwiched between concentric layers of “ghost” particles. The ghost particles are imaginary particles with only the spatial coordinates stored in the memory of the actual drones. The purpose of the ghost particles is to provide a reference structure for the non-affine projection formalism. Further, ghost particles do not interact with background flow field and are free to translate and rotate along with the center of mass of the actual flocks. Coarse-graining volume for model-B thus consist of total $8+1$ particles as shown in Fig 6.3.

For a pure affine deformation of Ω, a deformation matrix $\mathcal{D}$ can be written such that $\mathbf{u}_j - \mathbf{u}_i = \mathcal{D}_i(\mathbf{R}_j - \mathbf{R}_i)$. On the other hand, a generic set of particle displacements contains contribution from both affine and non-affine. In such cases a local deformation tensor $\mathcal{D}$ is defined as the one which minimises

$$\chi_i = \min_{\mathcal{D}} \sum_{j\in\Omega(i)} \left[\mathbf{u}_j - \mathbf{u}_i - \mathcal{D}_i(\mathbf{R}_j - \mathbf{R}_i)\right]^2, \tag{6.9}$$

the sum over index j extends to all particles contained in coarse-graining volume Ω around particle i. Upon following the procedure described in Chapter 2 and 5, the active forces for the swarm can be defined as follows.

$$\mathcal{F}_i = -\frac{\partial(-h_X N X)}{\partial \mathbf{r}_i} \tag{6.10}$$

In the above equation, N is the total number of active flocks and h_X determines the strength of non-affine active forces conjugate to global non-affinity parameter

$$X = \frac{1}{N}\sum_i \chi_i \tag{6.11}$$

Using Eq. (6.10), force in direction α on particle i can be written explicitly as

$$\mathcal{F}_i^\alpha = -2h_X \sum_{j\in\Omega(i)} \left[2u_{ij}^\alpha - \left(\mathcal{D}_i^{\alpha 1} + \mathcal{D}_j^{\alpha 1}\right) R_{ij}^1 - \left(\mathcal{D}_i^{\alpha 2} + \mathcal{D}_j^{\alpha 2}\right) R_{ij}^2\right]. \tag{6.12}$$

Here $\mathcal{D}_i$ is the best fit deformation matrix whose elements are given by,

$$\begin{aligned} \mathcal{D}_i^{\mu\nu} &= \sum_{j\in\Omega(i)} u_{ij}^\mu \left(R_{ij}^1(\Upsilon_j^{-1})^{\nu 1} + R_{ij}^2(\Upsilon_j^{-1})^{\nu 2}\right) \\ (\Upsilon_j)^{\mu\nu} &= \sum_{i\in\Omega(i)} R_{ij}^\nu R_{ij}^\mu \end{aligned} \tag{6.13}$$

Note that the above expression for the force, as usual, preserves translational invariance. Although the force expression outlined in above is true for both Model-A and B, the numerical value is different due to the sum over different coarse-grained regions and reference structures. Unlike the colloid case studied in Chapter 5, there are no other "inter-particle" forces. Of course, when two bots come very close to each other, they may collide. This eventuality has not been considered by us here but collision avoidance may easily be incorporated if needed.

6.3 Results

Once our model for active non-affine forces is setup, we are in position to start our investigation. The equations of motion Eq. (6.2) in Sec. 6.2 in the presence of flow field are integrated numerically using a Verlet type algorithm as prescribed in [148].

$$\begin{aligned}\mathbf{r}_i(t_{n+1}) &= \mathbf{r}_i(t_n) + gdt\mathbf{v}_i(t_n) + \frac{gdt^2}{2m}\mathbf{f}_i(t_n) \\ \mathbf{v}_i(t_{n+1}) &= h\mathbf{v}_i(t_n) + \frac{dt}{2m}\left(h\mathbf{f}_i(t_n) + \mathbf{f}_i(t_{n+1})\right)\end{aligned} \tag{6.14}$$

where,

$$g \equiv \frac{1}{1+\frac{\gamma dt}{2m}}; \qquad h \equiv \frac{1-\frac{\gamma dt}{2m}}{1+\frac{\gamma dt}{2m}}$$

Thus the particles' position $\{\mathbf{r}(t_{n+1})\}$ and velocities $\{\mathbf{v}(t_{n+1})\}$ at time t_{n+1} are computed from those at the earlier time ($t_n = t_{n+1} - dt$). Besides that, at each time particle position and velocities are also influenced by non-affine forces (Eq. (6.12)) and the background turbulent field. Therefore in Eq. (6.14), $\mathbf{f}_i(t_n)$ is the total force and is given by the sum $\gamma\mathbf{U}(\mathbf{r}_i(t_n), t_n) + \mathcal{F}_i(\{\mathbf{r}(t_n)\})$.

For our simulation, without loss of generality, we choose $m = \gamma = 1$ with the integration time step as $dt = 0.001$ units. We check the robustness of our stabilisation algorithm using the collective scalar variable X (Eq. (6.11)) averaged over different realisation of the flow field. Variation of X for different values of the strength of non-affine forces h_X and turbulent field V_0 has been studied. Lower the values of X corresponds to more stable patterned structure.

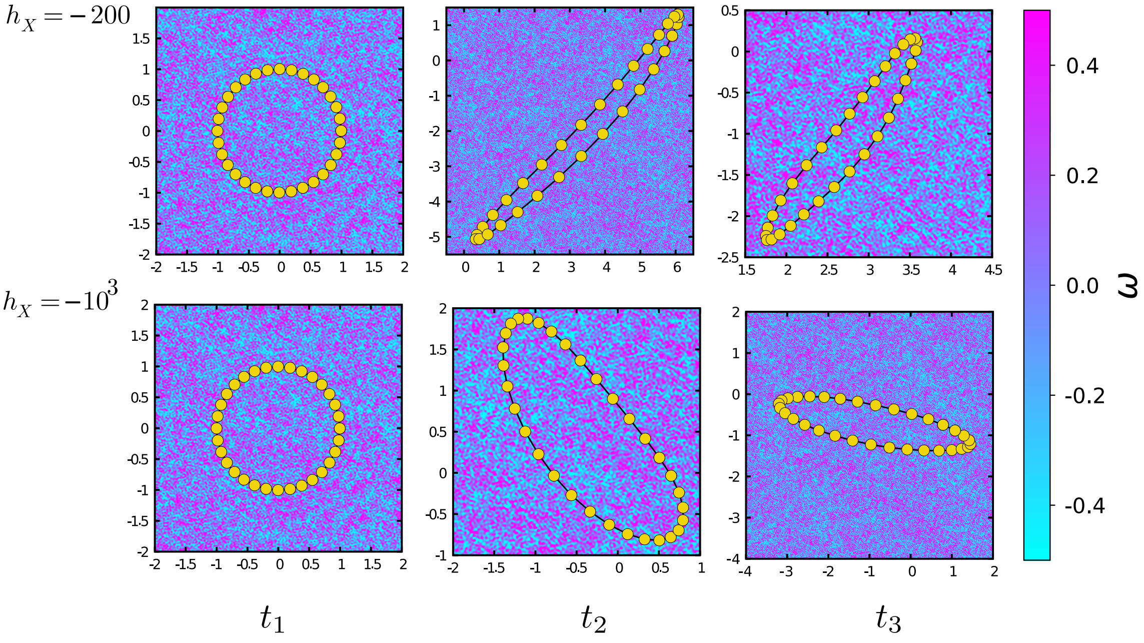

Fig. 6.4. Model A: Time evolution ($t_1 < t_2 < t_3$) of model-A for different strength of non-affine force $h_X = -200, -1000$ and $V_0 = 1.1$. Background color represents the vorticity values of the turbulent field. Clearly, transformations of the circular ring to elliptical shapes are allowed and cost no energy because these shapes are related to the reference circle by an affine transformation. Solid black lines are for visual guidance.

6.3.1 Model A: Floppy swarm

We collect and analyse the simulation data when X reaches a steady state for all realisations of flow field. Our results for the Model A ring reveals a stable elliptical pattern for sufficiently high values of h_X. On the other hand, at low strength of non-affine forces h_X, the ellipse may intertwine with itself occasionally. It is interesting to note that, in this case, since such an intertwined ellipse is essentially a non-affine deformation it relaxes back as time progresses in sharp contrast to the purely harmonic ring. Furthermore, highly elliptical configurations are often observed. The transformation that takes a circle to an ellipse is affine such as a shear or uni-axial strain. Such deformations, no matter how large, do not produce any non-affinity in the system and hence are not resisted by the active forces. However, in each case, we note that the local neighbourhood connectivity between particles is preserved.

At steady state, one can now also look at the variation of global non-affinity X with respect to strength of flow field V_0 and non-affine forces h_X (see Fig. 6.5). It is quite evident that, non-affine forces are working against the destabilising effects of turbulent flow field. Due to these two competing forces, we show (Fig. 6.5) that $X \sim \frac{V_0^2}{|h_X|}$ i.e. the ratio of the strength of the noise to strength of stiffness forces, which is the only

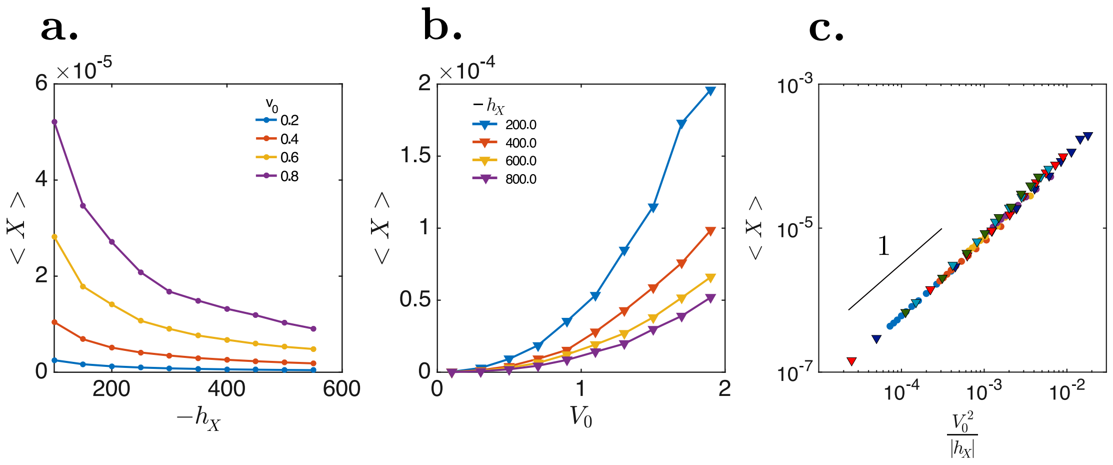

Fig. 6.5. Model A : **a.** Variation of $< X >$ with respect to strength of non-affine forces h_X. A decrease in value of $< X >$ shows the stability of the patterned as strength of non-affine field is increased. **b.** Variation of $< X >$ with respect to strength of non-affine forces V_0. Increase in value of $< X >$ with increase in strength of velocity V_0 indicates the destabilising effect of turbulent flow. **c.** Scaling form, $< X >$ varies linearly with $V_0^2/|h_X|$.

independent dimensionless number possible. For small values of this dimensionless number, the relation is linear.

6.3.2 Model B: Rigid swarm

Although, non-affine forces were able to preserve the local neighbourhood, a perfect ring shaped swarm of robotic agents is not possible and may transform into an ellipse. However, such affine deformations can be avoided if one considers a reference structure that involves ghost layers of particles viz. Model-B. The position of the particles in the ghost layers are not affected by the turbulent field or non-affine forces and remain virtual, stored only the memory of robotic agents. However, the ghost layers are free to translate and rotate with the real active particles. Presence of ghost particles thus serves as a stencil for actual ring and deformations like shear and uni-axial strain are now deemed as non-affine. Only affine transformations which involves pure rotation and translation of the full system as a whole are allowed. For such a system we realise that the affine mode which may take a ring to ellipse can be suppressed as well. Fig. 6.6 shows a typical configuration of a Model-B swarm for different values of V_0 and h_X indicating the stabilisation effect of non-affine forces at a much lower value of non-affine forces. It is interesting to note, the global non-affinity X, for the system with ghost particles also follow the same scaling form of $\langle X \rangle \sim V_0^2/h_X$ (see Fig. 6.7).

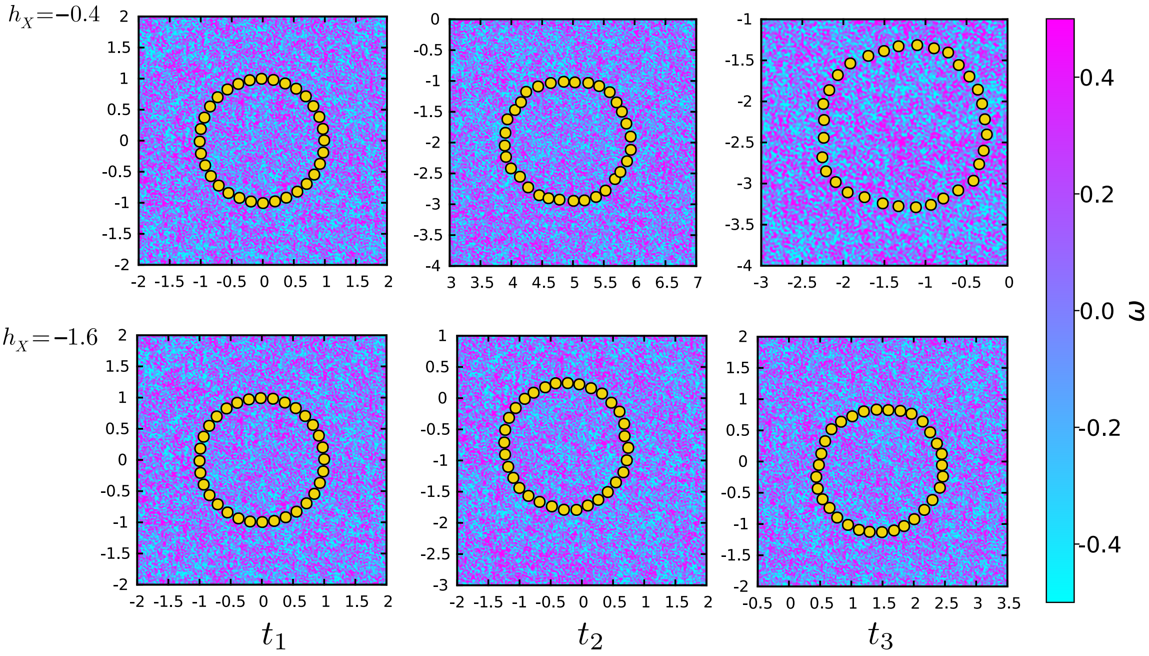

Fig. 6.6. Model B: Time evolution ($t_1 < t_2 < t_3$) of model-A for different strength of non-affine force $h_X = -0.4, -1.6$ and $V_0 = 1.1$. Background color represents the vorticity values of the turbulent field. Clearly, due to presence of ghost particles active particles in a definite ring pattern is stabilized.

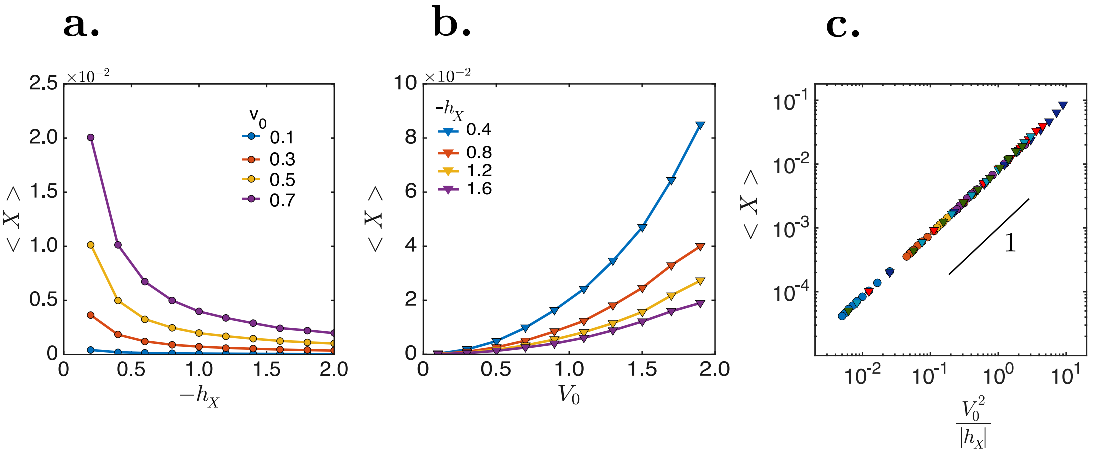

Fig. 6.7. Model B: **a.** Variation of $< X >$ with respect to strength of non-affine forces h_X. A decrease in value of $< X >$ shows the stability of the patterned as strength of non-affine field is increased. **b.** Variation of $< X >$ with respect to strength of non-affine forces V_0. Increase in value of $< X >$ with increase in strength of velocity V_0 indicates the destabilising effect of turbulent flow. **c.** Scaling form, $< X >$ varies linearly with $V_0^2/|h_X|$.

6.4 Summary and conclusion

In this work we have studied the effect of active forces on the stabilisation of a swarm of robotic agents immersed in turbulent flow field. We observed that introducing a simple, harmonic-like interaction among the bots is not sufficient to maintain the structure/pattern of the swarm. However, suppressing non-affine fluctuation of the robotic agents from the desired reference structure can achieve this feat. As active non-affine forces depends only on the instantaneous and reference position, any desired structure of swarm can be stabilised without worrying about the structure of background flow field. Another important finding of our work, worth mentioning, is the energy efficiency of the stabilisation algorithm. Upon ensemble averaging, the global non-affinity X reaches a constant value. Thus the average power spent by non-affine forces to stabilise the pattern is zero for both Models A and B. Of course, drones need a finite amount of power to operate. However, drones are also required to produce an additional thrust against the turbulent field to stabilize the desired pattern. It is this part of the total power, which upon ensemble averaging fluctuates around zero.

$$\langle \frac{dX}{dt} \rangle = \langle \sum_i \frac{\partial X}{\partial \mathbf{r_i}} \cdot \frac{\mathbf{r}_i}{dt} \rangle = \langle \sum_i \mathbf{F}_i \cdot \mathbf{v}_i \rangle = \langle \sum_i p_i \rangle = 0. \tag{6.15}$$

In Fig. 6.8**a** we have plotted a time series of the total power expended by the active

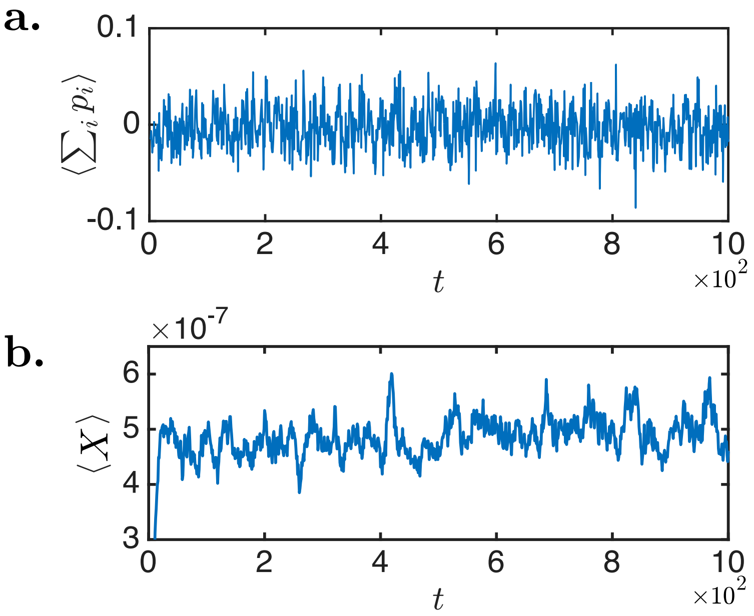

Fig. 6.8. Model-A: **a.** Time series of total power spent by the active forces. **b.** Time series of average value of X in the steady state. Both **a.** and **b.** are obtained for the value of $N = 32$, $h_X = -1000$ and $V_0 = 0.3$ averaged over 30 different realisations of the flow field.

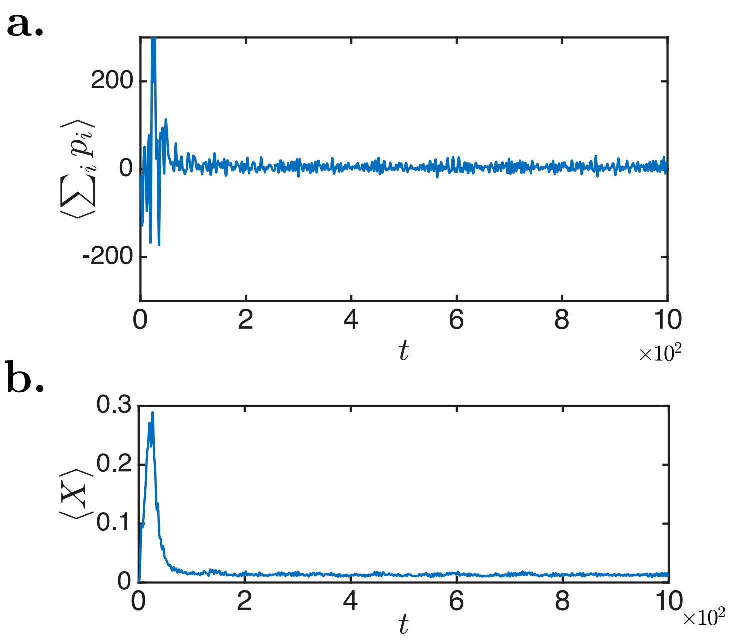

Fig. 6.9. Model-B : **a.** Time series of total power spent by the active forces. **b.** Time series of average value of X in the steady state. Both **a.** and **b.** are obtained for the values of $N = 128$, $h_X = -2.0$ and $V_0 = 1.0$ averaged over 20 different realisations of the flow field

forces in a Model A swarm. It is clear that this quantity, in the steady state, fluctuates around zero when the average non-affine parameter X attains a steady state (panel **b** of the same figure). In Fig. 6.9**a** and **b**, the corresponding quantities are plotted for Model B. A comparison shows that, while the graphs are qualitatively similar, both the non-affine parameter and the mean of the squared power to maintain the shape is much smaller in Model A than in B. This is obvious because the former produces a much more "floppy" swarm with large (affine) changes of shape that does not cost energy. On the other hand, in Model B, the nature of the reference configuration with the ghost layers ensure that all changes of shape are non-affine and needs to be resisted by active forces. This makes the structure of the swarm stiffer and takes larger active forces to maintain even though the average power still vanishes. The distribution of the power expended for the two models is shown in Fig. 6.10. We end this chapter by discussing an interesting application of our drone swarms. It is well known that the structure of a turbulent flow field can be efficiently interrogated using tracer particles [149, 150]. Recently, there has been progress in understanding the dynamics of extended objects such as polymers[135, 146]. As mentioned before, these studies showed that a lot of information about the turbulent velocity field can be obtained by studying the dynamics of polymers embedded in this field [135].

One of the obvious problems in such studies is the limited spatial scale from which information may be obtained. This is restricted by the size of the polymer and is not

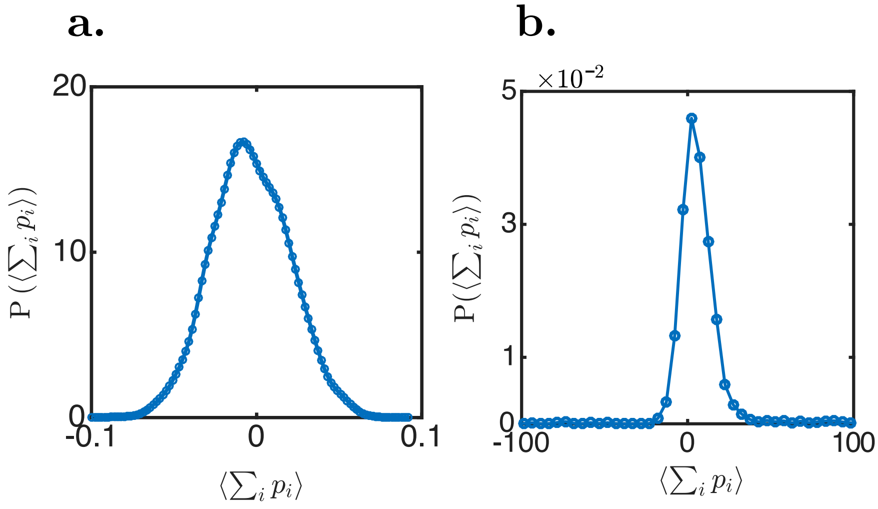

Fig. 6.10. Distribution of time series of averaged power around zero for **a.** Model-A and **b.** Model-B obtained for the parameters as in Fig 6.8, 6.9. The peak of the distribution indicates the energy-efficiency of the stabilization algorithm.

very useful if we need to interrogate a turbulent field of the size of a few meters to kilometers, for example a tropical hurricane or cyclone. This is where robotic swarms may become useful. One may be able to measure the local velocity field using appropriate sensors and compute correlation functions and structure factors “on the fly”.

While this is of course possible, our non-affine field stabilized drone swarms can go a step further. To see this, we first point out that interestingly, no knowledge of the velocity field is necessary to derive the active forces. They depend only on χ and therefore only on the knowledge of the instantaneous and reference positions. Obtaining information about positions is technically far easier than measuring local flow velocities. Further, in Model B in the steady state, non-affine forces exactly balances the destabilising flow field, since all fluctuations of the shape are non-affine due to the presence of the ghost layers. Therefore an imprint of the statistics of the flow is present in the statistics of the non-affine forces used to stabilise the swarm in the first place. The statistics of background flow field can be obtained as a bonus from that of non-affine forces.

We show this by calculating the longitudinal structure factor [151] for particle velocity $S_v^{||}(r_{ij}) = \langle((\mathbf{v}_i - \mathbf{v}_j)\cdot\hat{\mathbf{r}}_{ij})^2\rangle$ and non-affine forces $S_{\mathcal{F}}^{||}(r_{ij}) = \langle((\mathcal{F}_i - \mathcal{F}_j)\cdot\hat{\mathbf{r}}_{ij})^2\rangle$ averaged over different ensembles. Fig. 6.11**a** and **b** shows the velocity and force structure factor together with the expected Eulerian form obtained from the flow field in Model A(**a.**) and Model B(**b.**). In both the models, the velocity structure function follows the Eule-

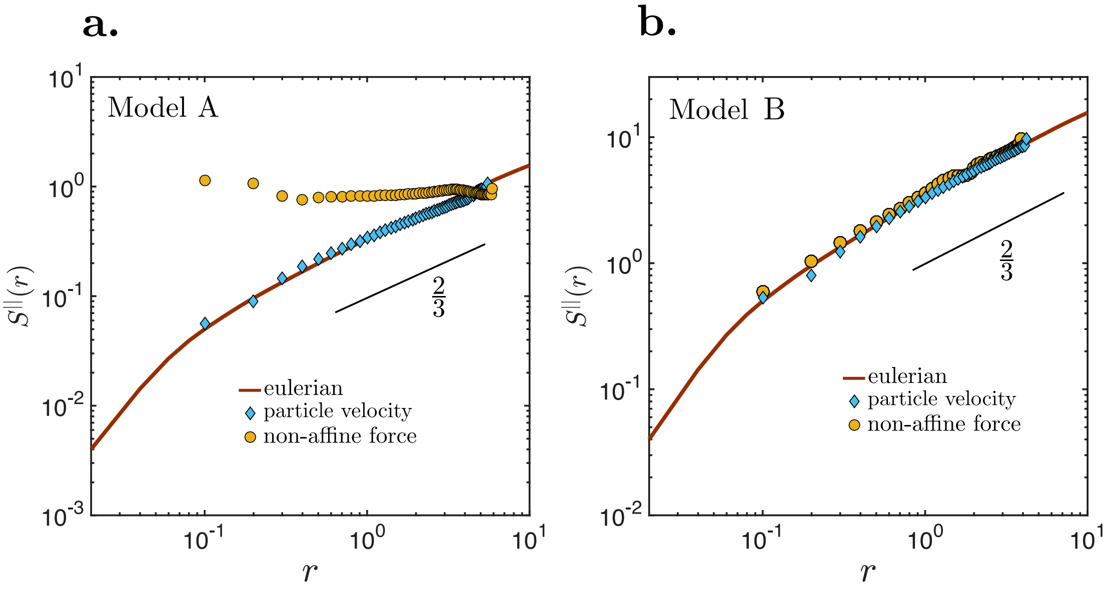

Fig. 6.11. Plot of longitudinal structure factor $S^{||}(r)$ as a function of distance r measured at Eulerian points (solid line), using velocities of individual particles(blue diamond), and using non-affine forces (yellow dots). The simulation was done for the ring size of radius $R_s = 2$, box size $L = 40$ and for $N = 128$ particles. In above the parameters were set to, **a.** for Model A, $V_0 = 0.1$, $h_X = -1000$ and **b.** for Model B $V_0 = 1.0$, $h_X = -2$. For dots and diamonds, simultaneous binning was done on distances and the value of structure factor. It is observed that for model B, the statistics for the underlying turbulent field can be obtained solely through the non-affine forces.

rian curve. The structure factor of the non-affine forces, however, is almost a constant for Model A but reproduces $S_v^{||}(r_{ij})$ for Model B.

To understand this we present below a small exercise to show the relation between the velocity and the non-affine force structure functions for both the models. Consider a small deformation of the ring away from the reference configuration $\{\mathbf{R}\}$ in time $\tau(= m/\gamma)$. The global non-affinity X thus produced can be expressed as a Taylor expansion in terms of the displacements $\{\mathbf{u}\}$,

$$X(\{\mathbf{u}\}, \{\mathbf{R}\}) = X(\{\mathbf{R}\}) + \sum_{i,\alpha} \frac{\partial X}{\partial u_i^\alpha}\bigg|_{\{\mathbf{R}\}} u_i^\alpha + \sum_{i,k,\alpha,\gamma} \frac{\partial^2 X}{\partial u_i^\alpha \partial u_k^\gamma}\bigg|_{\{\mathbf{R}\}} u_i^\alpha u_k^\gamma. \tag{6.16}$$

The first two terms vanish when evaluated at the reference configuration. Non-affine force $\mathcal{F}_i$ on particle i is then obtained by taking another derivative of the above equation,

$$\mathcal{F}_i^\alpha = h_X N \sum_{k,\gamma} \frac{\partial^2 X}{\partial u_i^\alpha \partial u_k^\gamma}\bigg|_{\{\mathbf{R}\}} u_k^\gamma = h_X \sum_{k,\gamma} \phi_{ik}^{\alpha\gamma} u_k^\gamma. \tag{6.17}$$

Here, the constants $\phi_{ik}^{\alpha\gamma}$ are related to the projection matrix P. By construction and from the definition of X, it is easy to show that $\phi_{ik}^{\alpha\gamma} = c_{i-k}\delta_{\alpha\gamma}$ with k being restricted to the neighbours and next nearest neighbours of i. Therefore, with the definition

$\Omega^2(i) \equiv \Omega(i) \cup \Omega(\Omega(i))$ and pulling out the displacement of the i^{th} particle from the sum, the non-affine force takes the following form,

$$\mathcal{F}_i = h_X[-c_1\mathbf{u}_i + \sum_{k\in\Omega^2(i),k\neq i} c_k\mathbf{u}_k], \tag{6.18}$$

and $c_1 = \sum_{k\in\Omega^2(i),k\neq i} c_k$. Note that, this expression can also be obtained from the usual expression of X and its derivative, see Eq. (6.12). However, it is useful to show the linearity in $\mathbf{u}$ when derived in this way. Since all sites on the ring are equivalent, the force on any other particle j is,

$$\mathcal{F}_j = h_X[-c_1\mathbf{u}_j + \sum_{k\in\Omega^2(j),k\neq j} c_k\mathbf{u}_k]. \tag{6.19}$$

Subtracting Eq. (6.19) from Eq. (6.18) while correcting for trivial rotation and translation yields,

$$\mathcal{F}_i - \mathcal{F}_j = -h_X[c_1(\mathbf{u}_i - \mathbf{u}_j) - \sum_{k=0}^{k=n} c_k(\mathbf{u}_{i+1+k} - \mathbf{u}_{j+1+k} + \mathbf{u}_{i-1-k} - \mathbf{u}_{j-1-k})]. \tag{6.20}$$

Although, the above equation is true for both the models, constants c needs to be calculated appropriately with $n = 3$ for Model-A and $n = 1$ for Model-B. Taking a dot product of Eq. (6.20) with $\hat{\mathbf{r}}_{ij}$,

$$(\mathcal{F}_i - \mathcal{F}_j)\cdot\hat{\mathbf{r}}_{ij} = -h_X[\underbrace{c_1(\mathbf{u}_i - \mathbf{u}_j)\cdot\hat{\mathbf{r}}_{ij}}_{\text{I}} \underbrace{- \sum_k c_k(\mathbf{u}_{i+1+k} - \mathbf{u}_{j+1+k} + \mathbf{u}_{i-1-k} - \mathbf{u}_{j-1-k})\cdot\hat{\mathbf{r}}_{ij}}_{\text{II}}]. \tag{6.21}$$

The second term II in the above expression tends to produce affine deformations. Since in Model B affine transformations other than global translation and rotation are restricted, term II is small and bounded at all instants. On the other hand, this term tends to diverge in Model A (see Fig. 6.12). For small values of V_0^2/h_X and considering bots to be tracer particles, displacements are proportional to $\mathbf{U}(\mathbf{r}_i, t)\tau$. Substituting for displacements and approximating the Eq. (6.21) with the first term on right hand side we obtain,

$$(\mathcal{F}_i - \mathcal{F}_j)\cdot\hat{\mathbf{r}}_{ij} \simeq c_1\tau(\mathbf{U}(\mathbf{R}_i, t) - \mathbf{U}(\mathbf{R}_j, t))\cdot\hat{\mathbf{r}}_{ij}. \tag{6.22}$$

Finally, upon squaring and taking ensemble average of the above equations yields the desired structure function for non-affine force and the background velocity field,

$$\langle((\mathcal{F}_i - \mathcal{F}_j)\cdot\hat{\mathbf{r}}_{ij})^2\rangle \simeq \langle(c_1\tau(\mathbf{U}(\mathbf{R}_i, t) - \mathbf{U}(\mathbf{R}_j, t))\cdot\hat{\mathbf{r}}_{ij})^2\rangle \sim |\mathbf{r}_{ij}|^{2/3}. \tag{6.23}$$

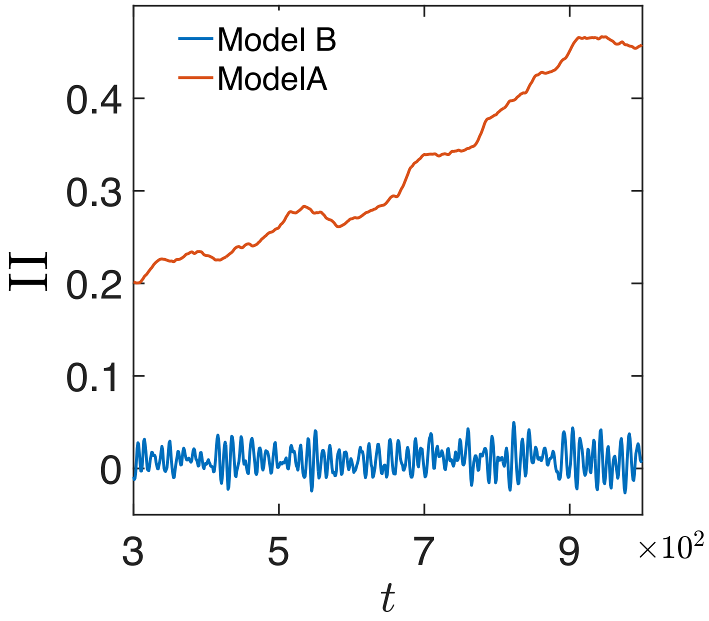

Fig. 6.12. Plot of term II of Eq. (6.21) as a function of time for both Model A (red) and B (blue). The term II is averaged over 50 different realization of the flow field evaluated for the set $(h_X, V_0) = (-1000, 0.1)$ and $(-2, 0.1)$ for Model A and B respectively. For better statistics sum over all equivalent pair of $i - j$ are considered.

Note that this approximation fails for Model A because term II cannot be neglected in this case.

For completeness, we also compute the two-point spatial non-affine correlation C_χ. Defining,

$$C_\chi(i,j) \equiv \frac{\langle \chi_i \chi_j \rangle - \langle \chi_i \rangle \langle \chi_j \rangle}{\sqrt{\langle (\chi_i - \langle \chi_i \rangle)^2 \rangle} \sqrt{\langle (\chi_j - \langle \chi_j \rangle)^2 \rangle}}. \tag{6.24}$$

These correlation are symmetric over the ring and is plotted as a function of particle id's i in Fig. 6.13. We observe that these correlations are long-range for both models. However, in Model A, it decays comparatively faster. Since non-affine force are nothing but the derivatives of χ, this further supports the fact that non-affine forces are correlated as well.

This surprising result elucidate a very important aspect of the Model B swarm. Since, non-affine forces need to be computed anyway in order to stabilise the structure, no extra measurements are required for obtaining the structure factor of the background flow field. This novel outcome of our study has important application in the field of turbulence. The set of robotic agents such as drones can be setup as a Model B swarm to probe the statistics of the atmospheric turbulence at the length scale of miles. It is also easy to make a swarm switch between Model A and Model B modes because the difference is only in the reference configurations. The swarm can, therefore, fly

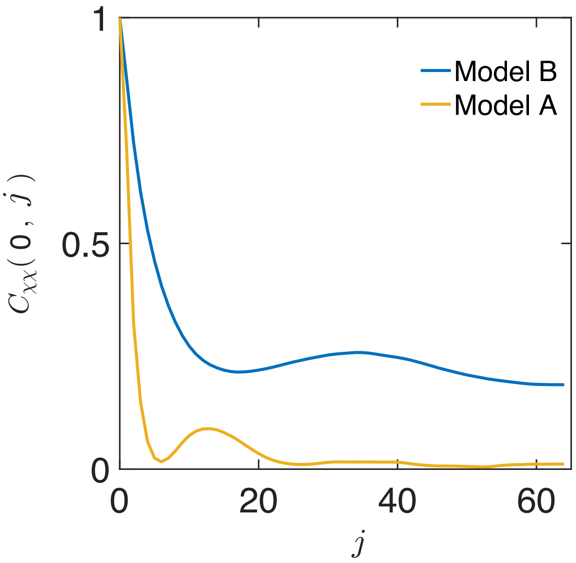

Fig. 6.13. Non-affine correlation between particle $i = 0$ and j for Model A and B. The correlations are obtained for values same set of parameters as in Fig. 6.12 averaged over 50 different realisations of the flow field. For better statistics, further averaging over equivalent pair with fixed $i - j$ is done.

in the floppy mode to conserve energy but switch to a stiffer configuration when a measurement of the background velocity field is needed.

Finally, we comment on the real world feasibility and technological aspect of our stabilisation algorithm. Of-course the active robotic agents are required to produce enough thrust to propel against turbulent flow, the proposed algorithm can stabilise the flock in a desired pattern. The formulation developed here can be used to stabilize flock of UAV (Unmanned Aerial Vehicle, e.g. drone, quadcopter, multirotor) or a cluster of satellites (e.g. SpaceX's Starlink) [152, 153] or cluster of high-altitude balloons (e.g. Project Loon) [154, 155] to preserve a reference pattern in fluctuating environments. For an UAV, this is typically accomplished by getting the precise position of each of the objects (either by performing a Sensor fusion using Inertial Measurement Sensors and/or GPS or by using ground-based radio subsystem [156]) in space and then compensating any deviation from the reference template using the classic Proportional Integral Differential (PID) control system or its variants (e.g. adaptive PID loop). But in the presence of a highly fluctuating and turbulent environment, say in the presence of a mild storm, maintaining the flock to its reference position becomes difficult using PID control loop alone. Also, this requires careful tuning of the three PIC coefficients (namely, K_p, K_i & K_d). The non-affine field may serve as a better alternative control loop than the traditional PID control having only one control parameter, namely the strength of the field h_X. The reference template can be updated even in flight to form a different pattern. A low-bandwidth but low-latency short-ranged) RF communication system is required to be present in each of the objects so that they can communicate their local positions to other objects present within the coarse-graining volume to calculate their local non-affine parameters. This should be achievable by either Bluetooth mesh networking implemented using Bluetooth Low Energy 4.0 (BLE) devices or ZigBee Wireless Mesh Networking (WMN) devices or possibly using other emergent technologies. The cluster of entities should be able to communicate with a central ground station by a long-range but low to moderate latency communication hardware. In order to efficiently compute their own non-affine parameter and the corrective non-affine force required to compute the target position, the entities should use a fast microcontroller, preferably having hardware single or double precision Floating Point Units (FPU).

7

Thesis conclusion and future direction

We generalise, and then use the non-affine projection formalism to study several two and three dimensional lattices. We have focused on both closed packed and open crystals as well as multi atom basis in thermal fluctuations. Atomic displacements once coarse-grinned over some specified volume can then be decomposed into two mutually orthogonal subspaces. Whereas eigenvectors of PCP obtained after such formalism are shown to be related with defect precursor in the crystals, sum of eigenvalues measures the total non-affine contribution. For any dimension d these modes are $d-$fold degenerate. While for lattices with one particle basis like triangular, square, sc, bcc, fcc, there exist a significant gap between the largest eigenvalue and the rest. In huge lattices, the eigenvector associated with the largest eigenvalue may be related to well known lattice defects such as dislocations and stacking faults. Open lattices like honeycomb and Kagome lacks this gap. Nevertheless for open lattices where the gap is absent, we observed soft non-affine modes continues to be related to the well known floppy modes. For fcc systems, mechanism of stacking or slip can also be understood in this framework.

Suppressing the non-affine modes related to defect precursors are shown to stabilise any desired lattice structure for any given interaction. The lattice thus produced is translationally invariant and the structure of the lattice can be changed at will. The qualitative features of the stabilisation mechanism is independent of the nature and interaction between particles. A feedback controlled optical traps is proposed for the experimental realisation of the non-affine field and may be used to verify our results.

Finally, we extended the stabilisation mechanism to non-thermal fluctuations such as noise in a turbulent fluid and show the general applicability of our stabilisation algorithm for any order/pattern. Active robotic drones aware of their neighbours can adjust their positions to minimise non-affine deformations caused by turbulent field thus stabilising the global pattern. We show that just by fixing the pattern one automatically obtains the statistics of the background flow field. This way of stabilising may prove useful for the experiments on real world turbulence, where measuring velocities is difficult in real time. On the other hand, continuous snapshot of the swarm of drones may reveal the information and statistics of the turbulence.

This decomposition of displacements into affine and non-affine have lead to a deeper understanding in several disparate contexts. For example, it has been possible to elucidate many aspects concerning the failure of rigid solids under load. Loading a rigid solid is tantamount to quenching it across an equilibrium first order phase transition [37]. Yielding of a crystal under load is simply the decay of this metastable phase to the stable phase, which eliminates stress by non-affine atomic rearrangements. This radically different viewpoint nevertheless allows one to calculate, for the first time, strain rate dependent yielding thresholds using classical nucleation theory.

In networked solids, where atoms are bound by strong chemical bonds, dislocations do not form. Nevertheless such solids may deform by special singular formations called pleats or “ripplocations", which have been described within the same language of non-affine displacements [30, 33].

Finally, in a *protein* - a large molecule consisting of interacting atoms with no spatial long ranged order - it has been shown that important conformational changes, which precede binding to ligands are always non-affine. These may be discovered by simply projecting out the local atomic displacements using the same projection formalism. Regions with large susceptibility for non-affine displacements correlate with binding hotspots and spatial correlations of the magnitude of non-affine ness mark sites of allosteric control [38].

Future direction

The findings presented in this thesis are mainly limited to harmonic lattices, but systems where harmonic approximation breaks down, a more comprehensive calculation is needed. Effects of such anhamonicities on the precursors to lattice defects may be included either perturbatively or using self consistent field theories [157, 158]. In amorphous solids, defects responsible for plastic flow co-localizes with extended vibrational modes and can be isolated with some effort [26]. Such localized defects resembles with the defect precursors discussed in the thesis. We believe, an extension of the present work to amorphous solids may show some light on the deformation mechanism of amorphous solids. In addition, an elasticity theory which involves both affine and non-affine displacements can be developed. This will go beyond the classic theory of elasticity where imposed compatibility conditions rule out the possibilities of dislocation like defects. A coarse-grained theory of non-affine displacements will also, finally, remove the constraint of having a tagged reference and will be able to describe point defects and particle exchanges (see Sec 2.4).

Landau theories in terms of an elastic order parameter are used to explain structural phase transformations (Martensitic) [159–162]. With imposed compatibility constraints, such strain only theories restrict the displacement field and prevents formation of defects or atomic rearrangements. Such theories therefore, by construction can only describe structural transitions where atomic rearrangements do not occur. Experiments on colloidal Martensites show that such rearrangements leading to non-affine displacements readily occur during nucleation of one crystal inside another [6, 56]. Although some efforts have been made to include non-elastic displacements [163–166], a Landau theory which involves all non-affine modes can be explored further.

Furthermore, as shown in Chapter 5, non-affine fields with a tuning parameter can be modeled to stabilize lattices of different symmetries. However, a system where different kinds of order compete with one another may result in a kinetically arrested state with glass like properties [167–169]. Investigation along these lines can be an interesting future goal.

Finally, we showed that the statistics of turbulent field can be obtained using a feedback controlled non-affine forces. We suspect this result stems through fluctuation dissipation theorem and is not limited to turbulent fields. Thus, a systematic study to establish this result for any general fluctuating environment must be done. Additionally the formulation developed here can be used in control theories to stabilize any set of parameters (such as an abstract set of quantities in an electronic circuit) close to the desired values. This is advantageous over the existing control theories where at least three control parameters are required [170], whereas our formalism has only one control parameter viz. h_X. Future work concerning this aspect of the non-affinity might be a good quest.

A

Appendix A

A.1 Dynamical matrix for harmonic interactions

We give below the expressions for the dynamical matrices for all the lattices studied in this paper. We have kept a, the lattice parameter, and the spring constants k_1 and k_2 explicitly for clarity. For each case we have included nearest neighbor and next nearest neighbor bonds, with spring constants k_1 and k_2, respectively. For the triangular lattice only nearest neighbor bonds were retained ($k_2 = 0$). Separate expressions are given for the additional terms that result in the triangular and honeycomb lattices from the introduction of additional bond-bending terms.

A.1.1 Square

$$\begin{aligned}
A_{11} &= 2(k_1 + k_2 - \cos(aq_x)(k_1 + k_2\cos(aq_y))) \\
A_{12} &= 2k_2\sin(aq_x)\sin(aq_y) = A_{21} \\
A_{22} &= 2(k_1 + k_2 - \cos(aq_y)(k_1 + k_2\cos(aq_x))) \\
D(\mathbf{q}) &= \begin{pmatrix} A_{11} & A_{12} \\ A_{21} & A_{22} \end{pmatrix}
\end{aligned} \tag{A.1}$$

A.1.2 Triangular

$$
\begin{aligned}
B_{11} &= k_1\left(3 - 2\cos(aq_x) - \cos\left(\frac{aq_x}{2}\right)\cos\left(\frac{\sqrt{3}aq_y}{2}\right)\right) \\
B_{12} &= k_1\left(\sqrt{3}\sin\left(\frac{aq_x}{2}\right)\sin\left(\frac{\sqrt{3}aq_y}{2}\right)\right) = B_{21} \\
B_{22} &= k_1\left(3 - 3\cos\left(\frac{aq_x}{2}\right)\cos\left(\frac{\sqrt{3}aq_y}{2}\right)\right) \\
D(\mathbf{q}) &= \begin{pmatrix} B_{11} & B_{12} \\ B_{21} & B_{22} \end{pmatrix} \qquad \text{(A.2)}
\end{aligned}
$$

A.1.3 Triangular with bond bending:

$$
\begin{aligned}
B'_{11} &= 3k_b\left[3 - \cos(aq_x) - 2\cos\left(\frac{aq_x}{2}\right)\cos\left(\frac{\sqrt{3}aq_y}{2}\right)\right] = B'_{22} \\
B'_{12} &= 0 = B'_{21} \\
D(\mathbf{q}) &= \begin{pmatrix} B'_{11} & B'_{12} \\ B'_{21} & B'_{22} \end{pmatrix} \qquad \text{(A.3)}
\end{aligned}
$$

A.1.4 Planar honeycomb

$$
\begin{aligned}
W_1 &= \frac{3k_1}{2} + 3k_2 - 3k_2\cos\left(\frac{3aq_x}{2}\right)\cos\left(\frac{\sqrt{3}aq_y}{2}\right) \\
W_2 &= \sqrt{3}k_2\sin\left(\frac{3aq_x}{2}\right)\sin\left(\frac{\sqrt{3}aq_y}{2}\right)
\end{aligned}
$$

$$W_3 = k_1\left(-\exp\left(iaq_x\right) - \frac{\exp\left(-\frac{iaq_x}{2}\right)\cos\left(\frac{\sqrt{3}aq_y}{2}\right)}{2}\right)$$

$$W_4 = \frac{k_1}{2}\left(\sqrt{3}i\exp\left(-\frac{iaq_x}{2}\right)\sin\left(\frac{\sqrt{3}aq_y}{2}\right)\right)$$

$$W_5 = \frac{3k_1}{2} + 3k_2 - 2k_2\cos\left(\sqrt{3}aq_y\right) - k_2\cos\left(\frac{3aq_x}{2}\right)\cos\left(\frac{\sqrt{3}aq_y}{2}\right)$$

$$W_6 = \frac{k_1}{2}\left(-3\exp\left(-\frac{iaq_x}{2}\right)\cos\left(\frac{\sqrt{3}aq_y}{2}\right)\right)$$

$$D(\mathbf{q}) = \begin{pmatrix} W_1 & W_2 & W_3 & W_4 \\ W_2^* & W_5 & W_4 & W_6 \\ W_3^* & W_4^* & W_1 & W_2 \\ W_4^* & W_6^* & W_2^* & W_5 \end{pmatrix} \tag{A.4}$$

A.1.5 Honeycomb with bond bending

$$W_1' = 3k_b$$

$$W_2' = i\sqrt{3}k_b\exp\left(-\frac{3iq_xa}{2}\right)\sin\left(\frac{\sqrt{3}q_ya}{2}\right)$$

$$W_3' = -3k_b\exp\left(-\frac{iq_xa}{2}\right)\cos\left(\frac{\sqrt{3}q_ya}{2}\right)$$

$$W_4' = -2i\sqrt{3}k_b\exp\left(-\frac{iq_xa}{2}\right)\sin\left(\frac{\sqrt{3}q_ya}{2}\right)$$

$$W_5' = k_b\left(7 + 2\cos\left(\frac{3q_x a}{2}\right)\cos\left(\frac{\sqrt{3}q_y a}{2}\right)\right)$$

$$W_6' = -3k_b \exp\left(-\frac{iq_x a}{2}\right)\left(2e^{\frac{3iq_x a}{2}} + \cos\left(\frac{\sqrt{3}q_y a}{2}\right)\right)$$

$$W_7' = -3k_b\left(2\cos(q_x a) + \exp\left(\frac{iq_x a}{2}\right)\cos\left(\frac{\sqrt{3}q_y a}{2}\right) - 2i\sin(q_x a)\right)$$

$$D(\mathbf{q}) = \begin{pmatrix} W_1' & W_2' & W_3' & W_4' \\ W_2'^{*} & W_5' & W_4' & W_6' \\ W_3'^{*} & W_4'^{*} & W_1' & W_2'^{*} \\ W_4'^{*} & W_7' & W_2' & W_5' \end{pmatrix} \tag{A.5}$$

A.1.6 Kagome

$$M_1 = k_1 + 3k_2$$

$$M_2 = 0$$

$$\begin{aligned} M_3 = {} & -\frac{1}{4}k_1 \exp\left(-i\big(\frac{aq_x}{4} + \frac{\sqrt{3}aq_y}{4}\big)\right) - \frac{1}{4}k_1 \exp\left(-i\big(-\frac{aq_x}{4} - \frac{\sqrt{3}aq_y}{4}\big)\right) \\ & - \frac{3}{4}k_2 \exp\left(-i\big(-\frac{3aq_x}{4} + \frac{\sqrt{3}aq_y}{4}\big)\right) - \frac{3}{4}k_2 \exp\left(-i\big(\frac{3aq_x}{4} - \frac{\sqrt{3}aq_y}{4}\big)\right) \end{aligned}$$

$$\begin{aligned} M_4 = {} & -\frac{1}{4}\sqrt{3}k_1 \exp\left(-i\big(\frac{aq_x}{4} + \frac{\sqrt{3}aq_y}{4}\big)\right) - \frac{1}{4}\sqrt{3}k_1 \exp\left(-i\big(-\frac{aq_x}{4} - \frac{\sqrt{3}aq_y}{4}\big)\right) \\ & + \frac{1}{4}\sqrt{3}k_2 \exp\left(-i\big(-\frac{3aq_x}{4} + \frac{\sqrt{3}aq_y}{4}\big)\right) + \frac{1}{4}\sqrt{3}k_2 \exp\left(-i\big(\frac{3aq_x}{4} - \frac{\sqrt{3}aq_y}{4}\big)\right) \end{aligned}$$

$$\begin{aligned}
M_5 &= -\frac{1}{4}k_1\exp\left(-i\big(-\frac{aq_x}{4}+\frac{\sqrt{3}aq_y}{4}\big)\right)-\frac{1}{4}k_1\exp\left(-i\big(\frac{aq_x}{4}-\frac{\sqrt{3}aq_y}{4}\big)\right)\\
&\quad -\frac{3}{4}k_2\exp\left(-i\big(\frac{3aq_x}{4}+\frac{\sqrt{3}aq_y}{4}\big)\right)-\frac{3}{4}k_2\exp\left(-i\big(-\frac{3aq_x}{4}-\frac{\sqrt{3}aq_y}{4}\big)\right)
\end{aligned}$$

$$\begin{aligned}
M_6 &= \frac{1}{4}\sqrt{3}k_1\exp\left(-i\big(-\frac{aq_x}{4}+\frac{\sqrt{3}aq_y}{4}\big)\right)+\frac{1}{4}\sqrt{3}k_1\exp\left(-i\big(\frac{aq_x}{4}-\frac{\sqrt{3}aq_y}{4}\big)\right)\\
&\quad -\frac{1}{4}\sqrt{3}k_2\exp\left(-i\big(\frac{3aq_x}{4}+\frac{\sqrt{3}aq_y}{4}\big)\right)-\frac{1}{4}\sqrt{3}k_2\exp\left(-i\big(-\frac{3aq_x}{4}-\frac{\sqrt{3}aq_y}{4}\big)\right)
\end{aligned}$$

$$M_7 = 3k_1+k_2$$

$$\begin{aligned}
M_8 &= -\frac{1}{4}3k_1\exp\left(-i\big(\frac{aq_x}{4}+\frac{\sqrt{3}aq_y}{4}\big)\right)-\frac{3}{4}k_1\exp\left(-i\big(-\frac{aq_x}{4}-\frac{\sqrt{3}aq_y}{4}\big)\right)\\
&\quad -\frac{1}{4}k_2\exp\left(-i\big(-\frac{3aq_x}{4}+\frac{\sqrt{3}aq_y}{4}\big)\right)-\frac{1}{4}k_2\exp\left(-i\big(\frac{3aq_x}{4}-\frac{\sqrt{3}aq_y}{4}\big)\right)
\end{aligned}$$

$$\begin{aligned}
M_9 &= -\frac{1}{4}3k_1\exp\left(-i\big(-\frac{aq_x}{4}+\frac{\sqrt{3}aq_y}{4}\big)\right)-\frac{3}{4}k_1\exp\left(-i\big(\frac{aq_x}{4}-\frac{\sqrt{3}aq_y}{4}\big)\right)\\
&\quad -\frac{1}{4}k_2\exp\left(-i\big(\frac{3aq_x}{4}+\frac{\sqrt{3}aq_y}{4}\big)\right)-\frac{1}{4}k_2\exp\left(-i\big(-\frac{3aq_x}{4}-\frac{\sqrt{3}aq_y}{4}\big)\right)
\end{aligned}$$

$$\begin{aligned}
M_{10} &= \frac{5k_1}{2}+\frac{3k_2}{2}\\
M_{11} &= \frac{\sqrt{3}k_1}{2}-\frac{\sqrt{3}k_2}{2}\\
M_{12} &= -k_1\exp\big(i\frac{aq_x}{2}\big)-k_1\exp\big(-i\frac{aq_x}{2}\big)\\
M_{13} &= \frac{3k_1}{2}+\frac{5k_2}{2}\\
M_{14} &= -k_2\exp\big(i\frac{\sqrt{3}aq_y}{2}\big)-k_2\exp\big(-i\frac{\sqrt{3}aq_y}{2}\big)
\end{aligned}$$

$$M_{15} = \frac{\sqrt{3}k_2}{2} - \frac{\sqrt{3}k_1}{2}$$

$$D(\mathbf{q}) = \begin{pmatrix} M_1 & M_2 & M_3 & M_4 & M_5 & M_6 \\ M_2^* & M_7 & M_4 & M_8 & M_6 & M_9 \\ M_3^* & M_4^* & M_{10} & M_{11} & M_{12} & M_2 \\ M_4^* & M_8^* & M_{11}^* & M_{13} & M_2 & M_{14} \\ M_5^* & M_6^* & M_{12}^* & M_2^* & M_{10} & M_{15} \\ M_6^* & M_9^* & M_2^* & M_{14}^* & M_{15}^* & M_{13} \end{pmatrix} \tag{A.6}$$

A.1.7 SC

$$S_{11} = -2\cos(aq_x)(k_1 + k_2(\cos(aq_y) + \cos(aq_z))) + 2k_1 + 4k_2$$

$$S_{12} = 2k_2 \sin(aq_x)\sin(aq_y) = S_{21}$$

$$S_{13} = 2k_2 \sin(aq_x)\sin(aq_z) = S_{31}$$

$$S_{22} = -2\cos(aq_y)(k_1 + k_2(\cos(aq_x) + \cos(aq_z))) + 2k_1 + 4k_2$$

$$S_{23} = 2k_2 \sin(aq_y)\sin(aq_z) = S_{32}$$

$$S_{33} = -2\cos(aq_z)(k_1 + k_2(\cos(aq_x) + \cos(aq_y))) + 2k_1 + 4k_2$$

$$D(\mathbf{q}) = \begin{pmatrix} S_{11} & S_{12} & S_{13} \\ S_{21} & S_{22} & S_{23} \\ S_{31} & S_{32} & S_{33} \end{pmatrix} \tag{A.7}$$

A.1.8 BCC

$$G_{11} = -\frac{8}{3}k_1 \cos\left(\frac{aq_x}{2}\right)\cos\left(\frac{aq_y}{2}\right)\cos\left(\frac{aq_z}{2}\right) - 2k_2\cos\left(aq_x\right) + \frac{8}{3}k_1 + 2k_2$$

$$G_{12} = \frac{8}{3}k_1 \cos\left(\frac{aq_z}{2}\right)\sin\left(\frac{aq_x}{2}\right)\sin\left(\frac{aq_y}{2}\right) = G_{21}$$

$$G_{13} = \frac{8}{3}k_1 \cos\left(\frac{aq_y}{2}\right)\sin\left(\frac{aq_x}{2}\right)\sin\left(\frac{aq_z}{2}\right) = G_{31}$$

$$G_{22} = -\frac{8}{3}k_1 \cos\left(\frac{aq_x}{2}\right)\cos\left(\frac{aq_y}{2}\right)\cos\left(\frac{aq_z}{2}\right) - 2k_2\cos\left(aq_y\right) + \frac{8}{3}k_1 + 2k_2$$

$$G_{23} = \frac{8}{3}k_1 \cos\left(\frac{aq_x}{2}\right)\sin\left(\frac{aq_y}{2}\right)\sin\left(\frac{aq_z}{2}\right) = G_{32}$$

$$G_{33} = -\frac{8}{3}k_1 \cos\left(\frac{aq_x}{2}\right)\cos\left(\frac{aq_y}{2}\right)\cos\left(\frac{aq_z}{2}\right) - 2k_2\cos\left(aq_z\right) + \frac{8}{3}k_1 + 2k_2$$

$$D(\mathbf{q}) = \begin{pmatrix} G_{11} & G_{12} & G_{13} \\ G_{21} & G_{22} & G_{23} \\ G_{31} & G_{32} & G_{33} \end{pmatrix} \tag{A.8}$$

A.1.9 FCC

$$F_{11} = 4k_1 + 2k_2 - 2k_2\cos\left(aq_x\right) - 2k_1\cos\left(\frac{aq_x}{2}\right)\left(\cos\left(\frac{aq_y}{2}\right) + \cos\left(\frac{aq_z}{2}\right)\right)$$

$$F_{12} = 2k_1 \sin\left(\frac{aq_x}{2}\right)\sin\left(\frac{aq_y}{2}\right) = F_{21}$$

$$F_{13} = 2k_1 \sin\left(\frac{aq_x}{2}\right) \sin\left(\frac{aq_z}{2}\right) = F_{31}$$

$$F_{22} = 4k_1 + 2k_2 - 2k_2 \cos\left(aq_y\right) - 2k_1 \cos\left(\frac{aq_y}{2}\right)\left(\cos\left(\frac{aq_x}{2}\right) + \cos\left(\frac{aq_z}{2}\right)\right)$$

$$F_{23} = 2k_1 \sin\left(\frac{aq_y}{2}\right) \sin\left(\frac{aq_z}{2}\right) = F_{32}$$

$$F_{33} = 4k_1 + 2k_2 - 2k_2 \cos\left(aq_z\right) - 2k_1 \cos\left(\frac{aq_z}{2}\right)\left(\cos\left(\frac{aq_x}{2}\right) + \cos\left(\frac{aq_y}{2}\right)\right)$$

$$D(\mathbf{q}) = \begin{pmatrix} F_{11} & F_{12} & F_{13} \\ F_{21} & F_{22} & F_{23} \\ F_{31} & F_{32} & F_{33} \end{pmatrix} \tag{A.9}$$

A.2 Strain correlation iso-surfaces for 3d lattices

We give below the equations for the iso-surfaces of the strain-strain correlation functions for the 3d lattices as shown in Fig. 3.13. We have used the same notation as in Section 3.3.

A.2.1 SC

The iso-strain surfaces are given by the equations $\beta\langle e_v^2\rangle(\mathbf{q}) = Q_v^{SC}/Q^{SC} = 1$, $\beta\langle e_u^2\rangle(\mathbf{q}) = Q_u^{SC}/Q^{SC} = 1.5$ and $\beta\langle e_s^2\rangle(\mathbf{q}) = Q_s^{SC}/Q^{SC} = 3.6$, where,

$$\begin{aligned} Q^{SC} = \; & a^2\Big[k_1^3 q_x^2 q_y^2 q_z^2 + k_1^2 k_2\Big(q_x^4\left(q_y^2 + q_z^2\right) + q_x^2\left(q_y^4 + 6q_y^2 q_z^2 + q_z^4\right) + q_y^2 q_z^2\left(q_y^2 + q_z^2\right)\Big) \\ & + k_1 k_2^2\Big(q_x^6 + 5q_x^4\left(q_y^2 + q_z^2\right) + q_x^2\left(5q_y^4 + 3q_y^2 q_z^2 + 5q_z^4\right) + q_y^6 + 5q_y^4 q_z^2 + 5q_y^2 q_z^4 + q_z^6\Big) \\ & + k_2^3\Big(2q_x^6 + 3q_x^4\left(q_y^2 + q_z^2\right) + q_x^2\left(3q_y^4 + 8q_y^2 q_z^2 + 3q_z^4\right) + 2q_y^6 + 3q_y^4 q_z^2 + 3q_y^2 q_z^4 + 2q_z^6\Big)\Big], \end{aligned}$$

$$
\begin{aligned}
Q_v^{SC} &= 3k_1^2 q_x^2 q_y^2 q_z^2 + 2k_1 k_2 \Big(q_x^4 \big(q_y^2 + q_z^2 \big) + q_x^2 \big(q_y^4 + q_z^4 \big) + q_y^2 q_z^2 \big(q_y^2 + q_z^2 \big) \Big) \\
&\quad + k_2^2 \Big(q_x^6 + q_x^4 \big(q_y^2 + q_z^2 \big) + q_x^2 \big(q_y^4 + 3q_y^2 q_z^2 + q_z^4 \big) + q_y^6 + q_y^4 q_z^2 + q_y^2 q_z^4 + q_z^6 \Big),
\end{aligned}
$$

$$
\begin{aligned}
Q_u^{SC} &= 3k_1^2 q_x^2 q_y^2 q_z^2 + 2k_1 k_2 \Big(q_x^4 \big(q_y^2 + q_z^2 \big) + q_x^2 \big(q_y^4 + 8q_y^2 q_z^2 + q_z^4 \big) + q_y^2 q_z^2 \big(q_y^2 + q_z^2 \big) \Big) \\
&\quad + k_2^2 \Big(q_x^6 + 9q_x^4 \big(q_y^2 + q_z^2 \big) + 3q_x^2 \big(3q_y^4 + q_y^2 q_z^2 + 3q_z^4 \big) + q_y^6 + q_y^4 q_z^2 + q_y^2 q_z^4 + q_z^6 \Big),
\end{aligned}
$$

$$
\begin{aligned}
Q_s^{SC} &= k_1^2 q_z^2 \big(q_x^4 + q_y^4 \big) + k_1 k_2 \Big(q_x^6 + q_x^4 \big(q_y^2 + 4q_z^2 \big) + q_x^2 \big(q_y^2 - q_z^2 \big)^2 + q_y^2 \big(q_y^4 + 4q_y^2 q_z^2 + q_z^4 \big) \Big) \\
&\quad + k_2^2 \Big(2q_x^6 + q_x^4 q_z^2 + 2q_x^2 \big(3q_y^2 q_z^2 + q_z^4 \big) + 2q_y^6 + q_y^4 q_z^2 + 2q_y^2 q_z^4 \Big).
\end{aligned} \tag{A.10}
$$

A.2.2 BCC

The iso-strain surfaces are given by the equations $\beta\langle e_v^2\rangle(\mathbf{q}) = Q_v^{BCC}/Q^{BCC} = 1.6$, $\beta\langle e_u^2\rangle(\mathbf{q}) = Q_u^{BCC}/Q^{BCC} = 5.5$ and $\beta\langle e_s^2\rangle(\mathbf{q}) = Q_s^{BCC}/Q^{BCC} = 2.15$, where,

$$
\begin{aligned}
Q^{BCC} &= a^2 \Big[k_1^3 \Big(- q_z^4 \big(q_x^2 + q_y^2 \big) + \big(q_x^2 - q_y^2 \big)^2 \big(q_x^2 + q_y^2 \big) - q_z^2 \big(q_x^4 - 10 q_x^2 q_y^2 + q_y^4 \big) + q_z^6 \Big) \\
&\quad + 3k_1^2 k_2 \Big(q_x^6 + 3q_x^4 \big(q_y^2 + q_z^2 \big) + 3q_x^2 \big(q_y^2 - q_z^2 \big)^2 + \big(q_y^2 + q_z^2 \big)^3 \Big) \\
&\quad + 9k_1 k_2^2 \big(q_x^2 + q_y^2 + q_z^2 \big) \Big(q_x^2 \big(q_y^2 + q_z^2 \big) + q_y^2 q_z^2 \Big) + 27 k_2^3 q_x^2 q_y^2 q_z^2 \Big],
\end{aligned}
$$

$$
\begin{aligned}
Q_v^{BCC} &= 3k_1 \big(q_x^2 + q_y^2 \big) \Big(6k_2 q_x^2 q_y^2 + k_1 \big(q_x^2 - q_y^2 \big)^2 \Big) \\
&\quad - 3 \Big(k_1 (k_1 - 6k_2) q_x^4 - 3 \big(2k_1^2 - 6k_1 k_2 + 9k_2^2 \big) q_x^2 q_y^2 + k_1 (k_1 - 6k_2) q_y^4 \Big) q_z^2 \\
&\quad - 3k_1 (k_1 - 6k_2) \big(q_x^2 + q_y^2 \big) q_z^4 + 3k_1^2 q_z^6,
\end{aligned}
$$

$$\begin{aligned} Q_u^{BCC} &= 3\Big[27k_2^2q_x^2q_y^2q_z^2 + 6k_1k_2\Big(q_x^4\big(q_y^2+q_z^2\big)+q_y^2q_z^2\big(q_y^2+q_z^2\big)+q_x^2\big(q_y^4+5q_y^2q_z^2+q_z^4\big)\Big) \\ &\quad + k_1^2\Big(q_x^6+7q_x^4\big(q_y^2+q_z^2\big)+\big(q_y^2-q_z^2\big)^2\big(q_y^2+q_z^2\big)+q_x^2\big(7q_y^4-10q_y^2q_z^2+7q_z^4\big)\Big)\Big], \end{aligned}$$

$$\begin{aligned} Q_s^{BCC} &= 3\Big[9k_2^2\big(q_x^4+q_y^4\big)q_z^2 + 3k_1k_2\Big(q_x^6+q_x^2\big(q_y^2-q_z^2\big)^2+q_y^2\big(q_y^2+q_z^2\big)^2+q_x^4\big(q_y^2+2q_z^2\big)\Big) \\ &\quad + k_1^2\Big(q_x^6-q_x^4\big(q_y^2+2q_z^2\big)+\big(q_y^3-q_yq_z^2\big)^2+q_x^2\big(-q_y^4+8q_y^2q_z^2+q_z^4\big)\Big)\Big]. \end{aligned} \tag{A.11}$$

A.2.3 FCC

The iso-strain surfaces are given by the equations $\beta\langle e_v^2\rangle(\mathbf{q}) = Q_v^{FCC}/Q^{FCC} = 1.44$, $\beta\langle e_u^2\rangle(\mathbf{q}) = Q_u^{FCC}/Q^{FCC} = 3.6$ and $\beta\langle e_s^2\rangle(\mathbf{q}) = Q_s^{FCC}/Q^{FCC} = 2.75$, where,

$$\begin{aligned} Q^{FCC} &= a^2\Big[k_1^3\Big(2q_x^6+3q_x^4\big(q_y^2+q_z^2\big)+q_x^2\big(3q_y^4+8q_y^2q_z^2+3q_z^4\big) \\ &\quad + 2q_y^6+3q_y^4q_z^2+3q_y^2q_z^4+2q_z^6\Big) + 4k_1^2k_2\Big(q_x^6+5q_x^4\big(q_y^2+q_z^2\big) \\ &\quad + q_x^2\big(5q_y^4+3q_y^2q_z^2+5q_z^4\big)+q_y^6+5q_y^4q_z^2+5q_y^2q_z^4+q_z^6\Big) \\ &\quad + 16k_1k_2^2\Big(q_x^4\big(q_y^2+q_z^2\big)+q_x^2\big(q_y^4+6q_y^2q_z^2+q_z^4\big)+q_y^2q_z^2\big(q_y^2+q_z^2\big)\Big) + 64k_2^3q_x^2q_y^2q_z^2\Big], \end{aligned}$$

$$\begin{aligned} Q_v^{FCC} &= 4\Big[k_1^2\Big(q_x^6+q_x^4\big(q_y^2+q_z^2\big)+q_x^2\big(q_y^4+3q_y^2q_z^2+q_z^4\big)+q_y^6+q_y^4q_z^2+q_y^2q_z^4+q_z^6\Big) \\ &\quad + 8k_1k_2\Big(q_x^4\big(q_y^2+q_z^2\big)+q_x^2\big(q_y^4+q_z^4\big)+q_y^2q_z^2\big(q_y^2+q_z^2\big)\Big) + 48k_2^2q_x^2q_y^2q_z^2\Big], \end{aligned}$$

$$\begin{aligned} Q_u^{FCC} &= 4\Big[k_1^2\Big(q_x^6+9q_x^4\big(q_y^2+q_z^2\big)+3q_x^2\big(3q_y^4+q_y^2q_z^2+3q_z^4\big)+q_y^6+q_y^4q_z^2+q_y^2q_z^4+q_z^6\Big) \\ &\quad + 8k_1k_2\Big(q_x^4\big(q_y^2+q_z^2\big)+q_x^2\big(q_y^4+8q_y^2q_z^2+q_z^4\big)+q_y^2q_z^2\big(q_y^2+q_z^2\big)\Big) + 48k_2^2q_x^2q_y^2q_z^2\Big], \end{aligned}$$

$$
\begin{aligned}
Q_s^{FCC} \;=\; & 4\Bigg[k_1^2\Bigg(2q_x^6 + q_x^4 q_z^2 + 2q_x^2\Big(3q_y^2 q_z^2 + q_z^4\Big) + 2q_y^6 + q_y^4 q_z^2 + 2q_y^2 q_z^4\Bigg) \\
& + 4k_1 k_2\Bigg(q_x^6 + q_x^4\Big(q_y^2 + 4q_z^2\Big) + q_x^2\Big(q_y^2 - q_z^2\Big)^2 + q_y^2\Big(q_y^4 + 4q_y^2 q_z^2 + q_z^4\Big)\Bigg) \\
& + 16k_2^2 q_z^2\Big(q_x^4 + q_y^4\Big)\Bigg].
\end{aligned}
\tag{A.12}
$$

B

Appendix B

Dynamical matrix for non-affine interactions

We give below a detailed derivation of the dynamical matrix $\mathbf{D}_X(\mathbf{q})$ used in Chapter 5. Although the derivation presented here is specific to the square lattice, extension to other lattices can be done in similar fashion. In the following, we use the notation where the subscript represents particle indices and the component of vectors or the matrices are denoted by superscripts.

The dynamical matrix, in Chapter 5 is defined as the Fourier transform of the second derivative of the extended Hamiltonian $\mathcal{H}_X = -h_X X$. Therefore, the components of the dynamical matrix are,

$$D_X^{\mu\nu}(\mathbf{q}) = -h_X \sum_{\mathbf{R}_i} \frac{\partial^2 X}{\partial u_i^\mu \partial u_0^\nu} e^{-i\mathbf{q}\cdot(\mathbf{R}_i - \mathbf{R}_0)} \tag{B.1}$$

where the lattice sum is extended over the reference set $\{\mathbf{R}_i\}$. The global non-affinity X is defined as the sum of the individual non-affine parameter χ at all the lattice sites,

$$X \equiv \sum_i^N \chi_i. \tag{B.2}$$

It is often useful to split the above sum and pull out the non-affinity at a particular lattice site 0 such that,

$$X = \chi_0 + \sum_{i, i\neq 0} \chi_i. \tag{B.3}$$

For a given coarse-graining region $\Omega(0)$, non-affinity parameter χ_0 is then given by (Eq. (2.23))

$$\chi_0 = \min_{\mathcal{D}} \sum_{j\in\Omega(0)} \sum_{\alpha=1}^{2} \left[(u_j^\alpha - u_0^\alpha) - \mathcal{D}_0^{\alpha 1}(R_j^1 - R_0^1) - \mathcal{D}_0^{\alpha 2}(\mathrm{R}_j^2 - \mathrm{R}_0^2)\right]^2. \tag{B.4}$$

Similarly for any other lattice site i,

$$\chi_i = \min_{\mathcal{D}} \sum_{j\in\Omega(i)} \sum_{\alpha=1}^{2} \left[(u_j^\alpha - u_i^\alpha) - \mathcal{D}_i^{\alpha 1}(R_j^1 - R_i^1) - \mathcal{D}_i^{\alpha 2}(\mathrm{R}_j^2 - \mathrm{R}_i^2)\right]^2, \tag{B.5}$$

where we have expressed Eq. (B.4) and (B.5) in the component form. In order to find derivatives of the each part of Eq. (B.3), one needs to express affine strain $\mathcal{D}$ in terms of the particle displacements. We show below how to obtain elements of $\mathcal{D}$ for a square lattice.

Elements of $\mathcal{D}$

The minimisation of Eq. (B.4) and (B.5) yields best fit affine strain $\mathcal{D}$ whose elements are given by Eq. (2.28),

$$\mathcal{D}_0^{\alpha\gamma} = \frac{1}{\sum_{i\in\Omega(0)}(R_i^\gamma - R_0^\gamma)^2} \sum_{i\in\Omega(0)} (u_i^\alpha - u_0^\alpha)(R_i^\gamma - R_0^\gamma) \tag{B.6}$$

and

$$\mathcal{D}_i^{\alpha\gamma} = \frac{1}{\sum_{j\in\Omega(i)}(R_j^\gamma - R_i^\gamma)^2} \sum_{j\in\Omega(i)} (u_j^\alpha - u_i^\alpha)(R_j^\gamma - R_i^\gamma) \tag{B.7}$$

For the square lattice with lattice parameter a and the coarse-graining Ω consisting nearest and next-nearest neighbours (see Fig. B.1), we find

$$\sum_{j\in\Omega(i)} (R_j^\gamma - R_i^\gamma)^2 = \sum_{i\in\Omega(0)} (R_i^\gamma - R_0^\gamma)^2 = 6a^2, \qquad \text{for all } \gamma.$$

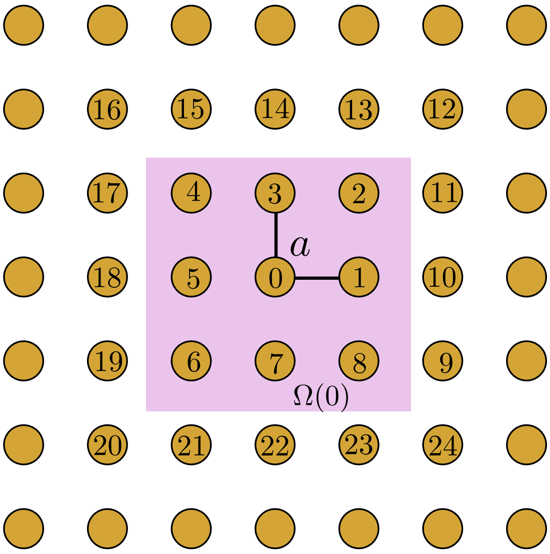

Fig. B.1. Square lattice with tagged particles used to create coarse-grained set Ω. The pink shaded region represents coarse-graining region around particle 0 with coordinates $\mathbf{R}_0 = (0, 0)$. The coarse-grained set $\Omega(0)$ consists nearest and next nearest neighbours. Similarly, coarse-graining volume for particles is also constructed (see text).

First derivative of $\mathcal{D}_0$:

Once the $\mathcal{D}_0$ is known as a function of displacements, derivatives can be evaluated easily. Therefore, with $\Omega(0) = \{1,2,3,4,5,6,7,8\}$ we get

$$\begin{aligned}\frac{\partial \mathcal{D}_0^{\alpha\gamma}}{\partial u_0^\nu} &= \frac{1}{6a^2}\frac{\partial}{\partial u_0^\nu}\left(\sum_{i\in\Omega(0)}(u_i^\alpha - u_0^\alpha)(\mathrm{R}_i^\gamma - \mathrm{R}_0^\gamma)\right)\\ &= -\delta_{\alpha\nu}\frac{1}{6a^2}\left(\sum_{i\in\Omega(0)}(\mathrm{R}_i^\gamma - \mathrm{R}_0^\gamma)\right)\end{aligned}$$

using the lattice symmetries $\left(\sum_{i\in\Omega(0)}(\mathrm{R}_i^\gamma - \mathrm{R}_0^\gamma) = 0\right)$, we finally obtain

$$\frac{\partial \mathcal{D}_0^{\alpha\gamma}}{\partial u_0^\nu} = 0 \tag{B.8}$$

First derivative of $\mathcal{D}_i$:

To evaluate the derivatives of $\mathcal{D}_i$, we note that $i \neq 0$ as required by Eq. (B.3). Further, index i is not included in the coarse-grained set $\Omega(i)$. Thus, the first derivative of $\mathcal{D}_i$ takes the following form

$$\begin{aligned}\frac{\partial \mathcal{D}_i^{\alpha\gamma}}{\partial u_0^\nu} &= \frac{1}{6a^2}\frac{\partial}{\partial u_0^\nu}\left(\sum_{j\in\Omega(i)}(u_j^\alpha - u_i^\alpha)(R_j^\gamma - R_i^\gamma)\right)\\ &= \frac{1}{6a^2}\sum_{j\in\Omega(i)}\delta_{\alpha\nu}\delta_{j0}(R_j^\gamma - R_i^\gamma)\\ &= \frac{1}{6a^2}\delta_{\alpha\nu}(R_0^\gamma - R_i^\gamma)\end{aligned} \tag{B.9}$$

Derivatives of X

first derivative of X:

We are now in a position to find derivatives of global non-affinity X. From Eq. (B.3), we have

$$\frac{\partial X}{\partial u_0^\nu} = \frac{\partial \chi_0}{\partial u_0^\nu} + \sum_{i,i\neq 0}^{N}\frac{\partial \chi_i}{\partial u_0^\nu}. \tag{B.10}$$

In the above equation, the derivatives of χ_i with respect to u_0^ν is non-zero only for i which correspond to the neighbours of 0. Therefore, the summation of i can be restricted to $i \in \Omega(0)$,

$$\frac{\partial X}{\partial u_0^\nu} = \frac{\partial \chi_0}{\partial u_0^\nu} + \sum_{i \in \Omega(0)} \frac{\partial \chi_i}{\partial u_0^\nu}. \tag{B.11}$$

With the help of Eq. (B.8) and Eq. (B.9), derivatives of χ_0 and χ_i can be obtained

$$\chi_0 = \sum_{i \in \Omega(0)} \sum_{\alpha=1}^{2} \left[(u_i^\alpha - u_0^\alpha) - \mathcal{D}_0^{\alpha 1}(R_i^1 - R_0^1) - \mathcal{D}_0^{\alpha 2}(R_i^2 - R_0^2)\right]^2$$

$$\begin{aligned}
\frac{\partial \chi_0}{\partial u_0^\nu} &= \sum_{i \in \Omega(0)} \sum_{\alpha=1}^{2} 2\delta_{\alpha\nu} \left(-1 - (R_i^1 - R_0^1)\cancel{\frac{\partial \mathcal{D}_0^{\alpha 1}}{\partial u_0^\nu}} - (R_i^2 - R_0^2)\cancel{\frac{\partial \mathcal{D}_0^{\alpha 2}}{\partial u_0^\nu}}\right) \qquad \text{(using Eq. (B.8))} \\
&\qquad \times \left[(u_i^\alpha - u_0^\alpha) - \mathcal{D}_0^{\alpha 1}(R_i^1 - R_0^1) - \mathcal{D}_0^{\alpha 2}(R_i^2 - R_0^2)\right] \\
&= -2 \sum_{i \in \Omega(0)} \left[(u_i^\nu - u_0^\nu) - \mathcal{D}_0^{\nu 1}(R_i^1 - R_0^1) - \mathcal{D}_0^{\nu 2}(R_i^2 - R_0^2)\right] \\
&= -2 \sum_{i \in \Omega(0)} (u_i^\nu - u_0^\nu) + 2\mathcal{D}_0^{\nu 1} \cancel{\sum_{i \in \Omega(0)} (R_i^1 - R_0^1)} + 2\mathcal{D}_0^{\nu 2} \cancel{\sum_{i \in \Omega(0)} (R_i^2 - R_0^2)} \\
&= -2 \sum_{i \in \Omega(0)} (u_i^\nu - u_0^\nu)
\end{aligned} \tag{B.12}$$

In the similar fashion,

$$\frac{\partial \chi_i}{\partial u_0^\nu} = -2\left[(u_i^\nu - u_0^\nu) - \mathcal{D}_i{}^{\nu 1}(R_i^1 - R_0^1) - \mathcal{D}_i{}^{\nu 2}(R_i^2 - R_0^2)\right]. \tag{B.13}$$

Upon substituting Eq. (B.12) and Eq. (B.13) in Eq. (B.11), first derivative of X is simply,

$$\frac{\partial X}{\partial u_0^\nu} = -2 \sum_{n \in \Omega(0)} \left[2\left(u_i^\nu - u_0^\nu\right) - \mathcal{D}_i^{\nu 1}\left(R_i^1 - R_0^1\right) - \mathcal{D}_i^{\nu 2}\left(R_i^2 - R_0^2\right)\right]. \tag{B.14}$$

Second derivative of X:

Calculation of the second derivative of X requires us to know elements of $\mathcal{D}_i$. Therefore, given the following sets of coarse-graining volume (see Fig. B.1)

$\Omega(0)$ = {1,2,3,4,5,6,7,8}; $\Omega(1)$ = {10,11,2,3,0,7,8,9};
$\Omega(2)$ = {11,12,13,14,3,0,1,10}; $\Omega(3)$ = {2,13,14,15,4,5,0,1};
$\Omega(4)$ = {3,14,15,16,17,18,5,0}; $\Omega(5)$ = {0,3,4,17,18,19,6,7};
$\Omega(6)$ = {7,0,5,18,19,20,21,22}; $\Omega(7)$ = {8,1,0,5,6,21,22,23};

Ω(8) = {9,10,1,0,7,22,23,24};

explicit expressions for $\mathcal{D}_i$ in terms of particle displacements is obtained by using Eq. (B.7)

$$\mathcal{D}_i^{\alpha\gamma} = \frac{1}{6a^2} \sum_{j\in\Omega(i)} (u_j^\alpha - u_i^\alpha)(R_j^\gamma - R_i^\gamma) \tag{B.15}$$

Substituting above expressions for all $\mathcal{D}_i$ in Eq. (B.14) and using the position coordinates of the lattice sites (see Fig.B.1),

$$\begin{aligned} h_X \frac{\partial X}{\partial u_0^\nu} = h_X \Bigg[& 28u_0^\nu - \frac{16}{3}\left(u_1^\nu + u_3^\nu + u_5^\nu + u_7^\nu\right) - 4\left(u_2^\nu + u_4^\nu + u_6^\nu + u_8^\nu\right) \\ & + \frac{2}{3}(u_9^\nu + u_{11}^\nu + u_{12}^\nu + u_{13}^\nu + u_{15}^\nu + u_{16}^\nu + u_{17}^\nu + u_{19}^\nu + u_{20}^\nu \\ & + u_{21}^\nu + u_{23}^\nu + u_{24}^\nu) + \frac{1}{3}\left(u_{10}^\nu + u_{14}^\nu + u_{18}^\nu + u_{22}^\nu\right) \Bigg]. \end{aligned} \tag{B.16}$$

Thus, another derivative of the above equation yields,

$$\begin{aligned} h_X \frac{\partial^2 X}{\partial u_i^\mu u_0^\nu} = h_X \Bigg[& 28\delta_{i0} - \frac{16}{3}\left(\delta_{i1} + \delta_{i3} + \delta_{i5} + \delta_{i7}\right) - 4\left(\delta_{i2} + \delta_{i4} + \delta_{i6} + \delta_{i8}\right) \\ & + \frac{2}{3}(\delta_{i9} + \delta_{i11} + \delta_{i12} + \delta_{i13} + \delta_{i15} + \delta_{i16} + \delta_{i17} + \delta_{i19} + \delta_{i20} \\ & + \delta_{i21} + \delta_{i23} + \delta_{i24}) + \frac{1}{3}\left(\delta_{i10} + \delta_{i14} + \delta_{i18} + \delta_{i22}\right) \Bigg] \delta^{\mu\nu}. \end{aligned} \tag{B.17}$$

Components of the dynamical matrix

Assuming the reference position of particle $\mathbf{R}_0 = (0, 0)$ in Fig. B.1, components of the dynamical matrix are obtained by the lattice sum,

$$\begin{aligned} D_X^{\mu\nu}(\mathbf{q}) &= -h_X \sum_{\mathbf{R}_i} \frac{\partial^2 X}{\partial u_i^\mu \partial u_0^\nu} e^{-i\mathbf{q}\cdot(\mathbf{R}_i - \mathbf{R}_0)} \\ &= -\delta^{\mu\nu} h_X \Bigg[28\delta_{i0} - \frac{16}{3}\left(\delta_{i1} + \delta_{i3} + \delta_{i5} + \delta_{i7}\right) - 4\left(\delta_{i2} + \delta_{i4} + \delta_{i6} + \delta_{i8}\right) \\ & \quad + \frac{2}{3}(\delta_{i9} + \delta_{i11} + \delta_{i12} + \delta_{i13} + \delta_{i15} + \delta_{i16} + \delta_{i17} + \delta_{i19} + \delta_{i20} \\ & \quad + \delta_{i21} + \delta_{i23} + \delta_{i24}) + \frac{1}{3}\left(\delta_{i10} + \delta_{i14} + \delta_{i18} + \delta_{i22}\right) \Bigg] e^{-i\mathbf{q}\cdot\mathbf{R_{io}}} \end{aligned} \tag{B.18}$$

$$\begin{aligned} D_X^{\nu\mu}(\mathbf{q}) \quad = \quad & -2h_X\Bigg[14 - \frac{16}{3}\left(\cos(q_x a) + \cos(q_y a)\right) - 8\left(\cos(q_x a)\cos(q_y a)\right) \\ & + \frac{4}{3}\left(\cos(2q_x a)\cos(q_y a) + \cos(q_x a)\cos(2q_y a) + \cos(2q_x a)\cos(2q_y a)\right) \\ & + \frac{1}{3}\left(\cos(2q_x a) + \cos(2q_y a)\right)\Bigg]\delta^{\mu\nu} \\ & = \; 2h_X \mathcal{A}_X \delta^{\mu\nu} \end{aligned} \tag{B.19}$$

Dynamical matrix corresponding to $\mathcal{H}_X$

$$\mathbf{D}_X(\mathbf{q}) = 2h_X \begin{pmatrix} \mathcal{A}_X & 0 \\ 0 & \mathcal{A}_X \end{pmatrix}$$

Also note that in the limit $\mathbf{q} \to 0$, the leading order of $\mathcal{A}_X \sim \mathbf{q}^4$. Explicitly,

$$\lim_{qx,qy \to 0,0} \mathcal{A}_X \sim \; -3h_X \left(\mathrm{qx}^4 + 4\mathrm{qx}^2\mathrm{qy}^2 + \mathrm{qy}^4\right) + \ldots$$

This completes the derivation of the dynamical matrix $\mathbf{D}_X(\mathbf{q})$ for the square lattice. A similar calculation can be done for other lattices as well. For all lattices such as triangular, honeycomb, and kagome we find that $\mathbf{D}_X(\mathbf{q}) \sim \mathbf{q}^4$ for small wave-numbers.

Bibliography

[1] P. M. Chaikin and T. C. Lubensky, *Principles of condensed matter physics* (Cambridge University Press, Cambridge, 1995).

[2] N. W. Ashcroft and N. D. Mermin, *Solid State Physics*, Vol. 2 (Holt, Rinehart and Winston, New York, 1976) p. 848.

[3] R. Phillips, *Crystals, Defects and Microstructures* (Cambridge University Press, 2004).

[4] J. P. Sethna, M. K. Bierbaum, K. A. Dahmen, C. P. Goodrich, J. R. Greer, L. X. Hayden, J. P. Kent-Dobias, E. D. Lee, D. B. Liarte, X. Ni, K. N. Quinn, A. Raju, D. Z. Rocklin, A. Shekhawat, and S. Zapperi, Annual Review of Materials Research **47**, 217 (2017).

[5] S. Ganguly, S. Sengupta, P. Sollich, and M. Rao, Physical Review E - Statistical, Nonlinear, and Soft Matter Physics **87**, 042801 (2013), arXiv:1212.6377 .

[6] S. Ganguly, S. Sengupta, and P. Sollich, Soft Matter **11**, 4517 (2015).

[7] A. Mitra, S. Ganguly, S. Sengupta, and P. Sollich, Journal of Statistical Mechanics: Theory and Experiment **2015**, P06025 (2015).

[8] A. K. Sood, Solid State Physics - Advances in Research and Applications **45**, 1 (1991).

[9] A. Arora and B. Tata, *Ordering and Phase Transitions in Charged Colloids* (1996) p. 361.

[10] H. Löwen, Physics Reports **237**, 249 (1994).

[11] A. Ivlev, H. Löwen, G. Morfill, and C. P. Royall (WORLD SCIENTIFIC, 2012) pp. 49–73.

[12] L. Berthier and G. Biroli, (2010), 10.1103/RevModPhys.83.587, arXiv:1011.2578 .

[13] A. Cavagna, Physics Reports **476**, 51 (2009), arXiv:0903.4264 .

[14] P. G. Wolynes and V. Lubchenko, *Structural Glasses and Supercooled Liquids: Theory, Experiment, and Applications* (John Wiley and Sons, 2012).

[15] M. D. Ediger, C. A. Angell, and S. R. Nagel, Journal of Physical Chemistry **100**, 13200 (1996), arXiv:9911023 [cond-mat] .

[16] T. Vicsek, A. Czirk, E. Ben-Jacob, I. Cohen, and O. Shochet, Physical Review Letters **75**, 1226 (1995), arXiv:0611743 [cond-mat] .

[17] A. Czirók, H. E. Stanley, and T. Vicsek, Journal of Physics A: Mathematical and General **30**, 1375 (1997), arXiv:0611741 [cond-mat] .

[18] W. F. Loomis, Methods in Cell Biology **28**, 31 (1987).

[19] A. Bricard, J. B. Caussin, N. Desreumaux, O. Dauchot, and D. Bartolo, Nature **503**, 95 (2013), arXiv:1311.2017 .

[20] J. Toner, (2018), arXiv:1812.00310 .

[21] M. Born and K. Huang, *Dynamical Theory of Crystal Lattices (Oxford Classic Texts in the Physical Sciences, 1998)* (Oxford University Press, USA, 1998) p. 432.

[22] P. C. Martin, O. Parodi, and P. S. Pershan, Physical Review A **6**, 2401 (1972).

[23] J. P. . Hirth and J. Lothe., *Theory of dislocations* (McGraw-Hill, New York, 1967).

[24] F. R. N. Nabarro and M. S. Duesbery, *Dislocations in solids*, Vol. 10 (Elsevier, Amsterdam, Amsterdam, 1996) pp. 505–594.

[25] M. L. Falk and J. Langer, Annual Review of Condensed Matter Physics **2**, 353 (2011), arXiv:1004.4684 .

[26] S. Wijtmans and M. Lisa Manning, Soft Matter **13**, 5649 (2017).

[27] A. Acharya and M. Widom, Journal of the Mechanics and Physics of Solids journal homepage **104**, 1 (2017).

[28] A. Ghosh, Z. Budrikis, V. Chikkadi, A. L. Sellerio, S. Zapperi, and P. Schall, Physical Review Letters **118**, 148001 (2017).

[29] A. Zaccone, P. Schall, and E. M. Terentjev, Physical Review B - Condensed Matter and Materials Physics **90**, 140203 (2014).

[30] S. Ganguly, P. Nath, J. Horbach, P. Sollich, S. Karmakar, and S. Sengupta, The Journal of Chemical Physics **146**, 124501 (2017).

[31] S. Ganguly and S. Sengupta, Journal of Chemical Sciences **129**, 891 (2017).

[32] S. Ganguly, P. S. Mohanty, P. Schurtenberger, S. Sengupta, and A. Yethiraj, Soft Matter **13**, 4689 (2017).

[33] S. Ganguly, D. Das, J. Horbach, P. Sollich, S. Karmakar, and S. Sengupta, Journal of Chemical Physics **149**, 184503 (2018).

[34] P. Popli, S. Kayal, P. Sollich, and S. Sengupta, Physical Review E **100**, 033002 (2019), arXiv:1907.07434 .

[35] P. Popli, S. Ganguly, and S. Sengupta, Soft Matter **14**, 104 (2017).

[36] P. Popli, P. Perlekar, and S. Sengupta, (2020), arXiv:2011.11334 .

[37] P. Nath, S. Ganguly, J. Horbach, P. Sollich, S. Karmakar, and S. Sengupta, Proceedings of the National Academy of Sciences of the United States of America **115**, E4322 (2018).

[38] D. Dube, N. Ahalawat, H. Khandelia, J. Mondal, and S. Sengupta, PLoS Computational Biology **15**, e1006665 (2019).

[39] R. Milkus and A. Zaccone, Physical Review B **93**, 094204 (2016).

[40] J. Krausser, R. Milkus, and A. Zaccone, Soft Matter **13**, 6079 (2017).

[41] M. L. Falk and J. S. Langer, Physical Review E - Statistical Physics, Plasmas, Fluids, and Related Interdisciplinary Topics **57**, 7192 (1998), arXiv:9712114 [cond-mat] .

[42] E. W. Müller and K. Bahadur, Physical Review **102**, 624 (1956).

[43] B. J. Alder and T. E. Wainwright, The Journal of Chemical Physics **31**, 459 (1959).

[44] T. C. Germann and K. Kadau, International Journal of Modern Physics C **19**, 1315 (2008).

[45] D. Myers, *Surfaces, interfaces, and colloids : principles and applications* (Wiley-VCH, 1999) p. 501.

[46] P. Pawel, Contemporary Physics **24**, 25 (1983).

[47] K. Zahn, A. Wille, G. Maret, S. Sengupta, and P. Nielaba, Physical Review Letters **90**, 155506 (2003).

[48] D. Frenkel and B. Smit, *Understanding Molecular Simulation* (Academic Press, San Diego, 2002, 2002).

[49] M. P. Allen and D. J. Tildesley, *Computer simulation of liquids* (Oxford University Press, 1987).

[50] S. Plimpton, Journal of Computational Physics **117**, 1 (1995).

[51] "LAMMPS Molecular Dynamics Simulator," .

[52] B. V. Tata, D. Boda, D. Henderson, A. Nikolov, and D. T. Wasan, Physical Review E - Statistical Physics, Plasmas, Fluids, and Related Interdisciplinary Topics **62**, 3875 (2000).

[53] N. Hoffmann, F. Ebert, C. N. Likos, H. Löwen, and G. Maret, Physical Review Letters **97** (2006), 10.1103/PhysRevLett.97.078301.

[54] P. Keim, G. Maret, U. Herz, and H. H. Von Grünberg, Physical Review Letters **92**, 215504 (2004).

[55] B. V. Tata and S. S. Jena, Solid State Communications **139**, 562 (2006).

[56] P. S. Mohanty, P. Bagheri, S. Nöjd, A. Yethiraj, and P. Schurtenberger, Physical Review X **5** (2015), 10.1103/PhysRevX.5.011030.

[57] J. Mikhael, G. Gera, T. Bohlein, and C. Bechinger, Soft Matter **7**, 1352 (2011).

[58] S. Neser, C. Bechinger, P. Leiderer, and T. Palberg, Physical Review Letters **79**, 2348 (1997).

[59] R. P. Dullens and W. K. Kegel, Physical Review Letters **92**, 195702 (2004).

[60] N. B. Simeonova, R. P. Dullens, D. G. Aarts, V. W. De Villeneuve, H. N. Lekkerkerker, and W. K. Kegel, Physical Review E - Statistical, Nonlinear, and Soft Matter Physics **73**, 041401 (2006).

[61] K. Franzrahe, P. Keim, G. Maret, P. Nielaba, and S. Sengupta, Physical Review E - Statistical, Nonlinear, and Soft Matter Physics **78**, 026106 (2008).

[62] S. Sengupta, P. Nielaba, M. Rao, and K. Binder, Physical Review E - Statistical Physics, Plasmas, Fluids, and Related Interdisciplinary Topics **61**, 1072 (2000).

[63] K. Franzrahe, P. Nielaba, and S. Sengupta, Physical Review E - Statistical, Nonlinear, and Soft Matter Physics **82**, 016112 (2010).

[64] D. Forster, *Hydrodynamic Fluctuations, Broken Symmetry, and Correlation Functions* (CRC Press, 2018) pp. 1–326.

[65] R. Bruinsma, B. I. Halperin, and A. Zippelius, Physical Review B **25**, 579 (1982).

[66] T. V. Ramakrishnan and M. Yussouff, Physical Review B **19**, 2775 (1979).

[67] T. V. Ramakrishnan, Pramana **22**, 365 (1984).

[68] C. Walz and M. Fuchs, Physical Review B - Condensed Matter and Materials Physics **81** (2010), 10.1103/PhysRevB.81.134110.

[69] J. M. Häring, C. Walz, G. Szamel, and M. Fuchs, Physical Review B - Condensed Matter and Materials Physics **92** (2015), 10.1103/PhysRevB.92.184103.

[70] C. W. Reynolds, in *Proceedings of the 14th Annual Conference on Computer Graphics and Interactive Techniques, SIGGRAPH 1987* (Association for Computing Machinery, Inc, 1987) pp. 25–34.

[71] A. Huth and C. Wissel (1990) pp. 577–595.

[72] J. L. Ericksen, Mathematics and Mechanics of Solids **13**, 199 (2008).

[73] G. I. Taylor, Proceedings of the Royal Society A: Mathematical, Physical and Engineering Sciences **145**, 362 (1934).

[74] P. Schall, D. A. Weitz, and F. Spaepen, Science **318**, 1895 (2007).

[75] H. Ahn, T. Lookman, A. Saxena, and R. Bishop, Physical Review B - Condensed Matter and Materials Physics **68**, 092101 (2003), arXiv:0207224 [cond-mat] .

[76] J. C. Maxwell, The London, Edinburgh, and Dublin Philosophical Magazine and Journal of Science **27**, 294 (1864).

[77] A. K. Geim, Science **324**, 1530 (2009).

[78] S. K. Jain, G. T. Barkema, N. Mousseau, C. M. Fang, and M. A. Van Huis, Journal of Physical Chemistry C **119**, 9646 (2015).

[79] J. G. Kirkwood, The Journal of Chemical Physics **7**, 506 (1939).

[80] A. J. Stone and D. J. Wales, Chemical Physics Letters **128**, 501 (1986).

[81] P. N. Keating, Physical Review **145**, 637 (1966).

[82] M. Mekata, Physics Today **56**, 12 (2003).

[83] T. C. Lubensky, C. L. Kane, X. Mao, A. Souslov, and K. Sun, Reports on Progress in Physics **78**, 073901 (2015).

[84] Y. Y. Kim, Y. Y. Kim, and S. Ryu, Journal of Mechanical Science and Technology **32**, 2693 (2018).

[85] L. Monette and M. P. Anderson, Modelling and Simulation in Materials Science and Engineering **2**, 53 (1994).

[86] V. Chikkadi, G. Wegdam, D. Bonn, B. Nienhuis, and P. Schall, Physical Review Letters **107**, 198303 (2011).

[87] J. D. Clayton and P. W. Chung, Journal of the Mechanics and Physics of Solids **54**, 1604 (2006).

[88] P. W. Chung, International Journal for Numerical Methods in Engineering **60**, 833 (2004).

[89] J. Lubliner, *Plasticity theory* (Dover, New York, 2008).

[90] A. Acharya, Journal of the Mechanics and Physics of Solids **49**, 761 (2001).

[91] É. Brillaux and F. Turci, Soft Matter **15**, 4371 (2019).

[92] J. Zylberg, E. Lerner, Y. Bar-Sinai, E. Bouchbinder, and J. S. Langer, Proceedings of the National Academy of Sciences of the United States of America **114**, 7289 (2017).

[93] A. J. Hurd, N. A. Clark, R. C. Mockler, and W. J. O'Sullivan, Physical Review A **26**, 2869 (1982).

[94] Z. Cheng, J. Zhu, W. B. Russel, and P. M. Chaikin, Physical Review Letters **85**, 1460 (2000).

[95] M. Bowick and P. Chaikin, Nature Materials **15**, 1151 (2016).

[96] W. T. M. Irvine, A. D. Hollingsworth, D. G. Grier, and P. M. Chaikin, Proceedings of the National Academy of Sciences **110**, 15544 (2013).

[97] A. Van Blaaderen, Nature **439**, 545 (2006).

[98] A. P. Hynninen, J. H. Thijssen, E. C. Vermolen, M. Dijkstra, and A. Van Blaaderen, Nature Materials **6**, 202 (2007).

[99] A. D. Law, D. M. A. Buzza, and T. S. Horozov, Physical Review Letters **106**, 128302 (2011).

[100] S. C. Glotzer and M. J. Solomon, Nature Materials **6**, 557 (2007).

[101] J. Russo, P. Tartaglia, and F. Sciortino, Soft Matter **6**, 4229 (2010).

[102] P. Pieranski, Physical Review Letters **45**, 569 (1980).

[103] D. Ershov, J. Sprakel, J. Appel, M. A. Stuart, and J. Van Der Gucht, Proceedings of the National Academy of Sciences of the United States of America **110**, 9220 (2013).

[104] A. Van Blaaderen, R. Ruel, and P. Wiltzius, Nature **385**, 321 (1997).

[105] A. Chowdhury, B. J. Ackerson, and N. A. Clark, Physical Review Letters **55**, 833 (1985).

[106] J. Bewerunge, A. Sengupta, R. F. Capellmann, F. Platten, S. Sengupta, and S. U. Egelhaaf, Journal of Chemical Physics **145**, 044905 (2016), arXiv:1607.02288 .

[107] E. Frey, D. R. Nelson, and L. Radzihovsky, Physical Review Letters **83**, 2977 (1999).

[108] Y. Peng, F. Wang, Z. Wang, A. M. Alsayed, Z. Zhang, A. G. Yodh, and Y. Han, Nature Materials **14**, 101 (2015).

[109] G. C. Spalding, J. Courtial, R. Di Leonardo, and D. L. Andrews, *Structured Light and its Applications* (Elsevier Inc., 2008) pp. 139–168.

[110] X. Mao, A. Souslov, C. I. Mendoza, and T. C. Lubensky, Nature Communications **6**, 5968 (2015), arXiv:1407.1946 .

[111] F. H. Stillinger, The Journal of Chemical Physics **65**, 3968 (1976).

[112] F. H. Stillinger and T. A. Weber, The Journal of Chemical Physics **74**, 4015 (1981).

[113] S. Prestipino, F. Saija, and P. V. Giaquinta, Physical Review Letters **106**, 235701 (2011), arXiv:1107.0828 .

[114] M. Zu, J. Liu, H. Tong, and N. Xu, Physical Review Letters **117**, 085702 (2016), arXiv:1605.00747 .

[115] K. Bhattacharya, S. Conti, G. Zanzotto, and J. Zimmer, Nature **428**, 55 (2004).

[116] H. Shiba, Y. Yamada, T. Kawasaki, and K. Kim, Physical Review Letters **117**, 245701 (2016), arXiv:1510.02546 .

[117] B. Illing, S. Fritschi, H. Kaiser, C. L. Klix, G. Maret, and P. Keim, Proceedings of the National Academy of Sciences of the United States of America **114**, 1856 (2017), arXiv:1510.05804 .

[118] S. Vivek, C. P. Kelleher, P. M. Chaikin, and E. R. Weeks, Proceedings of the National Academy of Sciences of the United States of America **114**, 1850 (2017).

[119] O. Otto, F. Czerwinski, J. L. Gornall, G. Stober, L. B. Oddershede, R. Seidel, and U. F. Keyser, Optics Express **18**, 22722 (2010).

[120] Y. Tanaka and S.-i. Wakida, Biomedical Optics Express **6**, 3670 (2015).

[121] J. J. Juárez and M. A. Bevan, Advanced Functional Materials **22**, 3833 (2012).

[122] B. L. Partridge, Scientific American **246**, 114 (1982).

[123] W. J. Rappel, A. Nicol, A. Sarkissian, H. Levine, and W. F. Loomis, Physical Review Letters **83**, 1247 (1999), arXiv:9811001 [patt-sol] .

[124] K. B. Raper and J. T. Bonner, Mycologia **60**, 211 (1968).

[125] D. Geyer, A. Morin, and D. Bartolo, Nature Materials **17**, 789 (2018).

[126] H. Levine, W. J. Rappel, and I. Cohen, Physical Review E - Statistical, Nonlinear, and Soft Matter Physics **63**, 1 (2001), arXiv:0006477 [cond-mat] .

[127] J. Toner, Physical Review Letters **108** (2012), 10.1103/PhysRevLett.108.088102, arXiv:1108.4392 .

[128] Y. Hatwalne, S. Ramaswamy, M. Rao, and R. A. Simha, Physical Review Letters **92** (2004), 10.1103/PhysRevLett.92.118101, arXiv:0308529 [cond-mat] .

[129] R. A. Simha and S. Ramaswamy, in *Physica A: Statistical Mechanics and its Applications*, Vol. 306 (2002) pp. 262–269.

[130] R. Aditi Simha and S. Ramaswamy, Physical review letters **89**, 058101 (2002), arXiv:0108301 [cond-mat] .

[131] N. Khurana and N. T. Ouellette, New Journal of Physics **15**, 095015 (2013).

[132] A. Choudhary, D. Venkataraman, and S. Sankar Ray, EPL **112** (2015), 10.1209/0295-5075/112/24005.

[133] D. Floreano and R. J. Wood, "Science, technology and the future of small autonomous drones," (2015).

[134] Intel, "Drone Light Shows Powered by Intel," (2016).

[135] M. E. Rosti, A. A. Banaei, L. Brandt, and A. Mazzino, Physical Review Letters **121** (2018), 10.1103/PhysRevLett.121.044501, arXiv:1801.10194 .

[136] J. C. Fung and J. C. Vassilicos, Physical Review E - Statistical Physics, Plasmas, Fluids, and Related Interdisciplinary Topics **57**, 1677 (1998).

[137] J. C. Fung, J. C. Hunt, N. A. Malik, and R. J. Perkins, Journal of Fluid Mechanics **236**, 281 (1992).

[138] F. Nicolleau and G. Yu, Physics of Fluids **16**, 2309 (2004).

[139] C. Brouzet, G. Verhille, and P. Le Gal, Physical Review Letters **112** (2014), 10.1103/PhysRevLett.112.074501.

[140] G. Verhille and A. Bartoli, Experiments in Fluids **57** (2016), 10.1007/s00348-016-2201-1.

[141] A. Gay, B. Favier, and G. Verhille, EPL **123** (2018), 10.1209/0295-5075/123/24001.

[142] D. Dotto and C. Marchioli, Acta Mechanica **230**, 597 (2019).

[143] S. Allende, C. Henry, and J. Bec, Physical Review Letters **121** (2018), 10.1103/PhysRevLett.121.154501.

[144] J. Bec, Physics of Fluids **15** (2003), 10.1063/1.1612500, arXiv:0306049 [nlin] .

[145] K. Gustavsson and B. Mehlig, Advances in Physics **65**, 1 (2016), arXiv:1412.4374 .

[146] R. Singh, M. Gupta, J. R. Picardo, D. Vincenzi, and S. S. Ray, (2019), arXiv:1908.08776 .

[147] H. Kedia, D. Pan, J.-J. Slotine, and J. L. England, (2019), arXiv:1908.09332 .

[148] N. Grønbech-Jensen and O. Farago, Molecular Physics **111**, 983 (2013), arXiv:1212.1244 .

[149] L. Ducasse and A. Pumir, Physical Review E - Statistical, Nonlinear, and Soft Matter Physics **77** (2008), 10.1103/PhysRevE.77.066304.

[150] M. M. Bandi, J. R. Cressman, and W. I. Goldburg, Journal of Statistical Physics **130**, 27 (2008).

[151] U. Frisch, *Turbulence* (Cambridge University Press, 1995).

[152] "Starlink," ().

[153] "SpaceX Starlink - Wikipedia," ().

[154] "Loon LLC - Wikipedia," ().

[155] "Loon," ().

[156] "US9853715B2 - Broadband access system via drone/UAV platforms - Google Patents," .

[157] N. S. Gillis, N. R. Werthamer, and T. R. Koehler, Physical Review **165**, 951 (1968).

[158] L. K. Moleko, B. Joos, T. M. Hakim, H. R. Glyde, and S. T. Chui, Physical Review B **34**, 2815 (1986).

[159] R. Ahluwalia, T. Lookman, A. Saxena, and S. R. Shenoy, Phase Transitions **77**, 457 (2004).

[160] S. R. Shenoy, T. Lookman, A. Saxena, and A. R. Bishop, Physical Review B - Condensed Matter and Materials Physics **60**, R12537 (1999).

[161] K. Rasmussen, T. Lookman, A. Saxena, A. R. Bishop, R. C. Albers, and S. R. Shenoy, Physical Review Letters **87**, 55704 (2001).

[162] A. R. Bishop, T. Lookman, A. Saxena, K. Rasmussen, and S. R. Shenoy, Physical Review B - Condensed Matter and Materials Physics **67**, 024114 (2003), arXiv:0211425 [cond-mat] .

[163] M. Rao and S. Sengupta, Journal of Physics Condensed Matter **16**, 7733 (2004).

[164] A. Paul, J. Bhattacharya, S. Sengupta, and M. Rao, Journal of Physics Condensed Matter **20** (2008), 10.1088/0953-8984/20/36/365211.

[165] J. Bhattacharya, A. Paul, S. Sengupta, and M. Rao, Journal of Physics Condensed Matter **20** (2008), 10.1088/0953-8984/20/36/365210.

[166] S. Sengupta, M. Rao, and J. Bhattacharya, Journal of Physics Condensed Matter **23** (2011), 10.1088/0953-8984/23/29/295402.

[167] J. Russo, F. Romano, and H. Tanaka, Physical Review X **8** (2018), 10.1103/PhysRevX.8.021040.

[168] A. Banerjee, S. Sengupta, S. Sastry, and S. M. Bhattacharyya, Physical Review Letters **113**, 225701 (2014), arXiv:1404.0815 .

[169] V. Molinero, S. Sastry, and C. A. Angell, Physical Review Letters **97**, 075701 (2006).

[170] B. C. Kuo and M. F. Golnaraghi, *Automatic control systems* (John Wiley & Sons, 2003) p. 609.

Atomic fuctuations are generally represented in terms of long and short wavelength phonon modes. This representation has led to a deeper understanding of many observed properties of crystalline solids. However, constructing a precise precise set of phonons which tantamount to the dominant lattice defect is often a non trivial task. As shown recently, any set of displacement of particles away from some specified reference configuration can be projected onto two mutually orthogonal space viz. affine and non-affine. In this new way of classifying fluctuations, the affine modes involves smoothly varying, elastic displacements and can be written as a linear transformation of this reference configuration. Whereas the latter, consists of discontinuous displacements and has been proved to be related to defects in certain two dimensional crystalline solids. Proceeding along similar lines, we generalise the projection formalism to investigate statistics of non-affine fluctuations in several two and three dimensional crystals. In each case we show that the non-affine modes are indeed associated with the commonly observed lattice defects. Furthermore, the susceptibility of a crystalline solid to any particular defect can also be estimated from the excitation spectra of non-affine modes. Using this knowledge we devise an experimental protocol to (a) stabilise any lattice of colloidal particles. (b) stabilising the patterns of active swarms of drones. This is accomplished in an energy efficient way by imposing “non-affine forces”. These forces alters the particle’s arrangement in order to minimise non-affine fluctuations and allows only affine transformations such as translation and rotation. In the former case, the colloidal lattice thus produced is translationally invariant and retains all the low energy modes. The patterned swarm of the drones is free to move in space and can be used for surveying territories and do scientific measurements. As a novel outcome of our study the statistics of the underlying source of fluctuation can be obtained solely from that of the applied non-affine forces.